# Magnetic, structural, and electronic properties of $NiFe_2O_4$ ultrathin films

Michael Hoppe

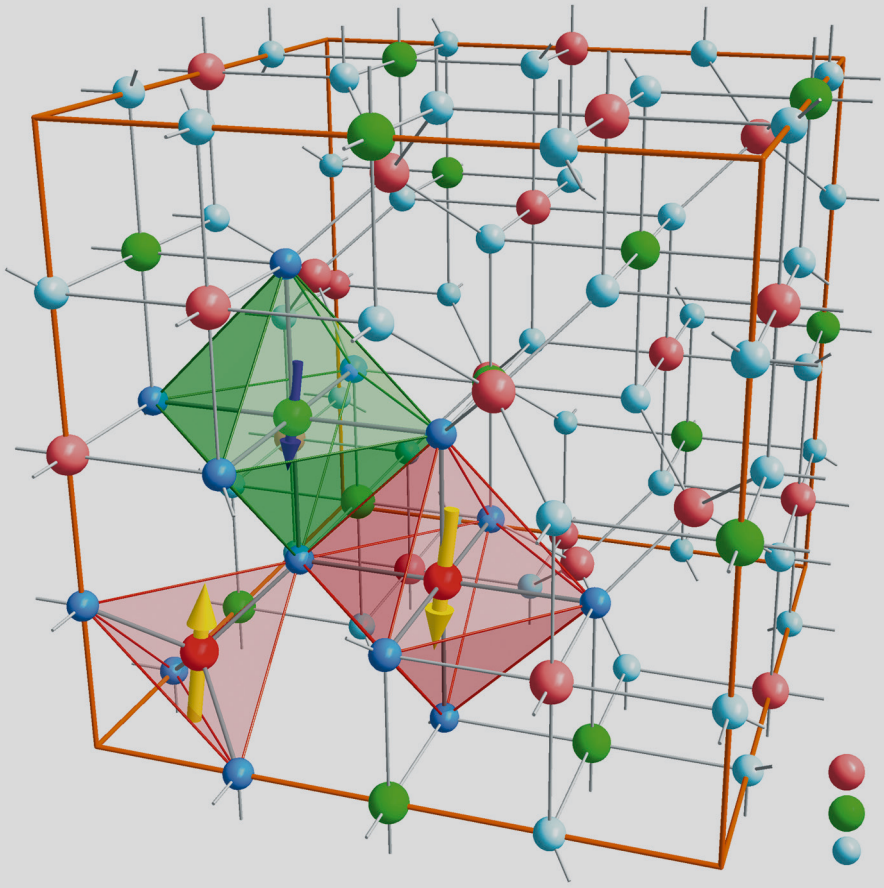

Schlüsseltechnologien / Key Technologies
Band / Volume 118
ISBN 978-3-95806-122-4

JÜLICH FORSCHUNGSZENTRUM

Schriften des Forschungszentrums Jülich
Reihe Schlüsseltechnologien / Key Technologies Band / Volume 118

Forschungszentrum Jülich GmbH
Peter Grünberg Institute (PGI)
Electronic Properties (PGI-6)

# Magnetic, structural, and electronic properties of $NiFe_2O_4$ ultrathin films

Michael Hoppe

Schriften des Forschungszentrums Jülich
Reihe Schlüsseltechnologien / Key Technologies Band / Volume 118

ISSN 1866-1807 ISBN 978-3-95806-122-4

Bibliographic information published by the Deutsche Nationalbibliothek.
The Deutsche Nationalbibliothek lists this publication in the Deutsche Nationalbibliografie; detailed bibliographic data are available in the Internet at http://dnb.d-nb.de.

Publisher and Distributor: Forschungszentrum Jülich GmbH
Zentralbibliothek
52425 Jülich
Tel: +49 2461 61-5368
Fax: +49 2461 61-6103
Email: zb-publikation@fz-juelich.de
www.fz-juelich.de/zb

Cover Design: Grafische Medien, Forschungszentrum Jülich GmbH

Printer: Grafische Medien, Forschungszentrum Jülich GmbH



Schriften des Forschungszentrums Jülich
Reihe Schlüsseltechnologien / Key Technologies, Band / Volume 118

D 464 (Diss., Duisburg, Univ., 2015)

ISSN 1866-1807
ISBN 978-3-95806-122-4

The complete volume is freely available on the Internet on the Jülicher Open Access Server (JuSER) at www.fz-juelich.de/zb/openaccess.

# Abstract

The physical properties of transition-metal oxides are strongly determined by the competition of charge, spin, and orbital degrees of freedom. Continuing progress in the deposition techniques of oxides nowadays allows to grow thin film heterostructures with atomically sharp interfaces. Tailoring the interface between oxides opens up the possibility to explore novel nanoelectronic functionalities and even to discover new phenomena only existing at the interface.

In this framework, oxides featuring simultaneously magnetic and insulating properties offer a promising approach for the optimized performance of spintronic devices. They can realize a highly effective spin-filter effect, where spin-polarized electron currents are generated by a spin-dependent tunneling process. For this purpose, the spinel ferrite $NiFe_2O_4$ is a very auspicious material since it possesses both features even at room temperature.

In this thesis, the sensitive interplay between magnetic, electronic and structural properties in the ferrimagnetic oxide $NiFe_2O_4$ is investigated in detail. Therefore, $NiFe_2O_4$ thin films are deposited on Nb-doped $SrTiO_3$ (001) substrates via pulsed laser deposition (PLD) and the growth conditions of the deposition process are carefully evaluated. Based upon this, a procedure is deduced, that allows the reproducible growth of high-quality, epitaxial, and single-crystalline $NiFe_2O_4$ thin films.

With the aim towards fabricating tunnel barriers, special emphasis is placed on the impact of reduced dimensionality in the crossover from bulk-like to ultrathin $NiFe_2O_4$ films. Here, an enhanced saturation magnetization $M_S$ for ultrathin $NiFe_2O_4$ films ($d < 4$ nm) that coincides with a reduced out-of-plane lattice constant under compressive in-plane epitaxial strain is observed. The films are investigated by complementing bulk- and surface-sensitive analyses using HAXPES, XANES and XMCD spectroscopy techniques. Hereby, a bulk-like cationic coordination of the inverse spinel lattice independent of the $NiFe_2O_4$ film thickness is found – thus ruling out a cationic inversion that nominally could account for an enhanced $M_S$.

The spin and orbital contribution to the net magnetization are investigated element-specific by recording high-quality low noise XMCD spectra and evaluating them using the sum rules. The resulting moments agree with the magnetic structure of an inverse spinel. However, they give no explanation for the observed enhanced $M_S$. Instead, a novel magnetism at the interface between the $NiFe_2O_4$ films and $SrTiO_3$ substrates is discovered, which originates from a ferromagnetic ordering of the Ti electrons. The underlying mechanism is explained by superexchange interaction across the interface which imposes the ferromagnetic order of the electron in $NiFe_2O_4$ onto the Ti electrons.

The given results open the path for a future integration of $NiFe_2O_4$ into spin filter tunnel junctions. Additionally, the observed interfacial Ti ferromagnetism renders $NiFe_2O_4/SrTiO_3$ heterostructures as a intriguing system for exploring the interplay between the various degrees of freedom in transition metal oxides.

## Kurzzusammenfassung

Die physikalischen Eigenschaften von Übergangs-Metalloxiden hängen in starken Maße von dem Wechselspiel der Ladungs-, Spin- und orbitalen Freiheitsgrade ab. Die Fortschritte in der Entwicklung von Dünnfilmabscheidungs-Technologien für Oxide erlauben heutzutage die Herstellung von oxidischen Heterostrukturen mit atomar definierten Grenzflächen. Durch die Optimierung der Grenzflächen können neue nano-elektronische Bauteile entwickelt werden oder physikalische Effekte untersucht werden, welche ihren Ursprung ausschließlich an der Grenzfläche haben.

In diesem Kontext bieten Oxide, welche gleichzeitig magnetisch und isolierend sind, einen vielversprechenden Ansatz für die Optimierung von spin-elektronischen Schalkreisen. Mit diesen kann eine hocheffiziente Injektion von spin-polarisierten Elektronenströmen realisiert werden, da ein Tunnelstrom durch diese Materialien hochgradig spin-abhängig ist. Hierfür ist $NiFe_2O_4$ ein aussichtsreicher Kandidat, da er beide Eigenschaften schon bei Raumtemperatur aufweist.

In dieser Arbeit wird das Zusammenspiel zwischen den magnetischen, elektronischen und strukturellen Eigenschaften des ferromagnetischen Oxids $NiFe_2O_4$ eingehend untersucht. Dafür werden dünne $NiFe_2O_4$ Schichten auf Nb-dotierten $SrTiO_3$ Substraten mit Hilfe von gepulster Laser-Ablation (PLD) abgeschieden, wobei der Einfluss der Wachstumsbedingungen detailliert analysiert wird. Darauf aufbauend wird ein Wachstumsprozess definiert, welcher die reproduzierbare Herstellung von hochqualitativen, epitaktischen und einkristallinen $NiFe_2O_4$ Filmen erlaubt.

Für das Ziel der Herstellung von magnetischen Tunnelbarrieren, wird der Übergang von bulkartigen zu ultradünnen $NiFe_2O_4$ Schichten untersucht und dabei wird insbesondere auf den Einfluss durch die reduzierte Dimensionalität geachtet. Hierbei wird eine erhöhte Magnetisierung $M_S$ im Grenzfall ultradünner Filme ($d < 4$ nm) beobachtet. Diese geht einher mit einer reduzierten out-of-plane Gitterkonstante, welche trotz der biaxial komprimierenden in-plane Verzerrung der Filme durch das Substrat auftritt. Die Schichten werden mit den sich ergänzenden Techniken HAXPES, XANES und XMCD untersucht, welche bulk- oder oberflächenempfindlich sind. Dabei zeigen alle Filme eine bulk-artige Kationenverteilung, wie sie in der inversen Spinel-Struktur erwartet wird. Dadurch kann der bisherige Erklärungsansatz für das erhöhte $M_S$, nämlich eine kationische Inversion der Spinel-Struktur, ausgeschlossen werden.

Die spin- und orbitalen Beiträge zum magnetischen Gesamtmoment der Filme werden durch die Aufnahme hochqualitativer XMCD Spektren element-spezifisch untersucht, welche mit Hilfe der Summenregeln ausgewertet werden. Die sich ergebenden Spin- und Orbitalmomente stimmen dabei mit der erwarteten magnetischen Struktur in einem inversem Spinel überein. Sie erklären jedoch nicht die beobachte erhöhte $M_S$. Stattdessen zeigt sich ein neuartiger Ferromagnetismus an der Grenzfläche zwischen den $NiFe_2O_4$ Filmen und den $SrTiO_3$ Substraten, welcher auf einer ferromagnetischen Ordnung der Ti Elektronen basiert. Der Ursprung dieser Ordnung wird durch eine Superaustausch-Wechselwirkung über die Grenzfläche hinweg erklärt, welche den Ti Elektron die ferromagnetische Ordnung der angrenzenden $NiFe_2O_4$ Schicht aufzwingt.

Aufbauend auf den präsentierten Ergebnissen kann im nächsten Schritt $NiFe_2O_4$ in eine Spin-Filter-Tunnelbarriere integriert werden. Außerdem, zeigt sich durch den beobachteten Ti Ferromagnetismus, dass $NiFe_2O_4/SrTiO_3$ Heterostrukturen ein vielversprechenden Modellsystem sein können, um das Zusammenspiel der Ladungs-, Spin- und orbitalen Freiheitsgrade in Übergangs-Metalloxiden zu untersuchen.

# Contents

# CHAPTER 1

# Introduction

The global demand for computing power has increased continuously throughout the last decades and is expected to increase further. Nowadays, logic operations are still primarily performed by semiconductors which are based on the manipulation of electron charge currents. Large efforts have been undertaken to improve the efficiency of nanoelectronics. However, the advancements hardly keep pace with the rising power consumption due the increased variety of electronic devices. The energy demand arising from information technology in Germany is expected to rise from 55.4 TWh to 66.7 TWh between 2007 and 2020 [1].

One possibility to address this challenge is the employment of spintronics. In contrast to conventional electronics, where only the charge of the electrons is manipulated, spintronics governs all concepts which involve the manipulation of the electrons intrinsic magnetic moment, which is known as its spin. The initial breakthrough of spintronics can be traced back to the discovery of the interlayer exchange coupling between ultrathin ferromagnetic films by P. Grünberg [2] and the giant magnetoresistance (GMR) effect by P. Grünberg and A. Fert [3, 4] in the late 1980s. The latter allows to detect very small magnetic fields, an effect that is employed since 1997 in the readout heads of computer hard-disks.

While the GMR effect gave a significant improvement to the performance of non-volatile memory, the next important step is the realization of spin-based logic circuits. In this regard, the spin-field effect transistor has been proposed, which relies on three subsequent steps [5]: First, a spin-polarized current is injected into a semiconductor. Afterwards, the spin state of the current is manipulated and finally analysed. An additional advantage is that switching the spin state is less energy consuming than the manipulation of a charge current in a classical field effect transistor.

Functional oxides moved into the focus of current spintronics research, since they

offer a broad variety of magnetic and electronic properties that may be incorporated and utilized in novel types of applications. Still, one major challenge for the optimized performance of spintronic devices is the creation of highly spin-polarized electron currents. One intuitive approach is the use of half-metals, e.g. $Fe_3O_4$, for which only one spin character is present at the Fermi level, which could naturally lead to a 100 % spin polarization. Their integration into functional spintronics devices, however, has turned out to be challenging. Another promising path is the usage of magnetic insulator tunnel barriers. Due to their spin-split conduction bands, magnetic insulators offer spin-dependent tunneling barrier heights with highly spin-dependent transition probabilities. Successful spin filtering has been demonstrated e.g. in EuS [6, 7], and EuO has been recently integrated into single-crystalline model systems [8, 9]. While the Eu compounds are limited to low Curie temperatures $T_C$, magnetic oxides from the family of the spinel ferrites with sizeable magnetic properties at and above room temperature give perspective for application. One representative of such high-$T_C$ magnetic oxides is the spinel $NiFe_2O_4$, which has a large bandgap of 1.65 eV [10] and a high Curie temperature of $T_C$ = 865 K [11]. Due to the complex crystalline structure of the spinel lattice, the growth of epitaxial and well-ordered $NiFe_2O_4$ thin films is a challenging task [12–14]. The various degrees of freedom in complex oxides, however, allow one to tailor their thin film properties by choosing appropriate growth conditions.

Furthermore, the controlled synthesis of high-quality oxide-oxide heterostructures has opened up the opportunity to study emerging physical phenomena, which are only existent at the interface of oxides itself. Designing electronic properties in ultrathin oxide films and interfaces thereby opens up routes to explore novel nanoelectronic functionalities for applications. In this pursuit, the interface between $SrTiO_3$ and $LaAlO_3$ has attracted a lot of interest in the last decade, due to the formation of a conductive two-dimensional electron gas. While, the two oxides themselves are insulating and non-magnetic, the interface between them shows properties like electrical conductivity [15], superconductivity [16], and ferromagnetism [17, 18]. Ongoing on these findings, the underlying 2D electron gas has also been identified in a broad variety of oxide interfaces between perovskite bilayers [19], which are however exclusively isostructural. Yet, recently also the complex oxide spinel/perovskite interface between $\gamma$-$Al_2O_3$ and $SrTiO_3$ revealed the formation of a 2D electron gas, with more than one order of magnitude higher electron mobilities [20]. In this pursuit, the heterointerface between $NiFe_2O_4$ and $SrTiO_3$ is becoming worthwhile for further investigations, since it allows to study the interplay at an oxide-oxide interface between two insulators with the magnetic ordering of $NiFe_2O_4$.

In this thesis, the fundamental properties of $NiFe_2O_4$ in the ultrathin film limit will be investigated in detail. The long-term goal is to integrate $NiFe_2O_4$ as magnetic tunnel barriers to evaluate its suitability as a magnetic insulating spin filters. Moreover, the controlled growth of ultrathin films with atomic sharp interfaces allows to study the interface between $NiFe_2O_4$ and the underlying substrate. First, the physical properties of $NiFe_2O_4$ in a bulk-like state are elucidated in **chapter 2**. Special attention is paid to the underlying mechanisms which are responsible for the coexistent insulating and

ferrimagnetic properties of $NiFe_2O_4$.

Next, the experimental methods which are employed during this work will be discussed in **chapter 3**. Since $NiFe_2O_4$ consists of three atomic species, we have chosen pulsed laser deposition (PLD) as a method for the growth of $NiFe_2O_4$ thin films, because it allows to transfer the stoichiometry of the compound as a thin film. After growth, every film needs to be characterized carefully for its structural and magnetic properties. Therefore, atomic force microscopy (AFM), X-ray diffraction (XRD), and SQUID experiments are used, which will be briefly introduced. Finally, the main work during this theses was performed using a variety of photon based X-ray core level spectroscopy techniques. All of them allow to probe the samples element-specifically, which is a major advantage for the investigation of a ternary compound. In particular, we have utilized hard X-ray photoemission spectroscopy (HAXPES), X-ray absorption near edge spectroscopy (XANES) and X-ray magnetic circular dichroism (XMCD). The advantages and caveats of these techniques are discussed in the last part of the chapter.

For the integration of thin films into tunnel junctions or heterostructures, one needs to gain precise control over the growth of the functional layer. Therefore, in **chapter 4**, we investigate the influence of the various growth parameters of the PLD process onto the properties of the grown film. Hereby, the energy of the laser pulses, the background pressure during deposition, and the substrate temperature are varied. Afterwards, the quality of the resulting films is evaluated by probing their structural and magnetic properties, as well as their surface roughness. In the end, we investigated the influence of the oxygen partial pressure in the background gas during deposition onto the film quality. From these studies, we find a set of growth parameters yielding in a reproducible high quality growth of $NiFe_2O_4$ thin films.

In a next step, the film thickness of the $NiFe_2O_4$ films is scaled down to a dimension of 1 – 3 nm, which is for instance necessary for future application in a tunnel barrier. However, magnetic spinels reveal an unexpected behaviour in the ultrathin film – i.e. an enhanced saturation magnetization as compared to the bulk [13, 21] – a feature we also observe in our samples. Still, an explanation for the origin of this fundamental phenomenon is lacking. Thus, the sensitive interplay between magnetic, electronic and structural properties in $NiFe_2O_4$ is investigated in **chapter 5**. Hereby, special attention is paid to the dependence of the film properties on their thickness. We use HAXPES – the high energy counterpart of soft X-ray photoemission spectroscopy – to analyse the electronic structure and the valency of the cation with bulk sensitivity. Additionally, XANES is employed to probe the valency, but also the coordination of oxygen anions around the cations. Finally, XMCD spectra of the samples are recorded and compared to model spectra from ligand field multiplet calculation. Based upon this, the cationic distribution in the films can be clearly identified and an earlier proposed cationic inversion of the spinel structure can be ruled out unambiguously.

Still, the origin of the enhanced magnetic moment is not determined. In order to element-selectively probe the magnetic properties of $NiFe_2O_4$ ultrathin films, we recorded high quality XMCD spectra over a wide energy range, which will be presented in **chapter**

**6**. The rigorous treatment of the data allows to apply the MCD sum rules [22, 23], which in turn enable us to determine the spin- and orbital magnetic moments for both cation species in $NiFe_2O_4$ individually. From these, no increase of the net magnetization of the films with decreasing thickness can be resolved. Instead, we found a novel ferromagnetic behaviour of the Ti cations at the interface to the underlying $SrTiO_3$ substrate. The possible origin for this surprising phenomenon will be discussed in detail and opens up a new playground for studying the sensitive interplay between the lattice, spin- and orbital degrees of freedom in transition metal oxides.

Finally, a conclusion of the presented results is given in **chapter 7**.

CHAPTER 2

# Theoretical background

This chapter introduces the fundamental aspects that are relevant for describing the physical properties of the magnetic insulator $NiFe_2O_4$. The spinel $NiFe_2O_4$ is a material, which consists of oxygen ions and 3*d* transition metal cations. Hereby, the 3*d* bands are only partly filled, but still $NiFe_2O_4$ shows insulating behaviour. This can be explained by a localization of the 3*d* electrons, which is described by the Mott-Hubbard model in the following. Subsequently, the exchange interaction which give rise to the ferrimagnetic ordering in $NiFe_2O_4$ are discussed.

## 2.1. Mott-Hubbard model

We start from the tight-binding model, in which the atoms in a lattice are treated in a single atom picture and the overlap of the electronic wave functions between adjacent atoms is handled as a perturbation to this. Due to this overlap, the electrons can hop from one lattice site to another. The probability of such a hopping process is given by the hopping matrix element $t$, and can be described by the following Hamiltonian:

$$\hat{H} = -t \sum_{\langle i,j\rangle,\sigma} \left( c^{\dagger}_{i,\sigma} c_{j,\sigma} + c^{\dagger}_{j,\sigma} c_{i,\sigma} \right) \tag{2.1}$$

Hereby, the sum runs over all adjacent lattice sites $\langle i, j\rangle$ and spins $\sigma$, while $c^{\dagger}_{i,\sigma}$ and $c_{i,\sigma}$ are the creation and annihilation operator for electron with spin $\sigma$ on site $i$. For simplicity, $\hat{H}$ is only written for the case of one orbital per lattice site. The hopping matrix element $t$ lowers the kinetic energy of the electrons, which are thus no more localized. This results in the formation of bands, with a width $W$ that is proportional to the matrix element ($W \sim t$). If these bands are only partly occupied, like the Ni or Fe 3*d* band, the band

model predicts metallic conducting behaviour of the material. So far, the tight-binding model completely neglected the electron-electron interactions, which are included in the Mott-Hubbard model. Hereby, the term $U$ is introduced, which describes the Coulomb repulsion of two electrons sitting on the same lattice site [24, 25]. The Hamiltonian can now be written as

$$\hat{H} = -t \sum_{\langle i,j\rangle,\sigma} (c^{\dagger}_{i,\sigma} c_{j,\sigma} + c^{\dagger}_{j,\sigma} c_{i,\sigma}) + U \sum_{i=1}^{N} n_{i\uparrow} n_{i\downarrow} \ , \tag{2.2}$$

where $n_{i\sigma} = c^{\dagger}_{i,\sigma} c_{i,\sigma}$ is the counting operator, that becomes one if an electron with spin $\sigma$ sits on site $i$, and zero else wise. Thus, the second term contributes $U$ if two electron in the band are staying on the same lattice site. Consequently, the electrons have a reduced mobility and become more localized. If the on-site repulsion $U$ becomes larger than the width $W$ of the band, it splits into an energetically lower lying filled band and a higher lying empty one. If the two bands are still overlapping or are completely split depends on the ratio $U/W$. Thus, with increasing $U/W$ the band structure migrates from a metallic to an insulating one, what is called the Mott-Hubbard (metal-insulator) transition. For these reasons, also partly occupied orbitals like the $3d$ orbitals in $NiFe_2O_4$ can result in an insulating behaviour.

In transition metal oxides also the $2p$-bands of oxygen are lying closely below the Fermi energy. If the repulsion $U$ is large, it is possible, that the lower Hubbard band is pushed below the O $2p$ levels, and thus the latter one become the highest occupied state. In this case, the band gap is given by the distance between the O $2p$ levels and the unoccupied upper Hubbard band and the system is called a charge-transfer (CT) insulator. The spinel $NiFe_2O_4$ is such an CT insulator, as will be discussed in section 2.8.

## 2.2. Heisenberg model

The last section described the insulating character of $NiFe_2O_4$ due to a splitting of the partly filled band $3d$ band into an empty and a filled band. In a band insulator the highest occupied band would be completely filled, i.e. the electronic states for all possible spin and orbital quantum numbers in the band are occupied. Thus, the spin and orbital degrees of freedom of all electrons in the insulator are completely quenched, which is why no ordering of these degrees is possible any more. In contrast, in the Mott-Hubbard insulator, the electrons are localized but still have open degrees of freedom. These can now couple to other lattice sites via exchange interactions, which in turn can result in an ordering of them. In case of the spin-spin interactions in localized electron systems, the ordering can be approximated by the Heisenberg model, which only considers the exchange interaction between adjacent lattice sites.

$$\hat{H} = -J \sum_{\langle i,j\rangle} \hat{\mathbf{S}}_i \cdot \hat{\mathbf{S}}_j \tag{2.3}$$

Hereby, $\hat{\mathbf{S}}_i$ is the operator describing the spin state of the electron on site $i$ and $J$ the coupling constant describing the exchange interactions. If $J$ is positive a parallel alignment of the spin in energetically favourable, resulting in a ferromagnetic ordering pattern. On the contrary, $J < 0$ causes an antiferromagnetic ordering.

## 2.3. Exchange interaction in a 1D-chain

To describe the exchange interaction in localized electron systems, we start with a simplified description, where we assume a one dimensional chain with a single orbital per lattice site and one electron per orbital. Thus, the orientation of the electron spin is the only degree of freedom. The exchange interaction can be modelled by considering a virtual hopping process, where one electron temporarily hops to an adjacent site and back again. These hopping processes result in a decrease of kinetic energy of the system as described by the tight-binding model. However, they are only allowed if the spin of the electron on the adjacent site is of opposite sign, since otherwise two electrons with the same spin quantum number would be present in the same orbital. This, however is forbidden by the Pauli exclusion principle. Thus, an anti-parallel alignment results in an energetically favoured state of the system. The coupling constant $J$ can be written in first order as

$$J = -4t^2/U \quad , \tag{2.4}$$

where $t$ and $U$ are the hopping matrix element and the on-site repulsion from Eq. 2.2, respectively. In transition metal oxides the next nearest neighbour of a cation is usually an oxygen anion with a fully occupied $2p$ shell. These overlap with the $3d$ orbitals of the transition metal and can thus mediate the exchange interaction, between two transition metal cations. In this case, one speaks of a superexchange interaction. In first order, it can be modelled by four consecutive hopping processes. Foremost, one oxygen electron is hopping from the oxygen to the first cation, followed by the transfer of an electron from the second cation into the now empty oxygen orbital. Step three and four are the same processes in reverse and restore the system into its initial state.

## 2.4. Exchange interaction in a orbital degenerate 1D-chain

Up to now, we only considered one orbital per lattice site, which is only appropriate if the partly filled orbital is completely non-degenerate. Therefore, the case where electrons can occupy two different degenerate orbitals on every lattice site shall also be discussed[1]. In this case two electrons with the same spin are allowed to be situated on the same lattice site without violating Pauli's exclusion principle since they now differ in their

[1] The given arguments are also valid for more degenerate orbitals.

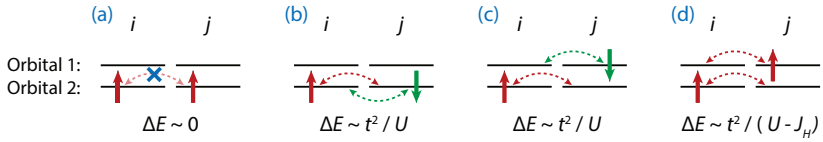


**Figure 2.1.:** Exchange interactions between two degenerate orbitals. Image after [26]

orbital quantum number. If we assume a ground state with one electron per lattice site there are four possible configuration for adjacent sites which are shown in Fig. 2.1. In case (a) and (b) the same orbital is occupied on all lattice sites and if we assume that no hopping processes between non-identical orbitals are allowed these cases are identical to a non-degenerate 1D-chain. This assumption is valid if the orbitals are aligned perfectly orthogonal with respect to each since in this cases the transition matrix element between them is vanishing. Thus, an antiferromagnetic alignment (b) is preferred since only in this case the transition between adjacent sites is allowed. In case (c) and (d) the electrons on adjacent sites are occupying different orbitals. Therefore, the electrons can always hop between the sites since the corresponding orbital on neighbouring site is always empty. In case (c) the energy gain from the exchange is identical to case (b). However, in case (d) both electrons are aligned parallel during the virtual hopping process. This is energetically favoured, since a parallel alignment minimizes the on-site Coulomb repulsions due to the intra-atomic coupling of the electron, which is also known as Hund's coupling. Therefore the on-site Coulomb repulsion $U$ is lowered by the the energy gain from the intra-atomic coupling $J_H$. Consequently, the most favourable ground state in a degenerate 1D-chain with one electron is the ferromagnetic alignment of the electron spin together with an antiferroorbital occupation, e.g. an alternating occupation of different orbitals on adjacent sites.

## 2.5. Goodenough-Kanamori-Anderson-Rules

In the last sections only simple cases have been discussed, which i.e. neglects that transition between orbitals with different angular quantum numbers usually are weakly allowed. Therefore, the findings on the exchange interactions cannot generally be applied to any system. However, Goodenough, Kanamori, and Anderson found a set of empirical rules [27–29] that has proven to correctly predict the exchange interactions for many transition metal oxides:

- The superexchange interaction between two magnetic cations with partially filled $d$ shells under an cation-ligand-cation angle of 180° is strongly antiferromagnetic.
- The superexchange interaction between two magnetic cations with partially filled $d$ shells under an cation-ligand-cation angle of 90° is ferromagnetic but weak.

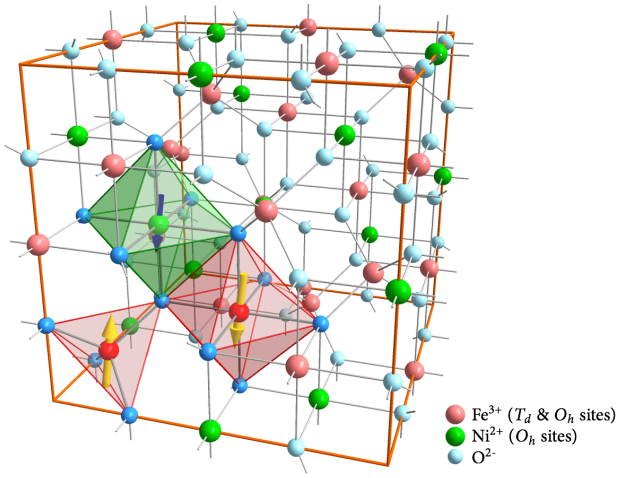


**Figure 2.2.:** Schematic representation of the inverse spinel lattice of $NiFe_2O_4$: $Fe^{3+}$-cations (red) are distributed equally across tetra- ($T_d$) and octahedral ($O_h$) lattice sites, while $Ni^{2+}$-cations (green) occupy $O_h$ sites. An antiferromagnetic coupling between the $T_d$ and $O_h$ sites compensates the magnetic moments of the $Fe^{3+}$-cations, why only the $Ni^{2+}$-cations account for the net macroscopic magnetization of $2\,\mu_B$/f.u.

- The exchange interaction between a magnetic cation with partially filled $d$ shell and a magnetic cation with full or empty $d$ shell under an cation-ligand-cation angle of 180° is ferromagnetic but weak.

These rules can be applied to the cations in the spinel crystal structure of $NiFe_2O_4$ to describe the formation of the observed ferrimagnetic order, as will be discussed in section 2.7. The localization of the $3d$ electrons together with the exchange interaction is able to explain the simultaneously occurring insulating and ferrimagnetic behaviour of $NiFe_2O_4$.

## 2.6. The spinel crystal structure

$NiFe_2O_4$ crystallizes in the spinel structure which is cubic with space group $Fd\bar{3}m$. Spinels can be denoted by the general formula $AB_2O_4$. Hereby, A labels a divalent and B a trivalent transition metal cation. The spinel structure is formed by a fcc sublattice of oxygen anions, whose interstitial tetrahedral (octahedral) sites are filled to one eighth (one half) by the transition metal cations. The spinel unit cell includes 56 atoms: 32 oxygen ($O^{2-}$), 16 trivalent metal cations ($B^{3+}$) and 8 divalent metal cations ($A^{2+}$). The spinel structure can be divided into the normal and the inverse spinel structure. In the normal one all divalent $A^{2+}$ (trivalent $B^{3+}$) cations occupy tetrahedral $T_d$ (octahedral $O_h$) lattice sites solely, while

in the inverse structure trivalent $B^{3+}$ cations are distributed equally across $T_d$ and $O_h$ sites and the divalent $A^{2+}$ cations only occupy $O_h$ sites. Also a mixture of both structures is possible which is quantified by the inversion parameter $\lambda$. Hereby, $\lambda$ is the fraction of $A^{2+}$-cations occupying $O_h$ sites, with $\lambda = 0$ denoting a normal ($A^{2+}[B^{3+}B^{3+}]O_4$) and $\lambda = 1$ a fully inverse ($B^{3+}[A^{2+}B^{3+}]O_4$) spinel lattice. Bulk $NiFe_2O_4$ crystals exhibit an ideal inverse spinel lattice with a cubic lattice parameter of $a = 8.338$ nm [30]. The unit cell of the inverse spinel structure of $NiFe_2O_4$ is exemplarily shown in Fig. 2.2.

## 2.7. Magnetism of $NiFe_2O_4$

The oxide $NiFe_2O_4$, together with $CoFe_2O_4$, $MnFe_2O_4$ and $Fe_3O_4$ belong to the class of ferrimagnetic spinels with a Curie temperature $T_C$ way above room temperature. Bulk $NiFe_2O_4$ shows ferrimagnetic ordering up to $T_C = 865$ K [11] which originates from a couple of exchange interaction between the cations in the spinel structure. Hereby, the strongest coupling arises from the superexchange interactions between the $Fe^{3+}$ cations on octahedral (B-sites) and tetrahedral (A-sites) lattice sites (Fig. 2.3(a)). The exchange is mediated by an overlap of the Fe $3d$ orbitals with the intermediate oxygen $2p$ orbitals in an angle of $\approx 125°$, which according to the Goodenough-Kanamori-Anderson-Rules (see sec. 2.5) results in a strong antiferromagnetic coupling between the cations on tetrahedral and octahedral sublattices. This intersublattice superexchange interaction was found to have a strength of $J_{AB} = -25.0\,k_B$ [31]. Additionally, the ferromagnetic ordering of the cations on the octahedral B-sites is stabilized via a 90° intrasublattice superexchange interaction among themselves with a strenghth of $J_{BB} = 4.2\,k_B$ (Fig. 2.3(b)) [31]. The intrasublattice super-exchange interaction between cations on tetrahedral A-site is antiferromagnetic with a strength of $J_{AA} = -4.0\,k_B$ [31]. However, it does not result in an antiferromagnetic ordering of the A-site cations since it is superimposed by the already mentioned stronger exchange interactions. Finally, the Fe and Ni cations on octahedral B-sites are ferromagnetically coupled by a double-exchange interaction (Fig. 2.3(c)). Hereby, one electron from the divalent Ni is transferred to an empty Fe $3d$ level and back. Though, this interaction is very weak and thus masked by the superexchange interactions. All together, these exchange interactions result in the formation of two ferromagnetic ordered sublattices which are aligned antiferromagnetically with respect to each other (Fig. 2.3(d)). The octahedral (B) sublattice is populated by $Fe^{3+}$ cations with 5 unpaired electrons in the $3d$ shell and $Ni^{2+}$ cations with 2 unpaired electrons, resulting in a net magnetic of $7\,\mu_B$/f.u.. The tetrahedral (A) sublattice which is only populated by $Fe^{3+}$ cations accounts with $5\,\mu_B$/f.u.. Thus, both sublattices do not compensate each other completely resulting in a net magnetic moment of $2\,\mu_B$/f.u. for the bulk $NiFe_2O_4$ spinel structure.

The crystal field from the oxygen anion surrounding the $3d$ cations is splitting the $3d$ levels into two manifolds which are each spherically symmetric, i.e. whose total angular momentum vanishes if they are fully occupied in one or both spin channels. An octahedral

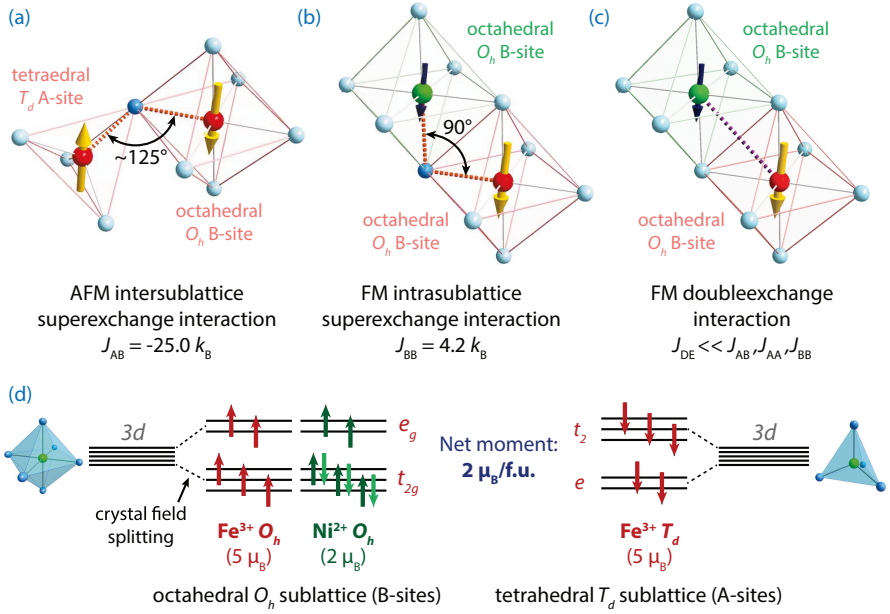


**Figure 2.3.:** (a-c) Exchange interactions in $NiFe_2O_4$: (a) AFM superexchange interaction between cations on tetraedral $T_d$ and octahedral $O_h$ lattice sites, (b) FM superexchange interaction between cations on octahedral $O_h$ lattice sites, (c) FM doubleexchange interaction between cations on octahedral $O_h$ lattice sites. (d) Occupation of the magnetic sublattices in the inverse spinel structure of $NiFe_2O_4$. Additionally, the splitting of the 3*d* levels due the crystal field is depicted.

lattice site symmetry results in a splitting into the lower lying threefold degenerate $t_{2g}$ and the higher lying twofold $e_g$ manifold. In a tetrahedral symmetry both manifolds are reversed, where the now lower lying twofold manifold is denoted *e* and the higher lying one $t_2$. The resulting term scheme is governed by Fig. 2.3(d) and demonstrates that each manifold is either half or fully occupied in $NiFe_2O_4$. Thus the total angular momentum is quenched on every lattice site, which explains the small observed magneto-crystalline anisotropy. The even occupation of the possible angular quantum numbers in the 3*d* states causes any effect due to the spin orbit coupling to mostly cancel out. Therefore, the spins are not locked to the alignment of the orbital states which are coupled to the symmetry of the lattice, thus suppressing a direction dependence of the spin alignment. In contrast, in $CoFe_2O_4$ ($3d^7$ configuration) one state is unoccupied in the $t_{2g}$ levels, whose spin is thus strongly coupled to the lattice by the spin orbit interactions. This in turn causes the strong magneto-crystalline anisotropy observed in $CoFe_2O_4$.

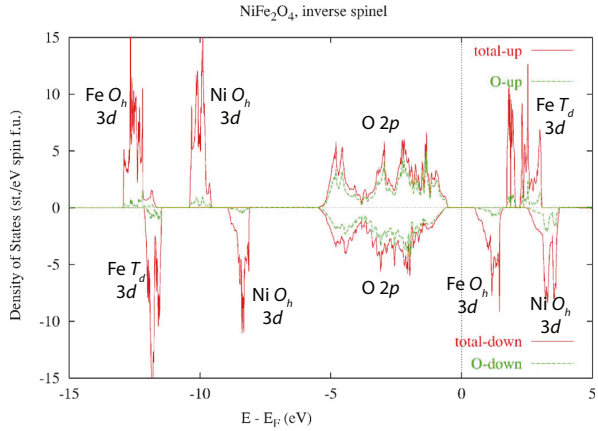


**Figure 2.4.:** Calculcated spin dependent total density of states (DOS) of $NiFe_2O_4$ in the inverse spinel structure. The majority DOS is shown in the upper half, while the minority DOS is on the negative side of the $y$ axis. The atomic species, which is mainly contributing to the different bands are denoted. (Image adopted from [32])

## 2.8. Electronic structure

The electronic structure of $NiFe_2O_4$ has been investigated theoretically by density functional theory (DFT) using the self-interaction corrected local spin density (SIC-LSD) approximation [32, 33]. The calculations were performed for the normal and inverse spinel configuration individually, whereby the authors found the resulting spin magnetic moment as well as the exchange splitting in $NiFe_2O_4$ to significantly increase, when going from the bulk-like inverse to the normal spinel structure. However, energy considerations revealed this transition to be very unfavourable and found the inverse spinel structure as the ground state configuration of $NiFe_2O_4$. The resulting total density of states (DOS) for the inverse spinel case is depicted in Fig. 2.4. A theoretical band gap of 0.98 eV was determined, while the exchange splitting of the conduction band is $2\Delta E_{Ex} = 1.21\,\text{eV}$. The valence band is predominantly formed by O $2p$ states, while the conduction band minimum of the majority (minority) states is formed by the unoccupied $3d$ levels of Fe cations on tetrahedral (octahedral) lattice sites.

## 2.9. Spin filtering

Magnetic insulators offer a promising approach for the creation of highly spin-polarized electron currents. Hereby, the magnetic insulator is integrated as a very thin barrier between two conducting electrodes, as depicted in Fig. 2.5. Due to the magnetic behaviour of the barrier the lowest lying conduction band above the Fermi level is spin split, as

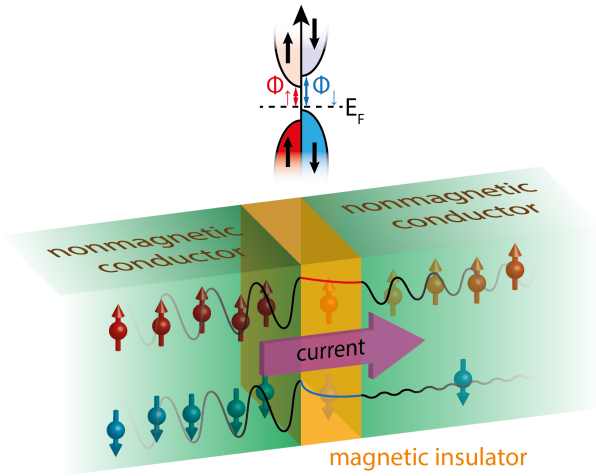


**Figure 2.5.:** Schematic drawing of a spin filter tunnel barrier. The spin-dependent barrier height $\phi$ of the magnetic insulator results in a highly spin-dependent tunnelling probability through the barrier. Hereby, the filtered electrons theoretical can reach a spin polarization of up to $P = 100\,\%$.

already discussed for the case of $NiFe_2O_4$ in the last section (see also Fig. 2.4). The spin-split conduction band result in a spin-dependent tunnelling barrier height $\Phi_{\uparrow\downarrow}$. Thus, the transition probability for any electron current passing through the barrier is highly spin-dependent. In contrast to ferromagnet/insulator/ferromagnet (FM/I/FM) tunnel junctions, the spin selectivity of a spin filter tunnel barrier does not predominantly depend on the available states in the second electrode.

For a non-magnetic tunnel barrier of thickness $d$, the transmission probability through the barrier is known to be

$$T = \exp\left(2d\sqrt{\frac{2m}{\hbar^2}\left(\Phi - E_{\text{kin}}\right)}\right), \tag{2.5}$$

where $m$ is the mass of the tunnelling particle, e.g. the electron, $E_{\text{kin}}$ its kinetic energy, and $\Phi$ is the barrier height, e.g. the offset between the lowest lying conduction band and the Fermi level $E_F$. In case of a magnetic insulator, the conduction band is split by the exchange energy $2\Delta E_{\text{exch}}$, which results in the spin-dependent barrier height $\Phi_{\uparrow\downarrow}$:

$$\Phi_{\uparrow\downarrow} = \Phi_0 \pm \Delta E_{\text{exch}} \tag{2.6}$$

Since the transmission probability exponentially depends on the square-root of the barrier height, it is obvious that already a minor spin-dependent splitting of the barrier can cause

a high difference in the transmission probability. The filtering efficiency of a spin-filter can be characterized by the spin-polarization $P$, which is defined as:

$$P = \frac{T_\uparrow - T_\downarrow}{T_\uparrow + T_\downarrow} \,. \tag{2.7}$$

CHAPTER 3

# Experimental methods

This chapter introduces the experimental methods applied in this work. First, the pulsed laser deposition technique, which was used for the growth of the spinel ferrite films investigated in this thesis, will be discussed. Afterwards, the methods utilized for structural and magnetic characterization of the samples will be presented. Finally, all applied synchrotron based X-ray spectroscopy techniques will be addressed.

## 3.1. Pulsed laser deposition (PLD)

Pulsed laser deposition is a powerful method for the thin film deposition of complex oxides. The desired film material is initially present as a target disk, which is prepared from stoichiometric powder or single crystals of the material. High-energtic laser pulses are focused onto the target, which are absorbed on a small spot of the target material (see Fig. 3.1). There, they instantaneously generate a plasma of neutral and ionized species from the target material. Due to the high energy density at the laser focus, the ablation process is far from equilibrium conditions. Thus, differing melting points of the individual ion species are of minor importance and the stoichiometry of the target material is basically preserved in the plasma. The plasma is forming a plume which is oriented orthogonal on the target surface towards the substrate. The particles in the plasma are moving in direction of the substrate, where they nucleate on the surface and start forming a film. The kinetic energy of the particles can be influenced by adjusting the background pressure in the deposition chamber. The substrate is glued on top of a heater, which allows to keep it at temperatures of up to 850 °C during growth, to provide sufficient surface mobility of the absorbed adatoms as is necessary for epitaxial growth.

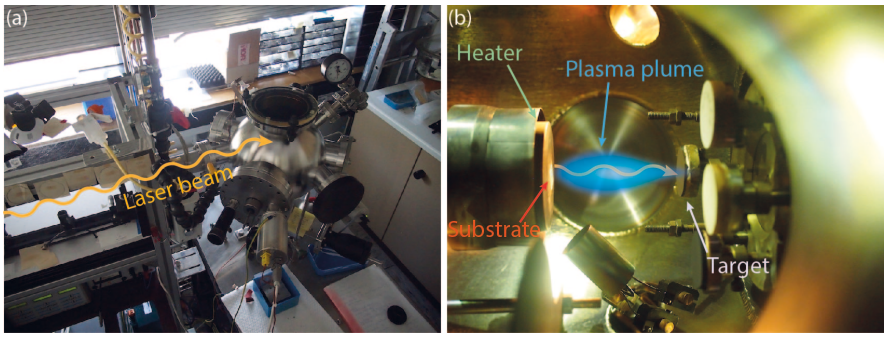


**Figure 3.1.:** Pictures of the PLD setup: (a) The PLD vacuum-chamber is situated at the end of the laser beamline. (b) Laser pulses are focussed onto the target material, which is vaporized by the pulse energy into a plasma plume. Afterwards, the ablated material is deposited on a substrate which is mounted on a heater.

In this work a deposition chamber assembled by Neocera Inc. was used[1], together with a 50 W KrF excimer laser. The laser has a wavelength of $\lambda = 248\,\text{nm}$, a pulse length of $t = 25\,\text{ns}$ and an adjustable repetition rate between $f = 1\,\text{Hz}$ and 50 Hz. The laser fluence at the target is determined by the laser pulse energy and the size of the focusing spot on the target. The former can be adjusted by a beam attenuator in front of the chamber, the latter by adjustable slits in the laser beam path. Inside the chamber, the substrate is mounted in a distance of 50 mm away from the target.

The energy of the laser pulses is measured by a thermal power sensor, which can be placed in the beam path. From this, the laser fluence $J$ is calculated using the laser spot size on the target, which has dimensions of $3.3\,\text{mm} \times 0.7\,\text{mm} = 4.6\,\text{mm}^2$. Finally, the value needs to be corrected for the absorption of the focussing lens and the fused quartz glass window of the vacuum chamber. Both together have a transmissibility of 50 %.

The deposition process takes place in a high vacuum chamber with a base pressure of $1 \times 10^{-7}$ mbar, which offers the possibility to introduce oxygen or argon gas. The background gas pressure and mixture during the deposition is adjusted by controlling the inflow rates of the gases using mass flow meters. Depending on the chosen growth parameters deposition rates of up to several 100 Å $\text{min}^{-1}$ can be achieved using PLD. The optimized growth parameters for $NiFe_2O_4$ thin films, which are worked out in chapter 4, result in a deposition rate of 7-8 Å $\text{min}^{-1}$.

[1] We thank R. Dittmann for providing us the PLD setup and the Peter-Grünberg-Institut (PGI-7) for providing us the possibility to perform measurements on the Philips XPert MRD diffractometer.

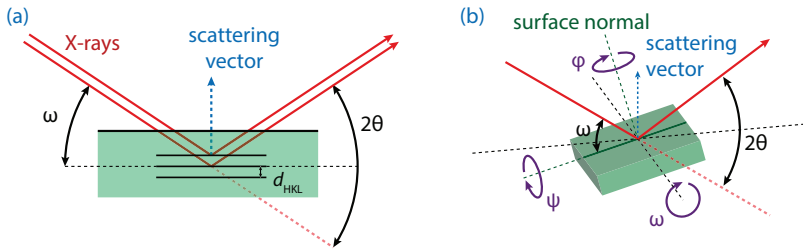


**Figure 3.2.:** Experimental geometry of an XRD experiment. (a) X-ray diffraction occurs, if the scattering vector matches a reciprocal space vector which is aligned perpendicular to the corresponding set of lattice planes. (b) Possible rotation angles of the sample in a four-circle X-ray diffractometer.

## 3.2. X-ray diffraction (XRD)

X-ray diffraction (XRD) is utilized for the ex situ structural characterization of the thin films. A X-ray beam traversing a crystal solid interacts with the electronic structure of the lattice and is scattered. Since the electrons are distributed periodically in the crystal the scattered X-rays interfere with each other. Constructive interference is only allowed, if the Bragg-equation is fulfilled,

$$n\lambda = 2d\sin(\theta)\,, \tag{3.1}$$

e.g. the beam is scattered by parallel lattice planes with distance $d$ between the planes under a scattering-angle of $2\theta$. If the scattered beam is not suppressed by symmetry conditions of the Bravais lattice the process results in a coherent diffraction which can be detected.

All XRD experiments in this thesis were performed on a four-circle Philips XPert MRD diffractometer[1] using Cu-K$\alpha$-radiation, with a wavelength of $\lambda = 0.154\,18$ nm. The experimental geometry is depicted in Fig. 3.2. A Bragg-Brentano setup was used to perform $\theta$-$2\theta$-scans with a scattering vector parallel to the surface normal. In this configuration, only lattice planes parallel to the surface result in diffraction peaks in the scans. Their positions can be used to calculate the lattice constant perpendicular to the surface (out-of-plane lattice constant $a_{\mathrm{OOP}}$) of the grown film using the Bragg equation (Eq. 3.1), whereby $n$ denotes the order of the corresponding reciprocal lattice vector. In a heterostructure, the lattice constant of an overlying film is in general not matching that of the substrate. Deviations of the out-of-plane lattice constant $a_{\mathrm{OOP}}$ of the film from its bulk-value indicate the incorporation of strain by e.g. defects, while an unmodified $a_{\mathrm{OOP}}$ indicates that the film is grown fully relaxed. Furthermore, parasitic phases can be identified in a $\theta$-$2\theta$-scan, since they result in additional diffraction peaks. This allows to determine if a film is growing uniformly.

Phi-scans were used to discover the orientation of the grown film with respect to the substrate, i.e. if the film grows cube-on-cube, is rotated, or even grows as crystallites with identical out-of-plane orientation, but different in-plane orientations rotated relative to one another. Before starting a phi-scan, the sample and the diffractometer are aligned so that a diffraction peak of the film with an in and out-of-plane component becomes visible. Afterwards, the sample is scanned while turning it around its surface normal. Hereby, the number of observable reflections during one rotation of $\phi$ by 360° reflects the symmetry of the film, e.g. a cubic lattice has a four-fold rotational symmetry resulting in four equidistant reflections in a $\phi$ scan. By repeating the $\phi$ scan for a reflection of the substrate, one can evaluate the alignment of the film relative to the substrate.

## 3.3. X-ray reflectivity (XRR)

Since the used PLD-setup provides no option for in situ thickness monitoring of the film growth, the thickness of all samples was determined after deposition by means of X-ray reflectivity. Hereby, a $\theta$-$2\theta$-scan with very small incidence angles ($0° < \theta < 3°$) is performed, which results in a reflection of the X-ray beam at flat planes. Since the reflection at the surface interferes with the reflections from the underlying interfaces, the measured intensity of the $\theta$-$2\theta$ shows interference fringes, which are called Kiessig fringes [34]. From the distance $\Delta\theta$ between the intensity maxima the film thickness $d$ can be determined by the relation,

$$d = \frac{\lambda}{2 \sin \Delta\theta} \,. \tag{3.2}$$

However, the accuracy of the given formula is limited for thin films since the interference oscillations become very broad, i.e. for a 4 nm thick $NiFe_2O_4$ film they have a width of $\Delta\theta \approx 1°$. Therefore, the measured reflectivity curve is modelled using the Parratt-formalism [35], which considers the thicknesses and the refractive indices of the layers in the system, as well as the roughness between the layers. The model curve is fitted to the experimental data utilizing the software X'Pert Reflectivity, which employs a genetic algorithm and the thickness is determined from the result of the fit. Yet, since for ultra thin films Kiessig fringes are often no more observable (e.g. for $d \leq 2$ nm), the application of XRR for thickness determination is not appropriate any more in this case.

## 3.4. SQUID magnetometry

For the characterization of the bulk magnetic properties of the samples SQUID magnetometry is used. Here, a MPMS XL SQUID by Quantum Design[2] is used, which allows us

[2] We thank the Jülich Centre for Neutron Science (JCNS-2 / PGI-4) for providing us the possibility to perform measurements on the Quantum Design MPMS

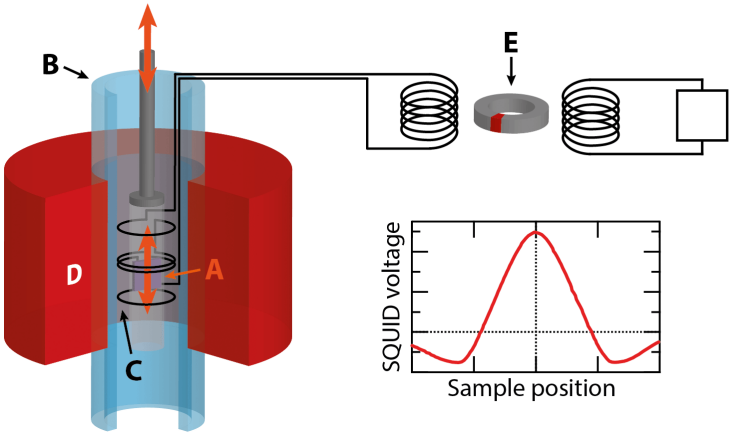


**Figure 3.3.:** Schematic drawing of a SQUID magnetometer.

to resolve magnetic signals down to $10^{-8}$ emu[3]. The sample (A) is positioned in a sample chamber (B) which can be cooled down to 2 K. There, it is surrounded by the pick-up coil for detection (C) of the magnetic response and a superconducting magnet (D), which generates the external applied magnetic field. The detection coil is made from a single piece of superconducting wires, that is configured as a second derivative gradiometer. The wire is forming four loops: Two clockwise wound loops at the centre, as well as one counter-clockwise below and one above the center loop pair. The advantage of this setup is that it cancels out any magnetic field changes which passes all loops, i.e. small drifts of the applied external field. Yet, by moving the sample through the detection coils the sample's dipole field still induces local changes of the magnetic flux, which leads to a change in the persistent current in the detection circuit proportional to the change in magnetic flux. Finally, the SQUID (E) acts as a highly linear current to voltage converter, that allows to detect any change in the magnetic flux as variation of the SQUID output voltage. The voltage is then recorded as a function of the sample position and the resulting curve is fitted with the theoretical curve of an ideal dipole. From the fit, the magnetic moment $M$ of the sample can be extracted [36].

One disadvantage of SQUID magnetometry is that it detects the magnetic response of the whole sample, i.e. of the substrate and all deposited films. Thus, to extract the magnetic response from one film only, one has to remove all other contributions properly, as discussed in the following.

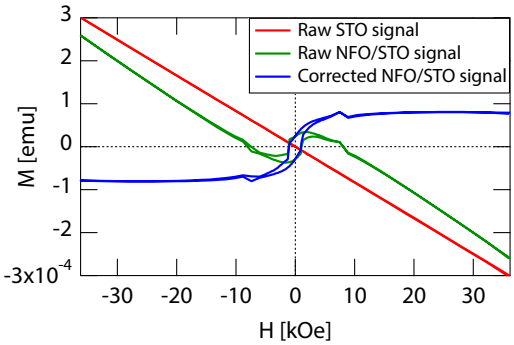


**Figure 3.4:** Exemplary presentation of the contribution from the substrate background signal on the resulting total signal in SQUID measurements. The red line reflects the pure diamagnetic response of $SrTiO_3$, while the green line is the recorded hysteresis loop from a $NiFe_2O_4$ film grown on $SrTiO_3$. To extract the signal from the film (blue line) the contribution from the substrate has to be substracted.

### 3.4.1. Background substraction

All samples discussed in this thesis are grown on $SrTiO_3$ substrates, which is a diamagnetic material. Thus, all recorded hysteresis loops are dominated by a diamagnetic contribution of the substrate, as exemplary depicted by the green line in Fig. 3.4. To extract the magnetic response of the films, a subtraction of the diamagnetic background is required. Therefore, ideally the hysteresis loop of every used substrate is recorded at the same conditions where the final hysteresis loop is recorded (red line in Fig. 3.4) before the deposition of the film, and the two loops have to be subtracted by each other. However, this approach is quite cumbersome and the corrected signal can also be extracted from the raw film plus substrate hysteresis loop solely. Therefore, linear slopes are fitted to the high-field tails of the raw signal and the resulting line is subtracted. However, this approach is only suitable, if the substrate has a purely linear response. In the presented experimental data, the resulting signal of the film (blue line in Fig. 3.4) often includes an artefact (e.g. visible at 8 kOe in Fig. 3.4), which originates from the zero-crossing of the raw signal.

## 3.5. Atomic force microscopy

The surface roughness and morphology of a sample can be determined by atomic force microscopy (AFM) scans. AFM is recording the attractive and repulsive forces that are acting on an atomic sharp tip in the vicinity of the scanned surface, which is attached to an elastic cantilever. In this thesis all scans are performed in tapping mode. Hereby, the cantilever is driven to oscillate near to its resonance frequency. The frequency is measured by a laser that is focused onto the backside of the cantilever and reflected into a segmented photo-diode. Atomic interactions between tip and surface atoms cause a bending of the cantilever in dependence of the surface topography, which causes a shift of

[3] 1 emu = $10^{-3}$ J $T^{-1}$

the cantilever's oscillation frequency. The shift is compensated by a piezo-motor which is moving the cantilever along the $z$-axis. From these movements, the surface morphology of a sample can be recorded while scanning the tip over the surface. AFM allows a vertical resolution of down to 1 Å and a spatial resolution below 100 nm. All AFM surface scans of substrates and deposited thin films presented in this thesis were performend on a SIS Pico Station[4] or an Asylum Research Cypher AFM in tapping mode.

The roughness of the films can be quantified by the root mean square (RMS) $\sigma_{\mathrm{RMS}}$ which is determined by the standard deviation of the surface heights from the average.

$$\sigma_{\mathrm{RMS}} = \sqrt{\sum_i \frac{1}{N} (z_i - \bar{z})} \tag{3.3}$$

One should bear in mind, that the calculation only delivers suitable values, when the surface scan is free of any artefacts. Thus, if instrumental artefacts are present, they have to be corrected in advance. Likewise, any dirt-particles which are clearly not attributed to the surface have to be excluded from the calculation.

## 3.6. X-ray Core Level Spectroscopy

Core level spectroscopy techniques are powerful methods to investigate the electronic structure of solids. In particular, they allow to probe element-specifically. In this work, X-ray photoelectron spectroscopy (XPS) and X-ray absorption spectroscopy (XAS) are employed, which both rely on the excitation of bound electrons by photons. In contrast to (in)elastic photon scattering experiments, both methods are based on a first-order optical absorption process, in which only one photon is involved. In the case of XPS, the absorption results in the excitation of a deeply bound core electron into a continuum state above the ionization threshold, which afterwards can be detected as a photoelectron if its kinetic energy is sufficiently large to escape from the solid. In XAS, on the other hand, only the absorption of the incident light is recorded. Thus, the core electron can also be excited into an empty state in the conduction band below the ionization threshold. In both cases, the photon energy of the incident light needs to be of the same order or larger than the binding energy of the core electron, which is why X-ray light sources are required. All X-ray spectroscopy data presented in this thesis has been recorded using synchrotron radiation from the electron storage ring BESSY-II at the Helmholtz-Zentrum Berlin. Using synchrotron radiation was mandatory, since the acquisition of XAS spectra requires a tunable soft X-ray source, which can only be realized at a synchrotron facility. Furthermore, in hard X-ray photoelectron spectroscopy (HAXPES) experiments the photoionization cross section is magnitudes lower than for soft X-rays, resulting in a highly reduced photoelectron yield. Therefore, HAXPES experiments demand for a high

[4] We thank the Peter-Grünberg-Institut (PGI-7) for providing us the possibility to perform measurements on the SIS Pico Station AFM

flux X-ray light source, e.g. a synchrotron facility, to archive reasonable photoelectron counting rates.

### 3.6.1. X-ray absorption spectroscopy

In X-ray absorption spectroscopy (XAS) experiments, the absorption of an X-ray beam which is transmitted through a solid is recorded as a function of the photon energy $h\nu$. The X-ray absorption process is quantified by the linear absorption coefficient $\mu$, which is defined by the amount of intensity that is absorbed from an X-ray beam with initial intensity $I_0$ while passing a sample of thickness $x$,

$$dI(h\nu) = \mu(h\nu)\, I(h\nu)\, dx \quad \Leftrightarrow \quad I(h\nu) = I_0(h\nu)\, \exp\left(-\mu(h\nu)\, x\right) . \tag{3.4}$$

The absorption coefficient can be determined straightforwardly in a **transmission experiment**, whereby the beam intensity is measured before ($I_0$) and after ($I$) passing the sample, and $\mu$ can be calculated using Eq. 3.4. However, this approach has the disadvantage that only very thin samples can be measured, since otherwise the X-ray beam is damped below the detection limit. The feasible sample thickness for such an experiment can be estimated from the X-ray attenuation length $\lambda_{\mathrm{EAL}}$, which is the inverse of the absorption coefficient $\lambda_{\mathrm{EAL}}(h\nu) = 1/\mu(h\nu)$. Alternatively, the photon absorption can be measured by detecting secondary processes, like (i) the sample fluorescence or (ii) secondary electrons. Both cases rely upon the recombination processes, where the initially excited electron falls back into its ground state. The released energy is then transferred either into the creation of photons, which is called fluorescence, or into the excitation of secondary Auger electrons.

In case (i), the intensity of the fluorescence can be easily detected using a photon detector and is directly related to the absorption coefficient. The advantage of the **fluorescence yield (FY)** detection is that the attenuation length of fluorescence radiation is of the same order as the attenuation length of the incident X-ray beam $\lambda_{\mathrm{EAL}}$. Thus, a probing depth of several µm can be realized using this mode.

For (ii), the excited Auger electron can travel towards the sample surface and escape from the sample. On their way through the sample, they excite secondary electrons which can also escape, thus forming an electron cascade. The sum of all electrons that are leaving the sample is called **total electron yield (TEY)**. It can be detected by measuring the current from ground towards the sample, that replenishes the missing electrons and that is thus related to the X-ray absorption coefficient. The advantage of the TEY detection mode is the amplification of the absorption signal by the electron cascade, resulting in the possibility to detect even very small deviations of $\mu(h\nu)$. On the other hand, the probing depth of this mode is limited by the mean free path of the Auger electrons. Only electrons originating from the uppermost few nm of the sample can escape the sample and thus limit the probing depth. Additionally, the sample needs to be conductive, for that electrons can replenish the created holes.

The determined absorption coefficient $\mu$ includes contributions from elastic and inelastic scattering and absorption due to the photoexcitation of core electrons. Hereby, the latter one is of major interest since it includes the information from the electronic structure of the sample. In this thesis, XAS spectra are only recorded for XMCD experiments, which will be discussed later.

### 3.6.2. The photoexcitation process - Fermi's golden rule

To understand the details of XPS and XAS spectra, like the intensity or shape of spectral lines, we discuss the interaction of light with matter. The crucial step in both mechanisms is the photoexcitation process, which describes the excitation of an electron in the crystal by an incoming photon. In the initial ground state of the probed atom in the solid all electrons are in their energetically most favourable state. After excitation, the atom is present in an excited (final) state, in which a core-hole is created and the excited electron is occupying an unoccupied state above the Fermi level.

For the theoretical description of this process, the many body Hamiltonian $H$ for the electron system of the solid is solved, resulting in the ground state $\phi_i$ and all possible excited states $\phi_n$ of the electron system. If one neglects the inter-atomic interactions in a solid, the many body Hamiltonian reduces into a single particle one. The incoming photon is treated as electromagnetic radiation, which causes a small perturbation to the system. Thus, the possible transition can determined by means of perturbation theory. The derivation of this approach is documented in standard textbooks [37, 38] and results in Fermi's Golden Rule, which gives the probability $W$ of a transition from the ground state $\phi_i$ into an allowed final state $\phi_f$. The Golden Rule is defined as:

$$W \sim \left|\left\langle \phi_f \left| \mathbf{T} \right| \phi_i \right\rangle\right|^2 \delta(E_f - E_i - h\nu) \tag{3.5}$$

Hereby, $h\nu$ is the photon energy, thus the delta function satisfies the energy conversion law, and $\mathbf{T}$ is the transition operator between the two states. From this equation it is obvious, that the shape of the measured spectra essentially depends on the possible initial as well as the possible final states. Another key result from the Golden rule are the dipole selection rules, which state that only transition between initial and final states with certain quantum numbers are allowed ($\Delta J = 0, \pm 1$, $\Delta M_J = 0, \pm 1$, $\Delta S = 0$).

Core level spectroscopy always investigates the excitation of a deeply bound core electron (which is equivalent the creation of a core hole), which is strongly localized and has almost no overlap with adjacent atoms in a lattice. Therefore, both XAS and XPS are only sensitive to the electronic properties within the atomic volume of the probed atom. In consequence, both spectroscopic techniques allow to probe the sample element-specifically. This is a major advantage for investigating compounds like $NiFe_2O_4$, that are consisting of multiple cation species, since it allows to probe each ion species individually.

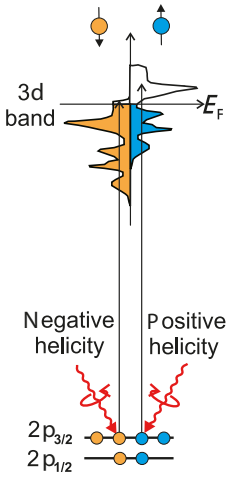


**Figure 3.5:** Schematic representation of the XMCD process. First, polarized X-rays create spin-polarized photoelectrons which are, in a second step, detected by the exchange split valence shell (Figure from [39])

### 3.6.3. XMCD

If an X-ray absorption experiment is performed on a ferromagnetic sample using circular polarized X-rays[5], absorption spectra that have been recorded under reversed polarization or magnetization differ. This effect is called X-ray magnetic circular dichroism (XMCD) and can be schematically explained in a single electron picture by a two step process. First, polarized X-rays create spin-polarized photoelectrons which are, in a second step, detected by the exchange split valence shell as schematically depicted in Fig. 3.5.

In XAS experiments with unpolarized X-rays the incoming photons have a randomly oriented spin angular momentum $J_z$. Thus, any effects due to coupling between the moments of the photon and the excited electron is averaged. In contrast, circular polarized photons have a well defined spin angular momentum, whereby the quantization axis is defined parallel to the beam direction. During the photoexcitation process the photon transfers its angular moment to the excited electron. However, if the electron spin and angular moment are independent the excited electron could have an arbitrary spin orientation. However, any electron that is occupying a shell except the *s* shell ($l = 0$) is subject to the spin-orbit (LS) coupling. In this case, the angular moment of the photon is partially transferred to the spin orientation of electron, thus resulting in a spin-polarization of the photoelectrons.

In a second step, the polarized electron is filling an empty state in the conduction band. In a magnetic sample the valence and conduction bands are spin split, e.g. there are more empty states for one spin direction than the other. Thus, the valence band acts as a spin-detector and preferentially accepts electrons of one spin orientation. The latter argument would also be true for antiferromagnets, however the spin splitting of the

[5] and the polarization and magnetization vector are not perpendicular

valence band is alternating between adjacent lattice sites, whereby the effect is cancelled out.

The XMCD is also covered by the quantum mechanical description using Fermi's golden rule. Hereby, the possible initial ($\phi_i$) and final states ($\phi_f$) have an total angular momentum quantum number $J_{i,f}$ and a magnetic quantum number $m_{i,f}$. The dipole transition matrix element in Eq. 3.5 depends on these quantum numbers as well as on the polarization of the incoming photon. Thus, the transition probabilities $W$ are spin-dependent and can therefore describe the differences observed in a dichroic spectrum. A detailed derivation of these matrix elements can be found in [38, 39].

Experimentally, an XMCD spectrum is recorded by taking two XAS spectra with either reversed helicity of the incoming X-ray or reversed magnetization direction of the sample. The XMCD spectra is then given by the difference of the two absorption spectra.

$$\mu_{\mathrm{XMCD}}(h\nu) = \mu_{+}(h\nu) - \mu_{-}(h\nu) \tag{3.6}$$

The dichroic spectrum depends on the alignment between the polarization vector of the incident light and the magnetization vector of the sample. Therefore, the differences between two spectra are identical if either the light helicity ($\sigma^{+} \rightarrow \sigma^{-}$) or the magnetization direction ($\mathbf{M} \rightarrow -\mathbf{M}$) is switched. Experimentally, this has the advantage to record the XMCD difference spectrum in two different ways, which in turn allows to discriminate dichroic effects from artefacts.

XMCD spectroscopy is a powerful tool for probing magnetic materials with multiple cation species. First, the magnetic contribution to the net magnetization of each species can be probed individually. Furthermore, the comparison of XMCD spectra with model data from ligand field multiplet (LFM) calculations (see also App. B) allows to identify and quantify the local lattice site symmetry of each cation species. Both benefits are useful for analysing $NiFe_2O_4$, since it possesses two magnetic cations which are distributed across the octahedral and tetrahedral symmetric lattice sites in the spinel structure.

### 3.6.4. Photoemission spectroscopy

Historically, photoemission spectroscopy is based on the photoelectric effect, which first was described by H. Hertz [40]. He observed that upon the illumination of a metal with UV light, the material can start to emit electrons, which are called photoelectrons. Einstein found that, if the energy $h\nu$ of the absorbed photons is smaller than the energy required to remove an electron from the surface of the metal, no electrons are emitted regardless of the intensity of the light. Above this energy, which is called the work function $\phi$, electrons can overcome this potential and are emitted with a kinetic energy, equal to the difference between the energy of absorbed photon and the work function ($E_{\mathrm{kin}} = h\nu - \phi$)[41]. If a solid is penetrated by X-rays, their photon energy is high enough to not only eject valence electrons, but also deeper bound core electrons. Hereby, the kinetic energy of the photoelectrons is further decreased by the binding energy $E_{\mathrm{B}}$ of the core electron. Thus,

in a one-electron picture the energy of the photoelectron is determined as

$$E_{\text{kin}} = h\nu - E_{\text{bin}} - \phi \tag{3.7}$$

On this basis, photoemission spectroscopy was developed. By using monochromatic light and energy-dependent detection of the photoelectrons, it is possible to determine the binding energy of the photoelectrons in the investigated solid. While this picture is intuitive, in reality it is too simple, since it neglects the many body interaction of the remaining electrons. The creation of a core hole produces a final state in the system and due to energy conversion actually only the differences of the total energies between the initial state with $N$ electron and the final state with $N-1$ electrons can be measured by photoemission spectroscopy,

$$E_{\text{bin}} = E_f^{N-1} - E_i^N \ . \tag{3.8}$$

### 3.6.5. Three step model

For the description of the photoemission process the so called "three step model" was proposed [42]. In this approach the whole process is divided into three consecutive steps, which are each treated individually. While this model simplifies the underlying physics, it is very useful to qualitatively understand the recorded photoemission spectra. Often the model is even suitable for a quantitative interpretation. The three steps are discussed briefly in the following.

The initial step involves the excitation of an electron from an occupied initial state $i$ to an unoccupied final state $f$ above the Fermi level in a one electron picture. The transition has to follow the laws of energy and momentum conservation. Thus,

$$E_f = E_i + h\nu \quad \text{and} \quad \mathbf{k}_f = \mathbf{k}_i + \mathbf{k}_{\text{Photon}} + \mathbf{G} \ , \tag{3.9}$$

where $\mathbf{G}$ is a reciprocal lattice vector of the solid. The probability of an excitation in dependence of the photon energy is determined by Fermi's golden rule (Eq. 3.5). The latter has already been discussed earlier during the description of XAS and the photoexcitation process is substantially the same here. The only difference is that the final state must be higher in energy than the ionization threshold for that the electron can escape the solid as described in step two and three.

In a second step, the excited electron is travelling through the solid towards the surface. Hereby, the electron is subject to elastic and inelastic scattering events. While elastic scattering alters the electron's trajectory, inelastic scattering results in a transfer of kinetic energy from the photoelectron to the lattice. Thus, the photoelectron loses its information on the binding energy of the core level from which it originates from. Instead, it contributes to the inelastic background observed at higher binding energies than the core-level peak in the photoemission spectrum. The distance an electron can travel before

any scattering event is limited, which is described by the inelastic mean free path (IMFP). As a consequence only photoelectrons which are excited a few nm below the surface can reach it without scattering, thus limiting the information depth of photoemission spectroscopy. The latter aspect is described in more detail in section 3.6.7 and 3.6.8.

The third step describes the transition of photoelectrons from the solid into the vacuum, whereby it has to overcome the work function $\phi$. Hereby, the electrons are diffracted at the surface potential barrier and the perpendicular part $\mathbf{k}_\perp$ of the electron wave vector $\mathbf{k}$ is altered.

The accurate approach to describe the photoemission process is the so called one-step theory, which treats all discussed process on a unified footing. Hereby, an photon induced electric dipole excitation is considered, but the final state is not modelled as a local electronic configuration of the investigated atom. Instead, the wave function of the final state is represented as a time reversed LEED state. A LEED state describes the wave function of an electron that enters a solid and is damped there. Thus, the time-reversed function properly describes an escaping electron, while at the same time governing the effects due to scattering inside the solid and at the interface to the vacuum.

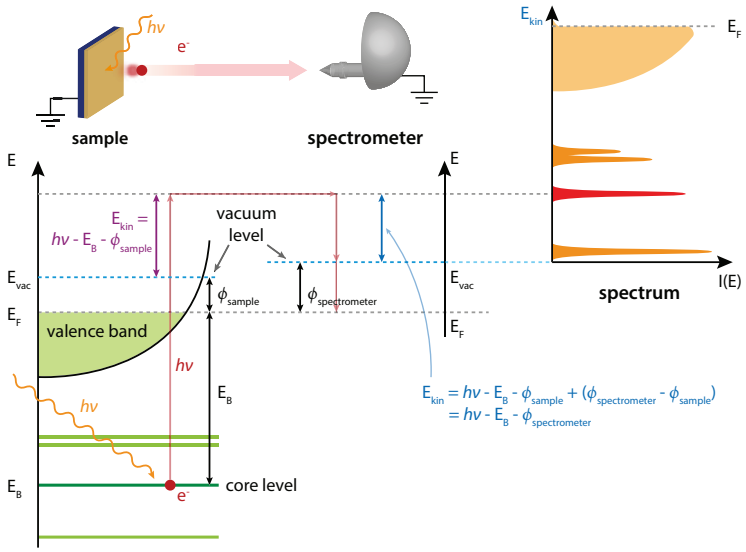


**Figure 3.6.:** Relation between the energy levels of the sample and the detector in a photoemission experiment if both are grounded to the same level. The right part depicts the measured spectrum. Adapted from [37].

### 3.6.6. Work function of the spectrometer

In equation 3.7, the work function is given as the energy that an electron at the Fermi level needs to overcome the vacuum level. In a photoemission experiment the free electron is detected by a spectrometer, which in turn has an additional work function as depicted in Fig. 3.6. The detector and the sample are usually set on the same potential, whereby the Fermi levels ($E_F$) of both equalize. Thus, the work function of the sample is actually not measured in the PES experiment, but instead the kinetic energy of the photoelectron relative to vacuum level of the detector (blue arrow). In practice this means that only the work function of the detector needs to be determined and the binding energies of any core level can be deduced from the spectra independent of the sample's work function.

### 3.6.7. Depth sensitivity of photoelectron spectroscopy

On its way to the surface the photoelectron can scatter within the material. This process is quantified by the inelastic mean free path (IMFP), which is defined as the average distance that an electron can travel without any inelastic collisions [43]. The IMFP is dependent on the kinetic energy of the photoelectron as well as on the material properties, but independent of the experimental geometry, i.e. the angle between the detector and the surface normal. It is impotent to note that the IMFP does not consider elastic scattering events. Despite the material dependency of the IMFP, one can identify a similar behaviour of the IMFP for any material in dependence of the kinetic energy of the electrons as obvious from Fig. 3.7. This lead to the concept of the so called "universal curve", which is only energy dependent and allows to roughly estimate the depth sensitivity of a PES experiment.

Originally, the surface sensitivity of XPS experiments was determined by the so called effective attenuation length (EAL), which assumes an exponential decay of the photoelectrons passing through a solid. However, it has been shown that the EAL's measured for the same material, can differ depending on the experimental geometry, which is mainly due to the neglected elastic scattering of the electrons inside the solid. Elastic scattering is the main reason why calculated IMFPs do not match the experimental determined EALs and can also result in a non-exponential decay of the photoelectrons. Thus, EAL and IMFP can only be directly substituted if elastic scattering effects are completely ignored. However, in HAXPES experiments using normal photoelectron emission angles, they are approximately the same.

Correctly, the EAL is defined as a parameter which, when introduced in place of the IMFP into an expression, and assuming that elastic scattering effects are negligible for a given quantitative application, will correct that expression for elastic scattering effects. This definition has the consequence that the EAL may have different values for different quantitative applications. Thus, it is crucial to clearly specify the particular application and the definition of the parameters for that application, e.g. by providing the used equation [43, 44].

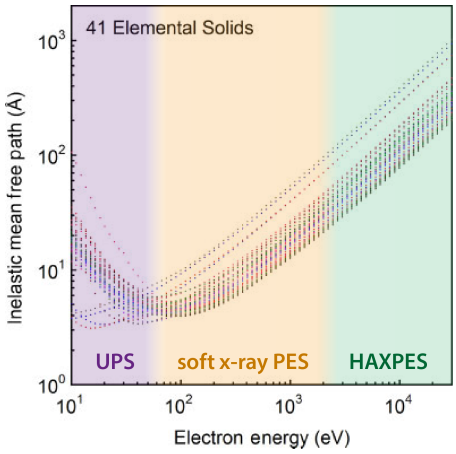


**Figure 3.7:** Comparison of calculated inelastic mean free paths (IMFP) for 41 elemental solids in dependence of electron energy. With increasing kinetic energy of the photoelectrons, the IMFP increase up to several tens of nanometers. Thus, HAXPES offers core level spectroscopy with true bulk sensitivity and allows to probe buried interfaces. (Figure from [48])

To circumvent these uncertainties, the emission from solids is described by the depth distribution function (EDDF) $\phi(z, \cos\alpha)$ [45], which states the probability that a photoelectron leaving the sample surface under an angle $\alpha$ is originating from a certain depth $z$ normal from the surface into the material [43]. The exact EDDF is determined by the electron transport through the solid. This is most frequently treated using Monte Carlo simulations, which however require a large computing effort. Thus, a formalism based on the kinetic Boltzmann equation within the transport approximation has been developed and has proven to be successful in modelling the transport of photoelectrons in solids [46]. A complete description of the formalism can be found in [47]. The electron transport is governed by inelastic and elastic scattering events, which in turn essentially depend on the physical properties of the individual material, like e.g. density and number of valence electrons per formula unit. If elastic electron scattering is neglected, the EDDF simplifies to,

$$\phi(z, \cos\alpha) = W(\psi) \exp\left(-\frac{-z}{\lambda_{\mathrm{IMFP}} \cos\alpha}\right) , \tag{3.10}$$

where $W(\psi)$ is the differential photoelectric cross section, $\psi$ the angle between the direction of the incident X-rays and the direction of photoelectron emission from the surface and $\lambda_{\mathrm{IMFP}}$ the IMFP of photoelectrons in the material.

### 3.6.8. Information Depth

A major experimental advantage of HAXPES is the increased probing depth due to the increased IMFP of the photoelectrons (see Fig. 3.7) compared to soft X-ray PES. Thus, for planning and analysing HAXPES experiments the maximum depth from which useful information can be acquired is of major interest. Therefore, the information depth (ID)

is defined as the probing depth from which a certain percentage $P$ of the photoelectrons originate [43] and can be determined by the emission depth distribution function,

$$\frac{\int_0^{ID(P)} \phi(z, \cos\alpha)\, dz}{\int_0^{\infty} \phi(z, \cos\alpha)\, dz} = \frac{P}{100} \,. \tag{3.11}$$

Commonly used values for $P$ are 90 %, 95 %, or 99 %. In this thesis only ID(95) will be employed. In case elastic scattering is neglected (see Eq. 3.10), the equation can be derived into an analytical expression

$$\mathrm{ID}(P) = -\lambda_{\mathrm{IMFP}} \cos\alpha \, \ln(1 - P/100) \,. \tag{3.12}$$

The influence of elastic scattering on the information depth has been studied in detail by comparing the results from Eq. 3.12 with results gained by using EDDFs obtained from solution of the kinetic Boltzmann equation within the transport approximation by Powell *et al.* [44]. They found that the information depth is smaller than expected from Eq. 3.12 and that the scaling factor $R_{ID}$ is approximately constant for emission angles of $0° \leq \alpha \leq 50°$. In this region the factor can be estimated using the single scattering albedo $\omega$, which describes the strength of elastic scattering, using the following expression:

$$R_{ID} = 1.000 - 0.787\,\omega \qquad \text{where } \omega = \frac{\lambda_{\mathrm{IMFP}}}{\lambda_{\mathrm{IMFP}} + \lambda_{\mathrm{TMFP}}} \tag{3.13}$$

Hereby, $\lambda_{\mathrm{TMFP}}$ is the transport mean free path (TMFP) of the investigated material. Using equation 3.12 and 3.13 it is possible to estimate the information depth for any material and electron energy as long as the emission angle is less than 50° if the the IMFP and TMFP of the material are known. IMFP values can be obtained from databases or calculated by the TPP-2M formula of Tanuma *et al.* [49]. The TMFP can be received from the SESSA database which is included in the software SESSA v1.3 [50]. The software also includes the TPP-2M formula for IMFP determination and thus can be used to determine IMFP and TMFP for any material.

### 3.6.9. Spectral features

A photoemission spectrum usually reveals a variety of features that cannot be explained by excitation of an electron from a core level only. A brief phenomenological description of the effects relevant for the features discussed in this thesis shall be given in the following.

#### Spin-Orbit-Coupling

The excitation of an electron creates a core-hole, which has an spin moment $S = 1/2$ and an orbital angular momentum $L = 0, 1, 2, \ldots$, which is often denoted with the familiar notation $s$, $p$, $d$. These moments are coupled by the spin-orbit interaction, which causes

a splitting of the so far degenerate energy levels of the core hole, to the total angular momentum $\mathbf{J} = \mathbf{L} + \mathbf{S}$. Since the spin of an electron is always $S = 1/2$ the total momentum can only be $J_{\pm} = |L \pm 1/2|$. In consequence, all core-levels levels with $L \neq 0$ (e.g. all core-levels except the s-shells) are split into two distinct levels. The relative intensity of the spin-split peaks can be derived from the ratio of the degeneracy $J(J+1)$ of the two states, as long as there are no other interactions, which are able to mix the spin–orbit split states,

$$\frac{J_+(J_+ + 1)}{J_-(J_- + 1)} = \frac{2(L + 1/2) + 1}{2(L - 1/2) - 1} = \frac{L}{L + 1} \,. \tag{3.14}$$

This results in intensity ratios of 1 : 2 for $p$, 2 : 3 for $d$, 3 : 4 for $f$-shells. Since the spin-orbit interaction is proportional to $1/r^3$, the spin-orbit splitting is most pronounced for deeply bound core levels. Since the core hole is created in XPS as in XAS as well, the splitting due to spin-orbit coupling is likewise observable by both techniques. However, the notation of the resulting spectral lines is not identical.

### Shake-up satellites and peak asymmetries

The photoemission process has a finite probability that the atom, which emits the photoelectron, in the final state is not present in its lowest lying ground state, but rather in an energetically higher lying excited state. Hereby, the kinetic energy of the photoelectron is reduced by the corresponding energy. In metallic materials the Fermi level is crossing the valence band, resulting in high density of unoccupied states above the Fermi level. The transition probability into these final states is gradually decreasing with increasing energy of the final states. As a consequence, an asymmetric tail at the high-binding energy side of the photoemission lines of metals can be observed. In contrast, in insulators an excited state reflects an occupation of a state clearly above the Fermi level. In this case, the effect is reflected in an additional "shake-up" peak at a higher binding energy above the main photoemission line

### Chemical shifts

In solids, part of the valence electrons of an atomic species can be transferred to another atom, depending on the type of bonding between them. In ionic crystals, cations completely give a number of electrons to neighbouring anions, which is quantified by the valency of the corresponding atom species. These missing or extra electron change the electrostatic interaction between the remaining electron shell and the nucleus, because the shielding (screening) of the nucleus by the shell is altered. In particular, in cations where some electrons are missing, the remaining electrons are stronger bound towards the core. This results in characteristic increased binding energies of the core levels, which in turn can be used as a fingerprint for the valency of the investigated cation species.

### Surface core-level shifts

The atoms situated at the surface of a solid have fewer next-nearest neighbours than atoms deep in the bulk. As a consequence these atoms are weaker bound in the lattice, which in turn can result an shift of the core level binding energies. This effect can become strongly pronounced if photon energies are used, which result in a very short IMFP of the photoelectrons and thus a strong surface sensitivity of the photoemission experiment. The latter is especially valid for photon energies from the ultraviolet to the soft X-ray range. In contrast, in HAXPES experiments this effect can often be neglected.

## 3.6.10. Determination of stoichiometry from XPS

XPS spectra can be used to determine the stoichiometry of different atomic species in a sample by comparing the intensity of the corresponding peaks. Also the ratio between different valencies of one ion species can be determined if their chemically shifted peaks can be well resolved. To perform such a quantitative analysis, one needs to isolate the contribution of the peak of interest from adjacent overlapping peaks and from the background, which is usually done by fitting all components of the spectrum. Hereby, all the above discussed line-shift effects need to be considered as possible contributions.

The probability $W_x$ that a photoelectron is excited on species $x$ depends on the the atomic density of the species $n_x$ in the investigated material, as well as of the corresponding photoionization cross section $\sigma_x$.

$$W_x \sim n_x \sigma_x \tag{3.15}$$

However, only photoelectrons that are reaching the spectrometer are contributing to the recorded spectrum. In order to justify this requirement it is common to use the angular distribution of photoelectrons, which can be determined from the differential cross section $d\sigma_{nl}/d\Omega$. The latter depends on the experimental geometry, the photon energy, the element of interest and the investigated core-level. If the incident photons are linearly polarized, as in the case of synchrotron radiation, the angular distribution of the subshell photoionization cross section can be approximated by [51, 52]:

$$\frac{d\sigma_{nl}}{d\Omega} = \frac{\sigma_{nl}(h\nu)}{4\pi}\left[1 + \beta_{nl}(h\nu)\, P_2(\cos\theta)\right] \tag{3.16}$$

$$P_2(\cos\theta) = \frac{1}{2}\left(3\,\cos^2\theta - 1\right)\,. \tag{3.17}$$

For circularly polarized and unpolarized photons, the photoelectron angular distribution may be written as [52, 53]

$$\frac{d\sigma_{nl}}{d\Omega} = \frac{\sigma_{nl}(h\nu)}{4\pi}\left[1 - \frac{\beta_{nl}(h\nu)}{2}\, P_2(\cos\theta)\right]\,. \tag{3.18}$$

In both cases, $\sigma_{nl}$ is the photoionization cross section of a given element for the atomic subshell with quantum numbers $n$ and $l$, which can be found in [54]. $\theta$ is the angle between the incident photon beam and the emitted photoelectron. $\beta$ is the subshell-dependent asymmetry parameter of the photoelectron angular distribution given in Ref. [55]. Alternatively, both parameters can be found in [52, 56] or determined using the software SESSA v1.3 [50]. Based upon this, the peak area $A_{x,nl}$ of species $x$, which is determined from the fit, can be corrected by the respective photoionization cross-sections to determine the corresponding spectral weight $I_{x,nl}$

$$I_{x,nl} = A_{x,nl} \left( \frac{d\sigma_{x,nl}}{d\Omega} \right)^{-1} . \tag{3.19}$$

# CHAPTER 4

# Growth studies of $NiFe_2O_4$ thin films

Before studying the physical properties of $NiFe_2O_4$ films and its interfaces, it is mandatory to establish a process for high quality thin film growth of $NiFe_2O_4$ and to understand the influence of the experimental parameters of the process on the properties of the resulting $NiFe_2O_4$ thin films. Ideally, the films shall maintain quasi bulk-like properties. In particular they should have insulating and ferrimagnetic behaviour, which is a prerequisite to realize magnetic tunnel junctions, that rely on spin-dependent tunnelling of electrons.

The complex crystalline structure of spinels is highly sensitive to structural and chemical disorder and defects, which can strongly alter the properties of the material. A review of the already comprehensive literature on this topic [12–14, 57] shows that growing ferrite thin films is a challenging task and that the process has to be optimized for every growth method and even for every setup individually. Based on a review of literature, we have chosen pulsed laser deposition (PLD) for $NiFe_2O_4$ thin film growth. This chapter will thus examine the influence of the PLD growth parameters on the epitaxial growth of $NiFe_2O_4$ thin films.

In detail, we deposited series of $NiFe_2O_4$ films for varying laser fluence, substrate temperature, and background $O_2$ pressure, respectively. The epitaxial quality and structural properties of the films were evaluated by XRD and their magnetic behaviour was probed by recording hysteresis loops using SQUID magnetometry. As a result, we found a set of growth parameters which yields reproducible high-quality $NiFe_2O_4$ thin films. The deposition of $NiFe_2O_4$ has also proven to be surprisingly robust to minor variations of these parameters. In the following, the given substrate temperatures correspond to the value set at the heater control unit. The laser fluence is calculated from the laser pulse power as described in section 3.1.

It has been shown that the electronic properties in spinels like e.g. $NiFe_2O_4$ [58], $CoFe_2O_4$ [59] or $Zn_xFe_{3-x}O_4$ [60] sensitively depend on the appropriate oxygen partial

| Substrate (Orientation) | Crystal structure | Lattice parameter *a* [nm] | Strain [%] |
|---|---|---|---|
| $SrTiO_3$ (001) | Perovskite | 3,905 | -6,3 |
| MgO (001) | Rock salt | 4,212 | 1,0 |
| $MgAl_2O_4$ (001) | Spinel | 8,083 | -3,1 |
| $NiFe_2O_4$ (001) | Spinel | 8,339 | |

**Table 4.1.:** Structural constants of various substrates and the corresponding lattice mismatch of $NiFe_2O_4$.

pressure during growth. We therefore investigated the influence of oxygen supply on the $NiFe_2O_4$ film properties by varying the oxygen partial pressure during growth under constant total background pressure. Hereby, contrary to our expectations, we found that $NiFe_2O_4$ thin films grow epitaxial over a wide-range of oxygen partial pressures and that only the total lack of oxygen results in a breakdown of stable film growth.

## 4.1. Review of Literature

Several publications on the thin film growth of $NiFe_2O_4$ have been published to date, concerning the growth parameters, substrate selection and the resulting film quality. Different deposition methods were employed and high quality growth of epitaxial films has been accomplished with many of them. Hereby, sputtering [12, 14, 61, 62] as well as pulsed laser deposition (PLD) [12, 57, 63] emerged as the methods of choice for the growth of $NiFe_2O_4$ films with thicknesses in the nanometer regime. Thicker films (> 1 µm) can be fabricated by direct liquid injection chemical vapour deposition [64]. Recently, also oxygen-assisted molecular beam epitaxy (MBE) turned up to provide high quality ferrite thin film growth, i.e. in the case of $CoFe_2O_4$ [65, 66] or $MnFe_2O_4$ [67].

Remarkably, the choice of the deposition method is of minor importance compared to the choice of an appropriate substrate material, since the substrate strongly affects the structure and properties of the films. A selection of substrates, that have been often used as templates for $NiFe_2O_4$ thin films is presented in table 4.1. MgO substrates with a (001) surface are chosen, since they have a rock salt structure with a lattice constant closely matching the half-unit-cell value of $NiFe_2O_4$. However, at growth temperatures of 600 °C, Mg ions have been observed to diffuse into the film by subgrain boundary diffusion [12]. This can be avoided by inserting an (001) oriented Pt buffer layer [61]. On top of this buffer $NiFe_2O_4$ grows in a two-dimensional Frank–van der Merwe mode in (111) orientation. Unfortunately, the films does not grow as a single crystal but instead in four families of crystallites that are rotated by 90° with respect to each other.

To improve this towards single crystalline film growth, substrates which are featuring

a spinel crystal structure were chosen, since they allow isostructural[1] growth of $NiFe_2O_4$. Hereby, $MgAl_2O_4$ is a common choice due to its commercial availability as a substrate material. Due to the lattice mismatch, $MgAl_2O_4$ induces a biaxial compressive in-plane strain of −3.1 %. $NiFe_2O_4$ grows textured and single crystalline on $MgAl_2O_4$ and the films shows an enhanced out-of-plane $a_{OOP}$ lattice parameter up to thicknesses of several tens of nm [14, 68]. With increasing film thickness, $a_{OOP}$ eases towards the bulk value, reflecting the relaxation of the lattice. However, $NiFe_2O_4$ on $MgAl_2O_4$ is also suffering from diffusion of Mg and Al cations into the film.

$SrTiO_3$ has also been investigated as a candidate for a substrate material. Surprisingly, despite the large lattice mismatch between $SrTiO_3$ (001) and $NiFe_2O_4$ (001) of −6.3 % it turned out that $NiFe_2O_4$ films grown on STO (001) substrates consistently have the same [001] in-plane texture as the substrate and grow cube-on-cube without any parasitic phases [12, 13, 57]. In contrast to films on $MgAl_2O_4$, they are already fully relaxed at film thicknesses of less than 10 nm [14], what is likely connected to the larger mismatch of $NiFe_2O_4$ on $SrTiO_3$.

One concern using approximately half unit-cell sized substrate is the occurrence of so-called antiphase boundaries (APB). The latter are generated due to island forming at different positions on the substrate, which are shifted by half of a unit cell to each other and thus loose periodicity upon merging [69, 70]. Antiphase boundaries are attributed to cause the inferior magnetic properties of $NiFe_2O_4$ thin films, which are caused by an antiferromagnetic coupling across the boundaries and result in a reduced saturation magnetization of the films. Since it is very hard to overcome this strong exchange coupling, very high magnetic fields are required to drive the films into saturation. The APB density in $NiFe_2O_4$ films deposited on different substrates has been compared and, as expected, films on MgO and $SrTiO_3$ show a large amount APB domains [63]. Yet, also films grown on spinel substrate exhibit a APBs, although with much lower densities as the films grown on half unit-cell sized substrate. Hereby, their density is correlated to the lattice mismatch and their occurence is thus explained by the more prominent relaxation in the more strained films.

Based on the above findings, we have chosen $SrTiO_3$ as a substrate for all samples discussed in this work. There are also some further advantages to mention: First, $SrTiO_3$ can be easily doped with Nb, which adds conductive behaviour to the otherwise insulating material. For example, this is mandatory for all spectroscopic studies, which involve the emission of photoelectrons by light. Otherwise, the created core holes could not be replenished and the investigated sample would start charging, which in turn hampers the spectroscopic experiments. Another important aspect of doping is that the conductivity of $SrTiO_3$ can be increased to a level, for which $SrTiO_3$ can be employed as a bottom electrode for a spin-filter tunnel junction. Successful spin-injection using MgO tunnel barriers into Nb-doped $SrTiO_3$ substrates has already been demonstrated [71]. Thus, the

[1] Isostructural growth is given when subtrate and film exhibit the same lattice structure (e.g. spinel on spinel).

fabrication of all-oxide heterostructures as efficient spin filter tunnel contacts may be envisioned.

## 4.2. Optimization of deposition parameters for $NiFe_2O_4$ thin film growth

In the following, we will discuss the studies performed to optimize the growth of $NiFe_2O_4$ on $SrTiO_3$ in our PLD setup[2]. The investigations in this thesis build on the findings from the master thesis by S. Kramer-Sinzinger [72]. Hereby, two major results concerning the effect of growth parameters on the resulting film quality can be emphasized. First, the effect of the post-annealing was discussed. During a post-annealing step, the grown film is kept at an elevated temperature, which is supposed to improve the micro-structural quality of the film due to diffusion of the ions to their equilibrium positions. A series of samples annealed at a temperature of 750 °C with varying post-annealing time revealed that with increasing annealing time the saturation magnetization as well as the coercive field of the films develops closer towards bulk values. This, together with the result of less broadened rocking curves of the $NiFe_2O_4$ (004) diffraction peak, was interpreted as a restoration of the crystal structure towards a bulk-like structure.

Second, a series of $NiFe_2O_4$ grown with varying substrate temperatures $T_{sub}$ was investigated. Hereby, it was revealed that temperatures above $T_{sub} = 800$ °C lead to a rapid decrease of the crystal quality as well as to increased surface roughness. On this footing, growth conditions of $T_{sub} = 720$ °C, $p_{ox} = 0.05$ mbar and $J = 1.5\,J/cm^2$ were chosen as a starting point for the further optimization study. The samples grown for the study include one series of $NiFe_2O_4$ films grown under varying laser fluence between $J = 1.3 - 1.8\,J/cm^2$, one with different substrate temperatures between $T_{sub} = 550 - 750$ °C and one with varying oxygen background pressure between $p_{ox} = 0.005 - 0.150$ mbar. After deposition all samples were post-annealed for 90 min in the given atmosphere and at the substrate temperature already applied given growth. Since the used PLD setup has no option for in situ thickness monitoring, the thickness of all samples was determined by ex situ XRR.

## 4.3. Influence of oxygen background pressure on $NiFe_2O_4$ thin film growth

The stoichiometry and structural properties of a thin film deposited by PLD are considerably influenced by the complex interaction of ablated ions in the plasma plume. The kinetics of the plume can be tuned by adjusting the particular oxygen background gas pressure in the PLD chamber [73, 74]. Thus, the influence of the background pressure

[2] We thank R. Dittmann for providing us the PLD setup at the Forschungszentrum Jülich.

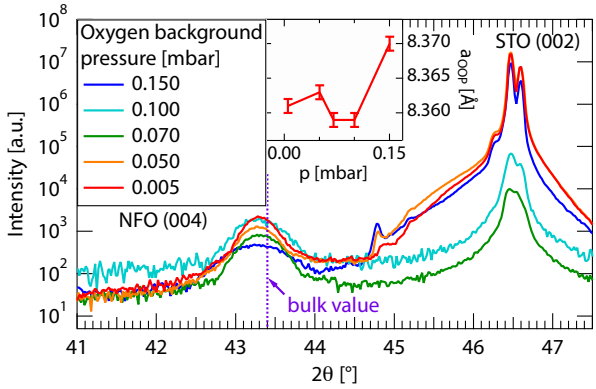


**Figure 4.1:** XRD scans of the $NiFe_2O_4$ (004) reflection from $NiFe_2O_4$ thin films grown under varying oxygen background pressure. All films show an enhanced out-of-plane lattice constant $a_{OOP}$.

during growth on the structural and magnetic properties of $NiFe_2O_4$ thin films is investigated. A series of $NiFe_2O_4$ thin films is grown under a 100 % oxygen atmosphere for which the total oxygen background pressure was varied between $p_{ox}$ = 0.005 – 0.15 mbar. The other growth parameters were kept at $T_{sub}$ = 720 °C, $J$ = 1.5 J/cm$^2$, a laser pulse rate of 2 Hz and a deposition time of 1500 s.

The film thickness gradually decreased from 25.2 nm to 11.8 nm with increasing background pressure. The structural properties of all films are evaluated from X-ray diffraction scans. $\theta$-2$\theta$-scans ranging from 2$\theta$ = 20° to 100° with a scattering vector parallel to the surface normal were used to analyse the crystal structure of the films and to confirm their epitaxial growth. All samples show the expected substrate peaks and the $NiFe_2O_4$ (004)

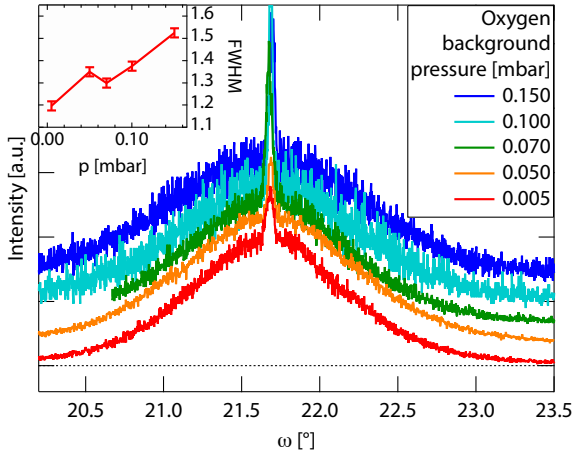


**Figure 4.2:** Rocking curves of the $NiFe_2O_4$ (004) reflection from $NiFe_2O_4$ thin films grown under varying oxygen background pressure $p_{ox}$. The small peak on top of the broad curves can be attributed to the rocking curve of the STO(002) substrate reflection. The inset presents the dependence of the rocking curve broadness, which is a measure of the defect density and mosaicity, on the background pressure.

and (008) reflection at $2\theta \approx 43°$ and $2\theta \approx 95°$ respectively. These reflections are expected for an $NiFe_2O_4$ film growing in [001] direction. No additional peaks are resolved, thus proving that the film growth is epitaxial without any impurity phases. The out-of-plane lattice constant shows no significant dependence on the background pressure and ranges between $a_{OOP}$ = 8.359 Å and 8.370 Å for the series of films (see Fig. 4.1). This is slightly above the bulk value of 8.339 Å and can be attributed to the lattice mismatch of −6.3 % between the $SrTiO_3$ substrate and the $NiFe_2O_4$ film. The latter applies a significant amount of compressive strain to the films. Thus, the films are expected to exhibit a considerable defect density and mosaicity. To investigate the impact of the background pressure onto the amount of created defects, we have performed rocking curve scans of the $NiFe_2O_4$ (004) reflection, which are shown in Fig. 4.2. The width of a rocking curve is directly related to the structural quality of a single crystal. In a perfect crystal, the curve would be a delta function, while defects in the crystal lattice interrupt the long range order and thus increase the width of the rocking curve. As expected, the rocking curves of all $NiFe_2O_4$ films are broadened and show FWHM values between 1.2-1.5°. The broadness is substantially larger than reported for films grown on $MgAl_2O_4$ (FWHM = 0.3°) [14], reflecting the higher distortion of the film due to the increased lattice mismatch. Still, the value is consistent with other reports from $NiFe_2O_4$ grown on $SrTiO_3$ [12, 61]. One clearly identifies a significant increase of the FWHM with increasing background pressure. This reflects an increased defect density and indicates that the films grown at higher oxygen background pressures prefer to relax through incorporation of dislocations or stacking faults.

In a next step, the surface properties of the $NiFe_2O_4$ films are investigated. For the integration of $NiFe_2O_4$ in heterostructures, an atomic sharp interface between the magnetic insulating film and an adjacent electrode would be beneficial, since it diminishes effects due to varying film thickness or intermixing of the two materials. Thus, optimization of the surface properties is of major interest. The surface of all films is scanned by atomic force microscopy right after deposition. The results of the scans are depicted in Fig. 4.3. All samples have in common, that their surface resembles the terrace structure of the underlying $SrTiO_3$ substrate (reference AFM scan of a prepared substrate is shown in App. A), which indicates a 2D growth mode of the $NiFe_2O_4$ films [57]. The roughness of the film surfaces is determined using the root mean square $\sigma_{RMS}$. The films grown with

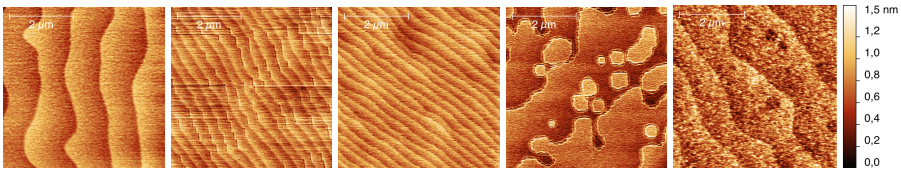


**(a)** 0.005 mbar **(b)** 0.05 mbar **(c)** 0.07 mbar **(d)** 0.10 mbar **(e)** 0.15 mbar

**Figure 4.3.:** AFM images of $NiFe_2O_4$ thin film grown under varying oxygen background pressure.

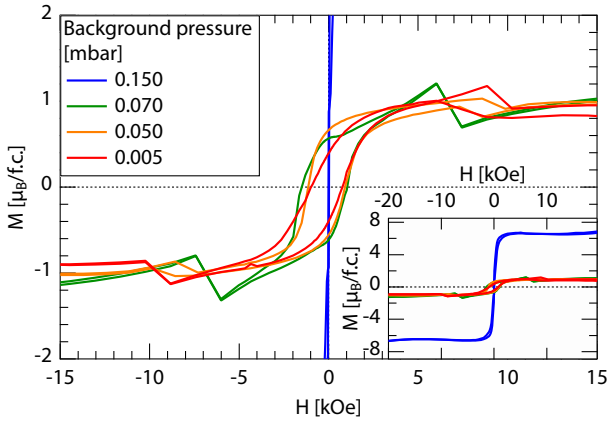


**Figure 4.4:** Detail of the SQUID hysteresis loops recorded from $NiFe_2O_4$ thin films grown under varying background oxygen pressure $p_{ox}$. The inset shows the hysteresis loops in full scaling.

background pressures ≤ 0.07 mbar show very smooth surfaces with $\sigma_{RMS}$ = 0.15 nm. The values are just slightly above the corresponding substrate roughness, and are dominated by the height differences at the step edges. If the background pressure is increased further, the roughness increases up to $\sigma_{RMS}$ = 0.24 nm, which is also clearly visible from the increased granularity in the AFM scan at $p_{ox}$ = 0.15 mbar. This also proves the decreased quality of the thin films grown at higher background pressures, consistent with the results from the rocking curve scans.

The magnetic properties of the samples are investigated by recording SQUID hysteresis loops with applied magnetic fields between $H$ = ±20 kOe parallel to the [001] direction at a temperature of $T$ = 5 K. The diamagnetic contribution of the substrate was removed as described in Sec. 3.4.1 and the remaining signal was normalized to the film volume. Details of the hysteresis loops after background correction are depicted in Fig. 4.4. All samples grown at background pressures below 0.07 mbar clearly show an open hysteresis loop, reflecting their ferrimagnetic nature. The saturation magnetization $M_S$ increases from 0.9 $\mu_B$/f.u. for $p_{ox}$ = 0.005 mbar to 1.2 $\mu_B$/f.u. for $p_{ox}$ = 0.07 mbar. Yet, $M_S$ is lower than the bulk value of 2 $\mu_B$/f.u. [11]. These deviations are supposed to be related to structural dislocations, which form due to the strain incorporated by the substrate, and to the formation of antiphase boundaries (APB) during growth [69]. Thus, the increase in $M_S$ suggests a reduction of the APB or dislocation density due to the increased background pressure. This is supported by the slope of the hysteresis at the coercive field which is also increasing with pressure. A lower APB density reduces the amount of frustrated spins in the film, which in turn is easier to saturate. However, the rocking curve scans suggest an increased defect density with rising background pressure, which leads to the conclusion that only the dislocation density is increasing while the APB density is improving. More surprising is the hysteresis loop of the film grown at $p_{ox}$ = 0.150 mbar, which shows no coercive field any more, but a dramatically increased $M_S$ of 6.8 $\mu_B$/f.u..

The increased background pressure reduces the mean free path of the ablated cations, due to scattering with the background gas as well as other cations and thus changes the energy distribution of the particles travelling towards the substrate. This implies that at a lower background pressure the kinetic energy of the particles is dominated by the energy transfer from the laser and that high energetic particles could impair the structure of the film upon impact. This in turn, results in an enhanced lattice defect density in the film explaining the inferior magnetic properties. At higher background pressure, the particles scatter repeatedly with the background gas. Thus, they are already in thermal equilibrium when they reach the substrate, which in turn results in an improved film quality.

An even higher pressure, as has been used for the film grown at $p_{ox} = 0.150$ mbar, might result in an increase of particle-particle collision in the plasma plume, which causes the formation of atomic chains or clusters in the gas phase. The latter could endure as nano particles in the film, which is supported by the high granularity of the film surface as visible in Fig. 4.7a. These particles could be small enough to reveal superparamagnetic behaviour, which could explain the missing coercive field as can be seen in Fig. 4.4. Superparamagnetism can occur, when the system is small enough, so that the thermal energy can overcome the magnetic anisotropy energy. This leads to random fluctuations of the thermally activated spins [75, 76]. The XRD results still reveal an epitaxial film, implying that the particles align in a lattice structure in the film. However, the enhanced out-of-plane lattice constant of $a_{OOP} = 8.370$ Å together with the enhanced rocking curve width suggest a high dislocation, which could surround the nano particles and which thus reside in the film as nanoscopic magnetic domains.

Another possible explanation is the occurrence of super-paramagnetism due to APBs, which has been observed in $CoFe_2O_4$ [77] and $Fe_3O_4$ [78]. Hereby, the antiferromagnetic coupling across the APBs leads to frustration. The superexchange barriers effectively cancel each other out, enabling the magnetic domains between the APBs to fluctuate much more freely. Thus, the single crystalline film becomes superparamagnetic [78]. However, this is conflicting with our result from the films grown at lower pressures, There, an increase of the background pressure resulted in an improvement of the magnetic properties, due to decreasing defect density.

Based on the results, a background pressure of $p_{ox} = 0.050$ mbar has been chosen for deposition of $NiFe_2O_4$ thin films in the following. At this pressure, epitaxial films with very smooth surfaces are obtained. They show well defined ferromagnetic behaviour and are still far away from the point were they turn into a superparamagnetic state.

## 4.4. Dependence on laser fluence *J*

Next, we investigated the influence of the laser fluence $J$ used in the PLD process on the structural and magnetic properties of the $NiFe_2O_4$ thin films. PLD is a widespread established method for the growth of thin film from complex oxide, since it is assumed to properly transfer the stoichiometry of the used target into the film. However, in

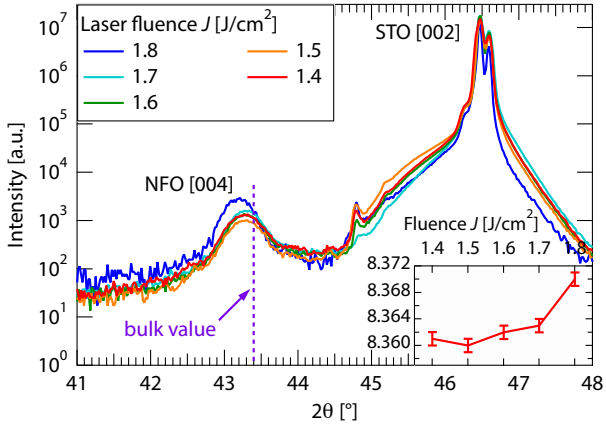


**Figure 4.5:** XRD scans of the $NiFe_2O_4$ (004) reflection from $NiFe_2O_4$ thin films grown under varying laser fluence $J$. All films show an enhanced out-of-plane lattice constant $a_{OOP}$.

case of $SrTiO_3$ thin film growth for example, it has been shown that the stoichiometry considerably depends on the used laser pulse energy. This observation could be explained by two phenomena: First, the ablation of cation species from the target does not necessarily need to be stoichiometric, e.g. XPS analyses of the ablation spots of $SrTiO_3$ targets reveal an increasing Sr/Ti ratio with increasing laser fluence [79]. Second, the scattering of the cation species in the plasma plume depends on the weight of the species. Thus, the ratio of cations reaching the substrate can be influenced by the laser energy [79, 80]. Since the atomic masses of Fe (55.9 u) and Ni (58.7 u) are similar, the latter effect should be of minor importance in the case of $NiFe_2O_4$ thin film growth. Still, the former argument cannot be neglected, since no study concerning the laser ablation of $NiFe_2O_4$ targets has been published so far.

A series of $NiFe_2O_4$ thin films is grown under varying laser fluence between pressure between $J = 1.5 - 1.8\,J/cm^2$. The other growth parameters were kept at $T_{sub} = 720\,°C$ and $p_{ox} = 0.05\,mbar$. It is worth mentioning, that the laser fluence is controlled by a servo loop that is keeping the average laser pulse power on a constant level. Still the emitted power, and thus laser fluence, can deviate slightly from pulse to pulse.

Again, all samples only show the $NiFe_2O_4$ (004) and (008) reflections in $2\theta - \omega$-scans, proving that the films grow epitaxial, independent of the laser fluence. Fig. 4.5 depicts the details of a diffractogram around the $NiFe_2O_4$ (004) reflection. For all films, the peak is shifted towards lower diffraction angles, reflecting an enhanced out-of-plane lattice constant. For laser fluences $J < 1.7\,J/cm^2$ no change in the out-of-plane lattice constant can be observed and all films show an constant of $a_{OOP} = 8.363 \pm 0.003$ Å. In contrast, $a_{OOP}$ is increased for the film grown at higher laser pulse energies $J = 1.8\,J/cm^2$ to $a_{OOP} = 8.374 \pm 0.003$ Å, reflecting a higher distorted unit cell. Rocking curve scans of the $NiFe_2O_4$ (004) reflection, which are shown in Fig. 4.6, reveal an FWHM of $\approx 1.3°$ which is spread by $\pm 0.5°$ (inset Fig. 4.6). There is no recognizable dependence to the laser

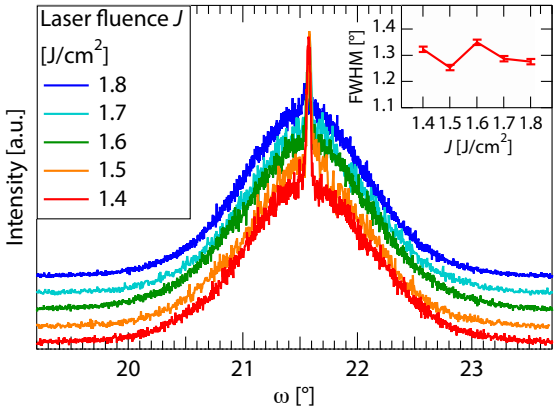


**Figure 4.6:** Rocking curves of the $NiFe_2O_4$ (004) reflection from $NiFe_2O_4$ thin films grown under varying laser fluence $J$. The small peak on top can be attributed to the rocking curve of the STO(002) substrate reflection.

fluence and thus we can conclude that the laser fluence has no sizeable impact on the defect density in the investigated fluence range.

AFM scans of the surfaces from all samples of this series are depicted in Fig. 4.7. All films reproduce the terrace structure of the $SrTiO_3$ substrate at their surfaces, reflecting two-dimensional growth. The rough mean square (RMS) over the whole series is very low between $\sigma_{RMS} \approx 0.14 - 0.17$ nm reflecting a very smooth surface. A closer look at the facets between the terrace edges reveals a grainy surface texture, which is improving when tuning the laser fluence towards lower energies. Furthermore, the terrace edges show some artefacts for all samples except the one grown at $J = 1.5\,J/cm^2$. The origin of these is yet not understood. One possible explanation could be the presence of a not completely $TiO_2$ terminated $SrTiO_3$ surface. In this case the part of the spinel growing on SrO facets would be shifted by a quarter unit-cell in comparison the rest of the film. This in turn would result in dislocations which could carry forward to the surface. However, this is in contradiction to the surface scans of the substrates, which do not show any SrO facets. Still, one can imagine SrO facets at the terrace edge, that are smaller than the lateral resolution of the AFM scans, but are magnified by the dislocations at the film surface.

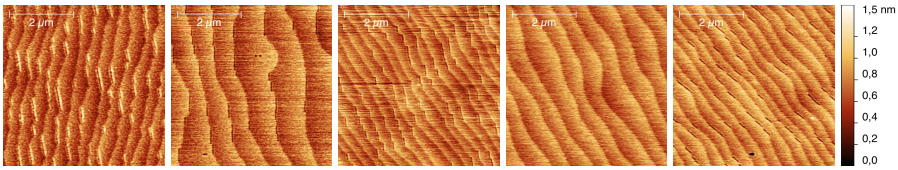


**(a)** $J = 1.8\,J/cm^2$ **(b)** $J = 1.7\,J/cm^2$ **(c)** $J = 1.6\,J/cm^2$ **(d)** $J = 1.5\,J/cm^2$ **(e)** $J = 1.4\,J/cm^2$

**Figure 4.7.:** AFM images of $NiFe_2O_4$ thin film grown under varying laser fluence $J$

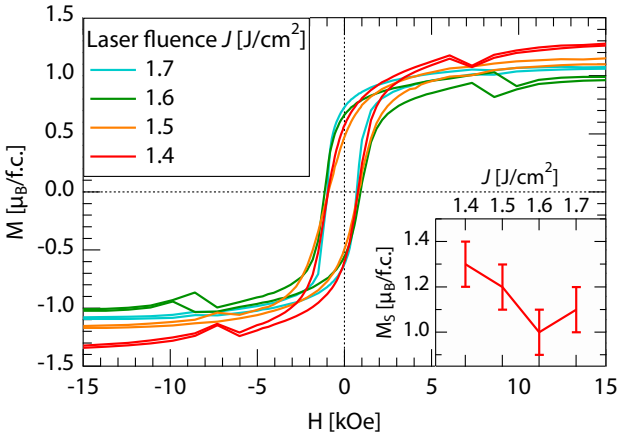


**Figure 4.8:** Details of the SQUID hysteresis loops recorded from $NiFe_2O_4$ thin films grown under varying laser fluence $J$. The inset shows the dependence of the saturation magnetization $M_S$ on the laser fluence.

Finally, the magnetic properties of the samples are investigated by recording SQUID hysteresis loops with applied magnetic fields from $H = \pm 20\,\text{kOe}$ at a temperature of $T = 5\,\text{K}$. Details of the background corrected, normalized $M(H)$ loops are shown in Fig. 4.8. The coercive fields are only varying slightly between the samples and thus no dependence on the laser fluence can be resolved. The inset Fig. 4.8 shows the dependence of the saturation magnetization $M_S$ on the laser fluence. $M_S$ is varying between $M_S \approx 1.0 - 1.3\,\mu_B/\text{f.u.}$, and shows a slight improvement with decreasing laser fluence. For all samples the determined value is again lower than the bulk value of $2\,\mu_B/\text{f.u.}$, as already discussed in Sec. 4.3.

In summary, $NiFe_2O_4$ thin films have been grown under varying laser fluence by pulsed laser deposition. We have found that the laser fluence in the investigated range has no major impact on the structural and magnetic properties of the film. The films grown using lower laser fluences ($J < 1.7\,\text{J/cm}^2$) show an out-of-plane lattice constant closer to the bulk value, reflecting a less distorted film. Also the surface granularity improved slightly with reduced fluence, while no clear trend is detectable for the magnetic properties. The results demonstrate that $NiFe_2O_4$ thin films deposited using PLD grow stable over the investigated range of laser fluences. On this basis, a laser fluency of $1.5\,\text{J/cm}^2$, in the middle of the investigated range, has been chosen for further thin film deposition of $NiFe_2O_4$. At this fluency also the initially mentioned deviations in the laser pulse power should not disturb the thin film growth.

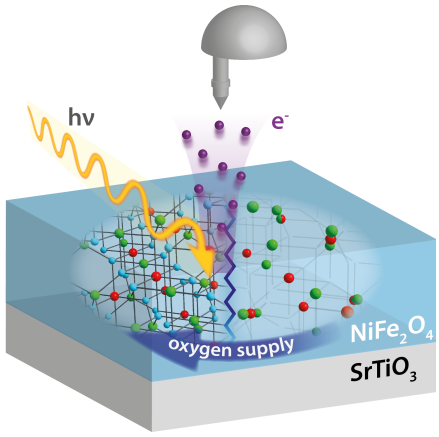


**Figure 4.9.:** Schematics of the experiment: $NiFe_2O_4$ thin films deposited on $SrTiO_3$ (001) in varying $O_2$:Ar atmosphere during PLD growth and probed by hard X-ray photoemission spectroscopy (HAXPES).

## 4.5. Stability of the $NiFe_2O_4$ thin films under varying oxygen partial pressure

The results of this section are published in M. Hoppe, M. Gorgoi, C. M. Schneider, and M. Müller, "*Wide-Range Structural and Chemical Stability of the Magnetic Oxide $NiFe_2O_4$ Grown by $O_2$-Assisted Pulsed Laser Deposition*", IEEE Transactions on Magnetics **50**, 2506204, (2014).

So far, we have worked out a suitable set of parameters for high quality growth of $NiFe_2O_4$ thin films. Though, only pure oxygen has been used as a background gas during deposition as described in section 4.3. It has been shown, that the properties of spinel thin films can be substantially altered by modifying the oxygen partial pressure. For example, the electronic properties in $NiFe_2O_4$ [58], $CoFe_2O_4$ [59] or $Zn_xFe_{3-x}O_4$ [60] sensitively depend on the appropriate oxygen partial pressure during growth. Varying the oxygen partial pressure while keeping the total backpressure constant can be archived by providing an oxygen-argon mixture and tuning the ratio between them. Thus, one can tune the reactivity of particles in the plasma plume, without modifying the kinetics. Here, we investigate in detail the influence of the partial oxygen supply during growth by PLD on the structural and electronic properties of $NiFe_2O_4$ thin films, as schematically depicted in Fig. 4.9.

$NiFe_2O_4$ thin films have been deposited on conductive 0.1 % Nb-doped $SrTiO_3$(001) substrates in a mixed oxygen/argon ($O_2$:Ar) atmosphere. Thereby, the $O_2$ partial pressure was stepwise increased from 0 % to 100 % in intervals of 25 %. During growth, the

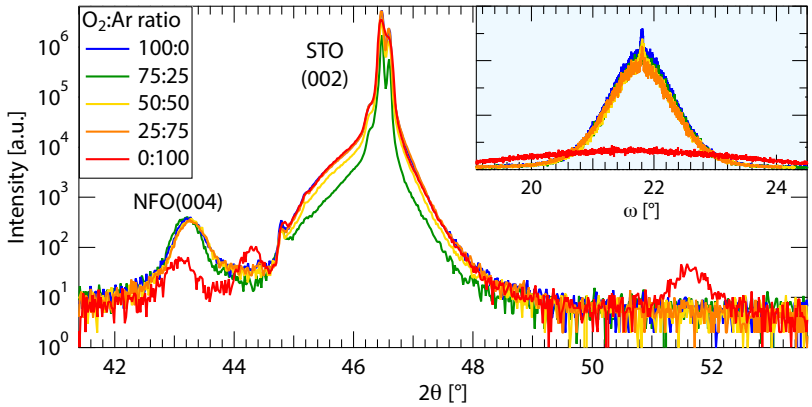


**Figure 4.10.:** $\theta$-$2\theta$-scans of the $NiFe_2O_4$ (004) and $SrTiO_3$ (002) reflections of $NiFe_2O_4/SrTiO_3$ (001) samples grown in varying $O_2$:Ar atmosphere. Single-crystalline growth without parasitic phases is observed for the $NiFe_2O_4$ films with nonzero oxygen supply, whereas the sample grown in a pure Ar atmosphere displays additional, nonepitaxial features. Inset: Rocking curve $\omega$-scans of the $NiFe_2O_4$ (004) reflection.

substrate was held at 720 °C, while the laser parameters were set to a fluence of 1.8 J/cm$^2$ and a repetition rate of 2 Hz. The background gas pressure was kept at p = $4 \times 10^{-2}$ mbar, with the $O_2$:Ar ratio controlled by the amount of introduced $O_2$ gas. After deposition, the samples were postannealed for 90 min under similar conditions. The film thickness was determined by X-ray reflectivity (XRR) measurements yielding values of $d$ = 23-26 nm for the oxygen-assisted grown films. The thickness of the film grown in pure Ar atmosphere was not determinable due to its large surface roughness, which suppresses the occurence of Kiesing-fringes in XRR data. Hard X-ray photoelectron spectroscopy (HAXPES) experiments were conducted at the HIKE endstation of the KMC-1 beamline at BESSY II (HZB Berlin) [82]. All HAXPES spectra were taken at room temperature and at a photon energy of 4 keV. The X-ray beam was aligned at 3° grazing incidence and the detector collected the photoelectrons with the emission direction normal to the sample surface. The given experimental parameters result in an ID(95) ≈ 17 nm (see Sec. 3.6.8).

### 4.5.1. Structual Properties

First, we investigate the structural properties of the $NiFe_2O_4$ sample series for different $O_2$:Ar ratios during PLD deposition by wide angle $\theta - 2\theta$-scans. For all samples with nonzero $O_2$ supply, the $\theta$-$2\theta$-scans recorded from 10° to 90° reveal pronounced $NiFe_2O_4$ (004) and (008) diffraction peaks, with no additional peaks observable. This result indicates, that the $NiFe_2O_4$ thin films grow epitaxially and without any parasitic phases on $SrTiO_3$ (001). In Fig. 4.10, we show the $\theta$-$2\theta$ spectra around the $NiFe_2O_4$ (004) and $SrTiO_3$ (002)

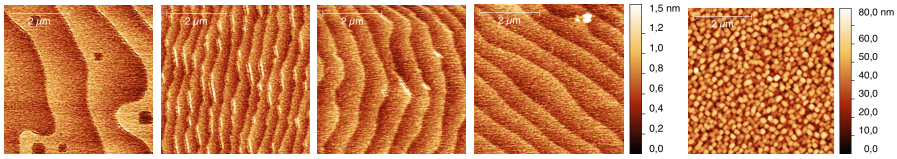


**(a)** 100:0 **(b)** 75:25 **(c)** 50:50 **(d)** 25:75 **(e)** 0:100 $O_2$:Ar-ratio

**Figure 4.11.:** AFM pictures of $NiFe_2O_4/SrTiO_3$ (001) samples grown in varying oxygen backpressure atmosphere. (a)-(d) Scans of films grown in non-zero oxygen atmosphere clearly depict a terraced surface with step heights of around 4 Å. (e) $NiFe_2O_4$ film grown in pure Ar atmosphere, which exhibits a granular surface morphology.

reflections. From the angular position of the $NiFe_2O_4$ (004) reflections, we determined an out-of-plane lattice constant of $d_{NFO} = 8.37 \pm 0.01$ Å for all samples with nonzero $O_2$ backpressure. This value is slightly larger than the bulk reference of 8.339 Å and can be assigned to the compressive biaxial lattice strain of −6 % induced by the $SrTiO_3$ (001) substrate. Rocking curve scans of the $NiFe_2O_4$ (004) reflection (inset in Fig. 4.10) show a full width half maximum (FWHM) of 1.28 ± 0.03°, caused by atomic dislocations and mosaicity. The small feature located on top of the $NiFe_2O_4$ (004) rocking curves originates from the $SrTiO_3$ (002) substrate peak.

The structural properties of the $NiFe_2O_4$ sample grown in a pure Ar atmosphere, however, are strongly deviating. First, the position of the $2\theta = 43.05°$ reflection translates into an increased out-of-plane lattice constant of 8.40 Å. Furthermore, the XRD spectrum displays two extra diffraction peaks at $2\theta = 44.27°$ and $2\theta = 51.58°$, which are not in agreement with the previously observed epitaxial growth mode and can rather be associated with parasitic or polycrystalline phases. Taking into account the photoemission data which will be discussed below, these two peaks can be assigned to the (111) and (200) reflection of metallic Ni, while the $2\theta = 43.05°$ reflection can be attributed to the (004) reflection of $Fe_3O_4$. The rocking curve FWHM is also strongly enhanced to ≈ 4.4°, indicating large structural disorder.

### 4.5.2. Suface Morphology

Next, we investigate the surface morphology of the samples by AFM, with representative results depicted in Fig. 4.11. All $NiFe_2O_4/SrTiO_3$ (001) samples deposited in a nonzero oxygen backpressure possess a very smooth surface with a root mean square (RMS) roughness of $\sigma_{RMS} \approx 0.13$ - 0.15 nm only. The $NiFe_2O_4$ surface morphology thereby nicely mirrors the characteristic terrace structure of etched $SrTiO_3$ (001) substrates, which evidently is a prerequisite for a 2-D growth mode of the $NiFe_2O_4$ films. In contrast, $NiFe_2O_4$ films grown in a pure Ar atmosphere show a granular structure and a significantly enhanced roughness of $\sigma_{RMS} \approx 12$ nm. This result is consistent with the breakdown of epitaxial growth, as observed by XRD measurements in Fig. 4.10. We thus conclude,

that epitaxial growth of $NiFe_2O_4$ thin films on $SrTiO_3$ (001) is observed only for nonzero oxygen partial pressure during PLD deposition.

### 4.5.3. Chemical Stability

In a further step, we clarify whether the $NiFe_2O_4$ chemical properties, i.e. cation stoichiometry and valencies, depend on the $O_2$:Ar pressure ratio. For this purpose, we conducted HAXPES experiments in order to quantitatively analyse the chemistry of the $NiFe_2O_4/SrTiO_3$ sample series. HAXPES – the high-energy counterpart of conventional soft X-ray PES – offers a large information depth (ID), which allows one to probe the chemical properties of a layered film structure with true bulk sensitivity [83]. In Fig. 4.12(a) and (b), the Fe 2p and Ni 2p core level spectra for $NiFe_2O_4$ thin films grown with varying $O_2$:Ar ratio are shown. As a reference dataset, we also recorded core-level spectra of the bulk $NiFe_2O_4$ target material.

For all samples grown in non-zero partial $O_2$ atmosphere, the Fe $2p_{3/2}$ and $2p_{1/2}$ core levels (Fig. 4.12(a)) are located at binding energies of 710.9 eV and 724.5 eV, in very good agreement with the bulk $NiFe_2O_4$ reference values of 711.0 eV and 724.5 eV, respectively, and consistent with literature [84]. Centered between the spin-orbit split Fe 2p doublet, we observe a satellite peak both in the thin film and the bulk samples. The shape and binding energy position of this Fe satellite serve as a fingerprint for the chemical state of different iron oxides and particular lattice site occupancies [85]. In bulk $NiFe_2O_4$, trivalent Fe cations are equally distributed across the tetrahedral and octahedral spinel lattice sites.

A complete inversion to the normal spinel structure would shift the satellite spectral weight to lower binding energies by about 0.8 eV as indicated by line A in Fig. 4.12(a). Since both shape and energy position of the thin film samples satellite peaks perfectly match that of the $NiFe_2O_4$ bulk spectrum, we conclude that the Fe cations occupy the bulk lattice sites, and find no hint for a cationic inversion from the inverse to the normal spinel within the resolution limit of the HAXPES experiment.

For the $NiFe_2O_4$ sample grown in pure Ar atmosphere, the Fe $2p_{3/2}$ peak in Fig. 4.12 (a) shows two shoulders B and C emerging around 709 eV and 707 eV, respectively. Feature B can be attributed to the presence of divalent iron cations, whereas feature C, which is e.g. also observed in $Fe_3O_4$ samples [86], can be explained by the formation of underoxidized iron cations, caused by the occurrence of defects in neighboring lattice sites during sample preparation. The Fe $2p_{1/2}$ core level is shifted to smaller binding energy 723.3 eV, which matches very well with results for $Fe_3O_4$ thin films [87] and thus indicates, that the Fe cations are not completely oxidized to $Fe^{3+}$. This mixed valence state of $Fe^{3+}$ and $Fe^{2+}$ cations is also reflected by the Fe $2p_{3/2}$ satellite, in which the divalent and trivalent Fe contributions superimpose each other in a way that leads to a characteristic structureless satellite feature.

We move on to the analysis of the Ni 2p core levels. For all $NiFe_2O_4$ thin films grown in nonzero $O_2$ backpressure, the Ni $2p_{3/2}$ and Ni $2p_{1/2}$ doublet in Fig. 4.12 (b) is located at a

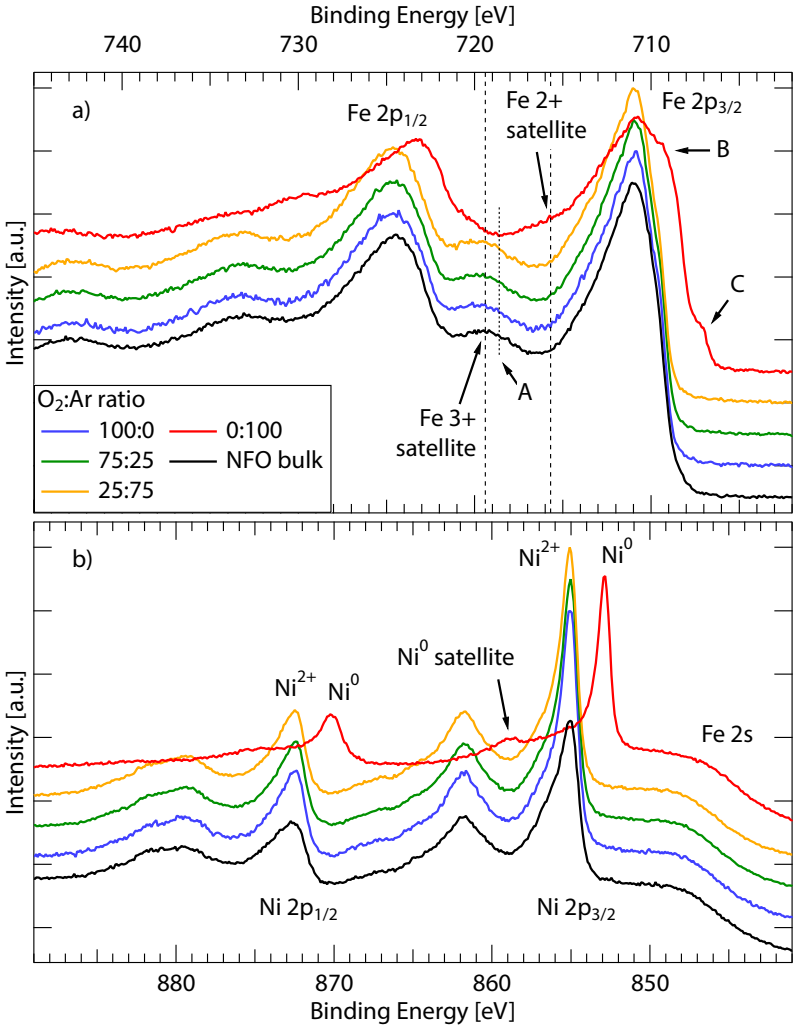


**Figure 4.12.:** HAXPES spectra of (a) Fe 2p and (b) Ni 2p core levels recorded at a photon energy of 4 keV from $NiFe_2O_4$ films grown under a varying oxygen argon atmosphere.

binding energy of 855.1 eV and 872.4 eV, respectively, with a $Ni^{2+}$ satellite peak observable at $E_B$ = 861.8 eV. The $NiFe_2O_4$ thin film spectra thereby perfectly matches the reference $NiFe_2O_4$ bulk spectrum, which nicely confirms, that the Ni cations are present in its fully oxidized 2+ valency. In contrast, the Ni 2p spectrum of the $NiFe_2O_4$ film grown in pure Ar atmosphere indicates the presence of metallic contributions. In Fig. 4.12 (b), the Ni $2p_{3/2}$ and $2p_{1/2}$ doublet is shifted towards lower binding energies of 852.9 eV eV and 870.2 eV, respectively, and the characteristic $Ni^0$ satellite shifted by 6 eV from the Ni $2p_{3/2}$ main peak is clearly resolved (Ref. [88, 89]). The Ni 2p spectrum does not show any hint for an intermediate state of underoxidized Ni, but contributions of metallic Ni only.

From these results we conclude, that if a 100 % Ar backpressure is provided during $NiFe_2O_4$ deposition, all available oxygen atoms are attracted by the Fe cations. Moreover, the energetically more favorable formation of Fe oxide leads to a chemical reduction of Ni to its metallic state. In consequence, the data reveals that due to the lack of oxygen no stoichiometric $NiFe_2O_4$ is formed. Instead, two chemical distinct phases develop, namely a $Fe_3O_4$ phase intermixing with metallic Ni clusters. This model is also supported by the structural results, for which we can assign the additional Bragg reflections in the XRD spectrum at $2\theta = 44.27°$ and $2\theta = 51.58°$ in Fig. 4.10 to the (111) and (200) reflection of metallic Ni, respectively.

### 4.5.4. Stoichiometry

Finally, the $NiFe_2O_4$ stoichiometry is determined by a quantitative analysis of the Fe 3p and Ni 3p core level peaks (Fig. 4.13). Their spectral weights are determined after subtraction of a Shirley-type background and correction by the respective photoionization cross-sections as described in Sec. 3.6.10. The resulting Fe:Ni cation ratio is given in the inset of Fig. 4.13.

We find the $NiFe_2O_4$ films grown in nonzero $O_2$ partial pressure nicely reproducing the bulk reference value within an uncertainty of ±3 %. In contrast, the $NiFe_2O_4$ sample deposited in pure Ar atmosphere reveals a significant off-stoichiometry, i.e. an ≈ 17 % enhanced Fe:Ni ratio. Moreover, the spectrum features an additional peak between the Fe 3p and Ni 3p core levels, that can be attributed to Ti 3s originating from the substrate. The appearance of the Ti 3s substrate peak is caused by the highly granular surface morphology of the film, as has been previously observed by AFM in Fig. 4.11.

From the stoichiometry analysis we conclude, that $NiFe_2O_4$ thin films deposited in a partial $O_2$ backpressure form with correct Fe:Ni stoichiometry. Obviously, the kinetics of the PLD growth mode reveals itself to be very robust with regard to the $O_2$:Ar ratio offered.

In summary, we studied the structural and chemical properties of PLD-deposited $NiFe_2O_4$ thin films on conductive Nb-doped $SrTiO_3(001)$ substrates, with special regard to the influence on the $O_2$:Ar ratio. By varying the $O_2$ partial pressure from 0 % to 100 %, we find that providing supplementary oxygen is necessary to realize heteroepitaxial growth and to obtain a stoichiometric Fe:Ni cation distribution. Although a stoichiometric

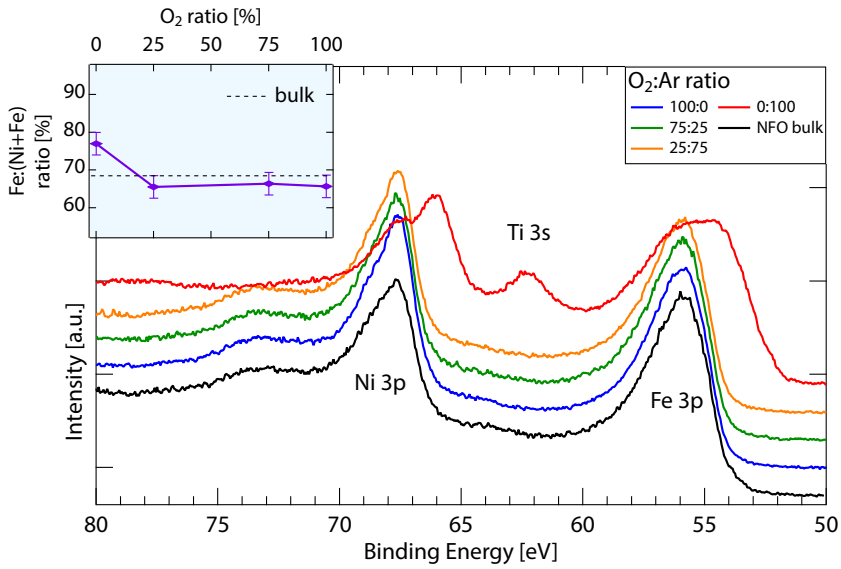


**Figure 4.13.:** HAXPES spectra of the Fe 3p and Ni 3p core levels recorded at a photon energy of 4 keV from $NiFe_2O_4$ films grown under a varying oxygen argon atmosphere. Inset: Stoichiometry of the films determined from the Fe 3p and Ni 3p spectral weights.

$NiFe_2O_4$ target material is utilized, $NiFe_2O_4$ samples deposited without an additional $O_2$ backpressure turn out to be of polycrystalline structure, while the chemical quality degrades to a coexistence of mixed-valent Fe oxide and metallic Ni phases.

In that, our study clearly demonstrates that $NiFe_2O_4$ thin films grow structurally and chemically stable over a wide range of oxygen partial pressure by PLD technique. Hence, these high quality epitaxial and insulating $NiFe_2O_4/SrTiO_3$ heterostructures are promising candidates for integration into spin filter tunnel contacts for room temperature application.

## 4.6. Conclusion

In summary, in this chapter the influence of the parameters from the PLD process on the growth conditions were evaluated in detail. We found, that the oxygen background pressure during growth can considerably alter the film quality, due to the changing kinetics of the particles in the plasma plume. We also proved, that the presence of oxygen in the background atmosphere is mandatory for the formation of $NiFe_2O_4$. Yet, the amount of supplied oxygen can be tuned over a wide range. In contrast, the laser pulse energy turned out to have only a minor impact onto the structural and magnetic

properties of the $NiFe_2O_4$ thin films. From the results, we worked out a set of parameters, which reproducibly allows to grow $NiFe_2O_4$ thin films epitaxial and cube-on-cube on $SrTiO_3$ substrate. In detail, for the optimized growth process for $NiFe_2O_4$ thin films $TiO_2$-terminated $SrTiO_3$ substrates are used, which are kept at a temperature of $T = 700\,°C$ during deposition. For the PLD process, a laser fluence of $J = 1.5\,J/cm^2$, a pulse repetition rate of 2 Hz and an oxygen background pressure of $p = 4 \times 10^{-2}$ mbar are chosen. After deposition, the grown films are postannealed for 90 min in vacuum and cooled down subsequently.

So far, only $NiFe_2O_4$ films with thicknesses above 10 nm have been fabricated, where effects due to reduced dimensionality can be neglected. In a next step, the film thickness is gradually reduced down to a few nanometer, which allows to probe the properties of the $SrTiO_3/NiFe_2O_4$ interface using surface-sensitive spectroscopic techniques. In this pursuit, any thickness dependence of the physical properties of the thin films is of interest, i.e. if $NiFe_2O_4$ remains insulating and ferrimagnetic in the ultrathin film limit.

# CHAPTER 5

## Cationic inversion in $NiFe_2O_4$ ultrathin films?

The results presented in this chapter are published in M. Hoppe, S. Döring, M. Gorgoi, S. Cramm, and M. Müller, "*Enhanced ferrimagnetism in auxetic $NiFe_2O_4$ in the crossover to the ultrathin-film limit*", Physical Review B **91**, 054418 (2015).

In this chapter, the structural, electronic and magnetic properties of single-crystalline $NiFe_2O_4$ thin films with varying thickness are investigated. Special attention is paid on the impact of reduced dimensionality in the crossover from bulk-like to ultrathin films. In particular, we evaluate if the films still reveal quasi bulk-like properties in this ultrathin film limit. Hereby, all $NiFe_2O_4$ films are found to be insulating and ferrimagnetic, independent of their film thickness. Furthermore, we observed an enhanced saturation magnetization $M_S$ for ultrathin $NiFe_2O_4$ films ($d$ = 2 nm) on Nb-$SrTiO_3$ (001) substrates that co-occurs with a reduced out-of-plane lattice constant under compressive in-plane epitaxial strain. We found a bulk-like cationic coordination of the inverse spinel lattice independent of the $NiFe_2O_4$ film thickness – thus ruling out a cationic inversion that nominally could account for an enhanced $M_S$.

In previous studies of $NiFe_2O_4$ [12, 13] and $CoFe_2O_4$ [21] thin films an unexpected magnetic behaviour, i.e. an enhanced saturation magnetization was reported for these films in the ultrathin film limit. The origin of this phenomenon was explained by a cationic inversion from an inverse to a partly normal spinel lattice ($0 < \lambda < 1$), since this structural redistribution of Fe cations nominally accounts for an increased magnetic moment. A structural inversion from the inverse to the normal spinel lattice consequently alters the cationic coordination, as quantified by the inversion parameter $\lambda$. Hereby, $\lambda$ is the fraction of $A^{2+}$-cations occupying $O_h$ sites, with $\lambda = 0$ denoting a normal ($Ni^{2+}[Fe^{3+}Fe^{3+}]O_4$) and $\lambda = 1$ an inverse ($Fe^{3+}[Ni^{2+}Fe^{3+}]O_4$) spinel lattice. A more detailed description of the spinel structure is given in section 2.6. Theoretical considerations based on density func-

tional theory calculations (DFT) find a partial cationic inversion energetically favourable for $NiFe_2O_4$ films under tensile, but not under compressive strain [91], as is the case for $NiFe_2O_4$ grown on Nb-$SrTiO_3$ (001). The origin of the altered magnetic exchange interaction in ultrathin $NiFe_2O_4$ films thus still remains an open question.

Here, we explore the details of the electronic and magnetic properties of single-crystalline $NiFe_2O_4$ films in the crossover from bulk-like to the ultrathin film limit. The goal of our studies is to uncover modifications of the structural, electronic and magnetic properties with regard to the reduced film dimensionality. We performed a complementing spectroscopic analysis employing the bulk- and surface sensitive photon spectroscopy techniques HAXPES, XANES and XMCD, respectively, which allow for a precise quantification of the element-specific cationic valencies and spatial coordinations. From our thorough analysis, we can conclude on the absence of a cationic inversion for all $NiFe_2O_4$ film thicknesses. Instead, we find an auxetic behaviour of ultrathin $NiFe_2O_4$ films, i.e. a reduction of the unit cell volume, which may correlate to the finding of an enhanced $M_S$.

## 5.1. Experimental details

A series of $NiFe_2O_4$ thin films with varying thicknesses between 2 and 20 nm has been deposited from stoichiometric targets on conductive 0.1 % Nb-doped $SrTiO_3$ (001) substrates by utilization of the pulsed laser deposition technique. The substrates were previously etched in buffered hydrofluoric acid to provide a $TiO_2$-terminated terrace surface [92]. During growth, the laser fluence was set to 1.5 J/cm$^2$ and a repetition rate of 2 Hz. The oxygen pressure was kept at 0.04 mbar and the substrate was heated to $T_S$ = 635 °C. After deposition, the samples were post-annealed at $T_S$ for 90 min in vacuum.

The thickness of the grown films was determined by X-ray reflectivity measurements (XRR), while the structural characterization was accomplished by X-ray diffraction experiments (XRD). Both XRR and XRD experiments were performed on a Philips XPert MRD using Cu-$K\alpha$-radiation. Bulk magnetic properties of the samples were investigated on a Quantum Design MPMS SQUID. Hysteresis loops were recorded at $T$ = 5 K with a magnetic field up to 3.6 T, which was applied parallel to the in-plane [100]-axis of the films.

Hard X-ray photoelectron spectroscopy (HAXPES) was conducted on the HIKE endstation of the KMC-1 beamline at the BESSY-II electron storage ring (HZB Berlin) [82]. In contrast to soft X-ray photoelectron spectroscopy, HAXPES experiments use high energy X-rays with photon energies $E_P$ ranging from 2 to 15 keV. Thus, the kinetic energy as well as the inelastic mean free path of the emitted photoelectrons are strongly enhanced, which gives HAXPES an information depth (ID) of several tens of nanometers, allowing one to probe the chemical properties of a multi-layered film structure with true bulk sensitivity [83]. All spectra shown in this work were taken at $E_P$ = 4 keV and at room temperature. The X-ray beam was aligned at 3° grazing incidence and the photoelectron detector normal to the sample surface. By defining ID(95) as the probing depth

from which 95 % of the photoelectrons originate, as described in section 3.6.8, the given experimental parameters result in an ID(95) ≈ 17 nm.

X-ray absorption near edge structure (XANES) experiments have been performed at the HIKE endstation as well. To record the XANES spectra, the X-ray absorption of the samples was determined by the emitted fluorescence (FY), which was detected by an energy dispersive detector. In contrast, the absorption of the $NiFe_2O_4$ bulk target material was determined in total electron yield mode (TEY). All signals were normalized to the incident X-ray flux, monitored by a ionization chamber in front of the sample. The incident beam was polarized parallel to the plane of incidence and we found no dependence of the angle between the incident X-ray beam and the sample surface on the resulting normalized spectrum. Thus, the angle was optimized for every spectrum, in order to maximize the fluorescence signal without saturating the detector.

For all photon energies used during the HAXPES and XANES experiments, photoemission spectra of the Au $4f$ core level from an Au reference sample attached to the manipulator have been recorded. The energy position of the Au $4f$ lines was compared to standard values and all measured data corrected accordingly.

X-ray magnetic circular dichroism (XMCD) data was determined by X-ray absorption spectroscopy (XAS) experiments performed at the UE56-1 SGM beamline at BESSY-II. The sample surfaces were aligned in 20° grazing incidence. A magnetic field of 300 mT was applied parallel to the surface and in the plane spanned by the incident beam with the surface normal axis. The absorption signal was taken in TEY mode and was normalized to the incident X-ray flux. The XMCD asymmetry spectra were determined from the difference of two spectra collected by changing either the magnetic field to the opposite direction, or by two spectra recorded by changing the polarization from left to right-handed. In total, at least four absorption spectra were taken for every sample, each with a different combination of polarization and magnetization direction.

For XMCD data analysis, we have calculated model XMCD spectra using the program CTM4XAS 5.5 which is briefly described in appendix B. Using the parameters from Ref. [93], the interatomic screening is taken into account by reducing the Slater integrals F(dd), F(pd), and G(pd) with scaling factors F(dd) = 0.7, F(pd) = 0.8 and G(pd) = 0.8. For octahedral (tetrahedral) symmetry, the crystal field was set to 10 Dq = 1.2 eV (−0.6 eV) and the exchange field was set to M = 10 meV (−10 meV). The resulting spectra were broadened by a Lorentzian width with a half-width of 0.3 eV (0.5 eV) for the $L_3$ ($L_2$) edge to respect the core-hole lifetime broadening, and by a Gaussian width of 0.2 eV to account for instrumental broadening.

## 5.2. Results

### 5.2.1. Structural and magnetic characterization

First, the thickness-dependent structural properties of ultrathin $NiFe_2O_4$ films on Nb-$SrTiO_3$ (001) were investigated by X-ray diffraction experiments. $\theta$-$2\theta$-scans ranging from $2\theta$ = 20° to 100° with a scattering vector parallel to the surface normal were used to

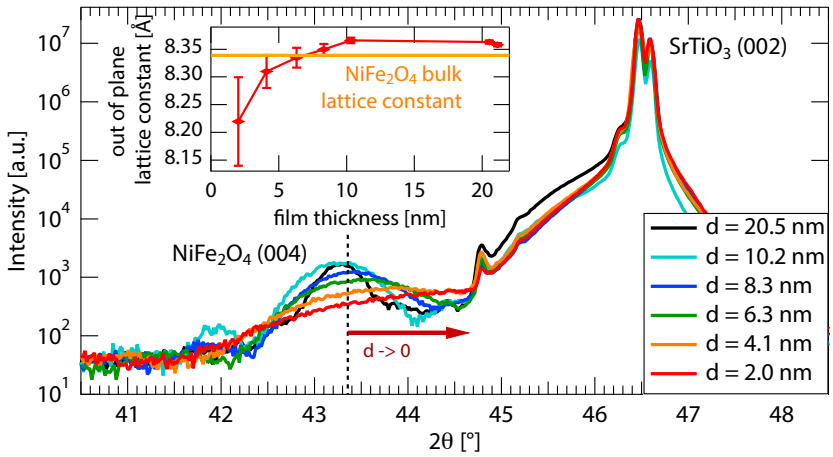


**Figure 5.1.:** $\theta$-$2\theta$-scans of the $NiFe_2O_4$ (004) reflection for varying film thickness. The out-of-plane lattice constant $a_{oop}$ decreases below the bulk value for ultrathin films (see inset).

analyze the crystal structure of the films and to confirm their epitaxial growth. All scans show the expected reflections of a (001)-oriented $SrTiO_3$ crystal, as well as two additional reflections at $2\theta \approx 43°$ and $2\theta \approx 95°$, which can be attributed to the $NiFe_2O_4$ (004) and (008) reflections. Since no other reflections are observed, we conclude that the $NiFe_2O_4$ films grow textured along the (001) direction without any parasitic phases. $\Phi$-scans around the $SrTiO_3$ (202) and $NiFe_2O_4$ (404) peaks both show a four-fold symmetry and provide evidence that the films grow cube-on-cube on the $SrTiO_3$ substrate, despite the induced biaxial compressive strain of 6.4 %. In Figure 5.1, the details of the $\theta$-$2\theta$-scans around the $NiFe_2O_4$ (004) reflection are shown, which reveal that for decreasing film thickness the center of the $NiFe_2O_4$ (004)-peak shifts towards larger angles, implying a decreasing out-of-plane lattice constant $a_{oop}$. The broadening of the peaks for thinner films is due to the smaller amount of material that contributes to coherent diffraction. For film thicknesses above 6 nm, $a_{oop}$ is slightly larger than the bulk value ($a_{bulk}$ = 8.339 Å). In combination with the compressive in-plane stress induced by the substrate, this finding reveals the tendency of the material to preserve its bulk unit cell volume. On the other hand, for lower thicknesses $a_{oop}$ decreases, as compiled in the inset of Fig. 5.1. This refers to a reduction of the unit cell volume for ultrathin films in comparison to the bulk value, a result that also has been reported for $CoFe_2O_4$ films on $SrTiO_3$ [94]. In contrast to $CoFe_2O_4$, however, $a_{oop}$ of $NiFe_2O_4$ even drops below its bulk value for ultrathin films, which implies that $NiFe_2O_4$ shows an auxetic behaviour, i.e. a negative Poisson ratio $\nu$ in the crossover to the monolayer regime.

Next, the $NiFe_2O_4$ films were investigated with regard to their magnetic properties. Hereby, special attention is payed to changes dependent on their film thickness. Hysteresis

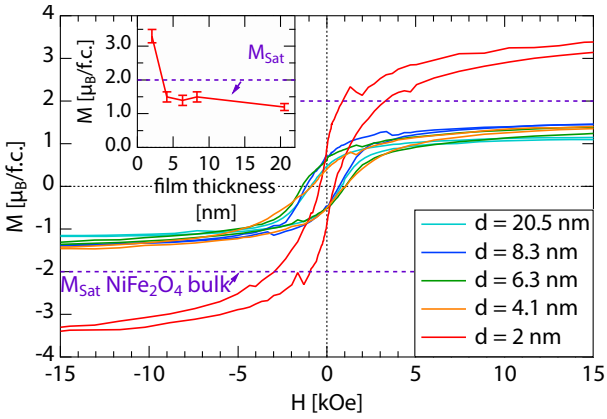


**Figure 5.2:** In-plane $M$-$H$ hysteresis loops of $NiFe_2O_4$ on $SrTiO_3$ (001) recorded at $T = 5\,K$. The inset shows the saturation magnetization $M_S$ as a function of $NiFe_2O_4$ film thickness.

loops of all samples were recorded at $T = 5\,K$, which are dominated by the diamagnetic contribution of the $SrTiO_3$ substrate. To extract the magnetic response of the $NiFe_2O_4$ films, a subtraction of the diamagnetic background is required. Therefore, linear slopes have been fitted to the high-field tails of the raw signal and subtracted afterwards.

In Figure 5.2, hysteresis loops after background correction are depicted, which confirm ferromagnetic behaviour for all $NiFe_2O_4$ film thicknesses. The coercive fields are approximately constant for thicknesses above $d = 6\,nm$, but dramatically decrease for $d = 2\,nm$. For $CoFe_2O_4$ on MgO, this effect has been interpreted as a result of the reduction of the magnetic anisotropy for thin films [77]. $NiFe_2O_4$ films with thicknesses above 6 nm show a saturation magnetization of $M_S \approx 1.3 - 1.5\,\mu_B/f.u.$, which is lower than the bulk value of $2\,\mu_B/f.u.$ [11]. These deviations are supposed to be related to structural dislocations, which form due to the strain incorporated by the substrate, and to the formation of anti-phase boundaries during growth. The latter occur due to island forming at different positions on the substrate, which are shifted by half of a unit cell to each other and thus loose periodicity upon merging [69]. This model is supported by the high external magnetic fields required to drive the films into saturation, which is even at 15 kOe not completely accomplished. More striking, when the film thickness scales below 6 nm, we find the saturation magnetization enhancing up to $3\,\mu_B/f.u.$ - thus significantly exceeding the bulk value. This result is in agreement with previous studies on $NiFe_2O_4/SrTiO_3$ [13] and $CoFe_2O_4/SrTiO_3$ [21]. So far, this phenomenon was explained in terms of a cationic inversion, where the inverse spinel structure of the bulk state partly changes to a normal spinel structure in the crossover to the ultrathin film limit. An experimental proof for this model is however still lacking.

Moreover, for the thinner films, the contributions from contaminations to the total signal increase. Foerster *et al.* [68] discussed the influence of the substrate, for which in the case of $NiFe_2O_4$ films on $MgAl_2O_4$, the observed increased magnetization can be explained by a paramagnetic contribution from the substrate, which even disappears, if

the magnetic response of the substrate is subtracted properly. Similar observations have been made in $Fe_3O_4$, where initially an enhanced magnetization has been attributed to non-compensated cations at the interfaces [95]. But again, the effect was later explained by Fe impurities in the used MgO substrates [96]. Yet, this cannot explain the findings for $NiFe_2O_4$ on $SrTiO_3$, since $SrTiO_3$ shows a purely diamagnetic response and thus validates the applied background subtraction.

In order to evidence the existence or absence of a cationic inversion, we investigate the chemical properties and cationic distribution of $NiFe_2O_4$ as a function of the film thickness in more detail.

### 5.2.2. HAXPES

In a first step, we need to clarify whether the chemical properties of $NiFe_2O_4$ differ for bulk-like and ultrathin films. HAXPES measurements have been performed to quantify the valence states of each cation species. In contrast to soft X-ray photoemission, HAXPES allows us to identify these properties not only at the surface but with bulk sensitivity. The increased information depth even allows us to record reference spectra of the pressed $NiFe_2O_4$ powder used as bulk-target for PLD deposition, which do not posses a flat surface as typically required for low-energy photoemission experiments.

Figure 5.3 plots the Ni $2p$ and Fe $2p$ core level spectra for $NiFe_2O_4$ films of 8 nm to 2 nm, and compares them to the bulk reference. In Figure 5.3(a), all spectra of the Ni $2p$ core level display the Ni $2p_{3/2}$ and Ni $2p_{1/2}$ peaks at a binding energy of 855.1 eV and 872.4 eV respectively, without a chemical shift relative to the bulk material. The two main peaks are both accompanied by satellite peaks at 7 eV above their binding energies and overlap with the Fe 2s core level at lower energies. The shape of all spectra is comparable to that of a single monolayer of NiO [97], in particular there is no shoulder visible at the high energy side of Ni $2p_{3/2}$. The occurrence of such a shoulder ~1.5 eV above the $2p_{3/2}$ peak (see NiO bulk reference in Fig. 5.3(a) for comparison) has been theoretically described by a screening effect, that emerges from electrons not originating from the oxygen orbitals around the excited Ni cation, but from adjacent $NiO_6$ clusters [98]. The HAXPES experiment thus confirms, that no NiO clusters have formed within the $NiFe_2O_4$ films. Moreover, the spectra do not show any contribution of metallic $Ni^0$, which would peak at around 852.8 eV. We therefore conclude, that the $NiFe_2O_4$ films contain completely oxidized and homogeneously distributed $Ni^{2+}$ cations only without any NiO cluster formation.

Figure 5.3(b) depicts the HAXPES data of the Fe $2p$ core levels from all $NiFe_2O_4$ samples with $d = 8 - 2$ nm. For comparison, also model spectra of Fe cations in the inverse spinel structure of magnetite ($Fe_3O_4$) are given (reproduced from Ref. [85]). These spectra have been calculated individually for the different possible Fe cation lattice site occupancies ($O_h$, $T_d$) and valencies (2+, 3+). The Fe $2p_{3/2}$ and $2p_{1/2}$ core levels are peaking at binding energies of 710.9 eV and 724.4 eV, in agreement with the spectrum of the $NiFe_2O_4$ bulk reference and consistent with literature [84]. The formation of under-oxidized $Fe^{2+}$ ions

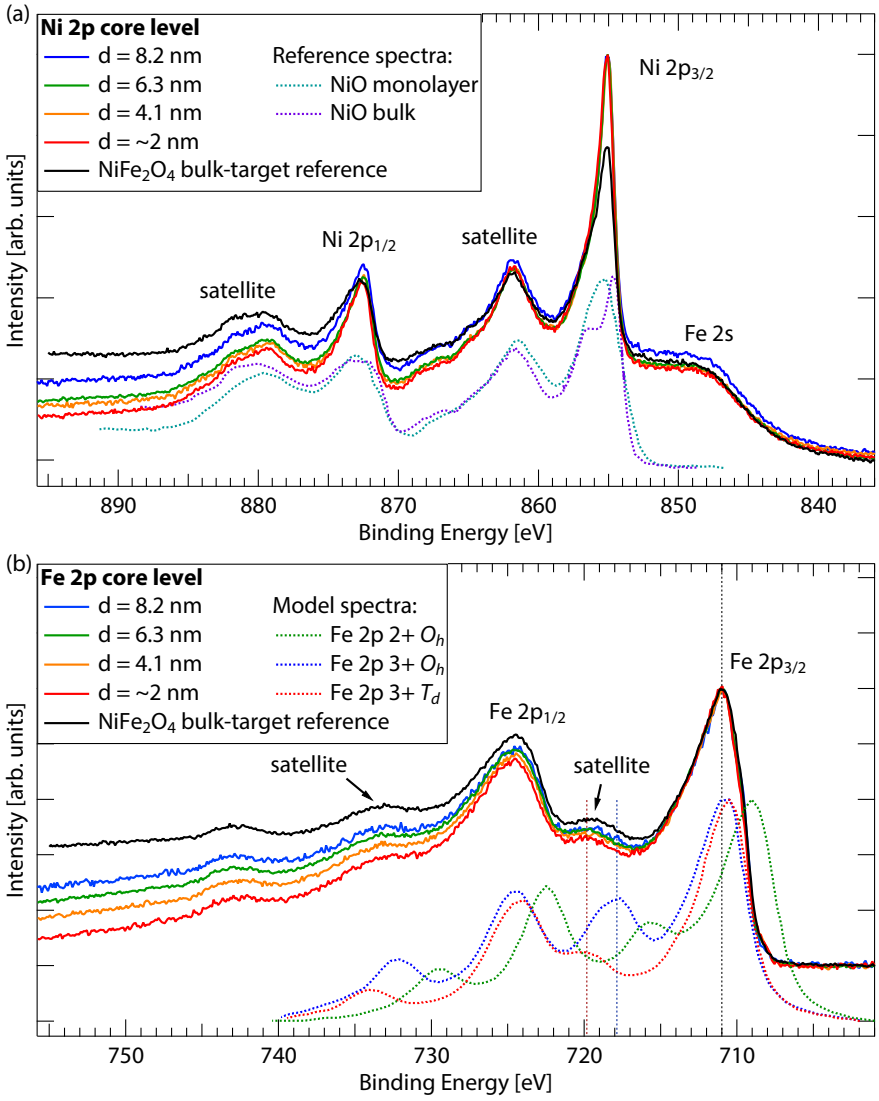


**Figure 5.3.:** HAXPES spectra of $NiFe_2O_4$ films with varying film thickness recorded at a photon energy of $h\nu$ = 4 keV. (a) Ni 2*p* core level spectra and references for one monolayer NiO and NiO bulk [97]. (b) Fe 2*p* core level spectra in comparison to model spectra taken from [85].

during film growth would result in a characteristic shoulder at the low-energy side of the Fe $2p_{3/2}$ peak, due to a chemical energy shift (as observable in the $Fe^{2+}$ $O_h$ reference). All measured spectra coincide with the bulk reference sample, thus confirming that the $NiFe_2O_4$ films consist of fully oxidized $Fe^{3+}$ cations and that the amount of underoxidized $Fe^{2+}$ cations is below the detection limit.

Comparing the $Fe^{2+}$ $O_h$, $Fe^{3+}$ $O_h$ and $Fe^{3+}$ $T_d$ model spectra reveals, that the main peak binding energies are sensitive to the oxidation state, but not to the atomic site occupancy. In contrast, the Fe $2p_{3/2}$ satellite observable between the spin-orbit split Fe $2p$ peaks is caused by a screening effect of the surrounding oxygen ions and deviates significantly for $T_d$ and $O_h$ cation coordination. Thus, its shape and binding energy position can serve as a fingerprint for the chemical state of different iron oxides and the cationic lattice site occupancies [85]. A complete inversion to the normal spinel structure would shift the satellite's spectral weight to lower binding energies by about 0.8 eV. Since both shape and energy position of the thin film samples satellite peaks perfectly match that of the $NiFe_2O_4$ bulk spectrum, we conclude, that the $Fe^{3+}$ cations occupy the bulk lattice sites – without any sign for a cationic inversion from the inverse to the normal spinel structure in the binding energy resolution limit of the performed HAXPES experiment.

In summary, both the Ni $2p$ and Fe $2p$ spectra are comparable to the spectrum of bulk material for all film thicknesses, and reveal that the chemical composition of the bulk material is well reproduced in the ultrathin $NiFe_2O_4$ films. The Fe $2p_{3/2}$ satellite gives no hint for a cationic inversion in ultrathin $NiFe_2O_4$. In order to rule out also any smaller effect, we investigate the spatial cationic distribution by further spectroscopic means.

### 5.2.3. XANES

To gain precise information on the spatial cationic distribution in the $NiFe_2O_4$ thin films, we recorded XANES spectra of the Fe and Ni $K$ edge. Since the fine structure above the absorption edge is dominated by multiple scattering with the surrounding atoms of the investigated cation species, XANES is very sensitive to the distribution of the oxygen anions around the cation. Thus, a cationic inversion - for which the local site occupancy changes from tetrahedral to octahedral, or vice versa - considerably modifies the shape of the spectral fine structure.

The absorption spectra of the $NiFe_2O_4$ film samples are recorded by fluorescence yield, thus the measured data probes the bulk-like film properties. Figure 5.4(b) shows the XANES spectra of the Fe $K$ edge for $NiFe_2O_4$ films down to 2 nm and a bulk material reference spectrum. All spectra show a pre-edge feature at 7111 eV, which in case of the spinel structure is observable for cations in a $T_d$ symmetry only. While the main absorption line is caused by a dipole transition from the 1s to the empty 4p orbital, the pre-edge structures in transition metal oxides are assigned to quadrupole transitions to the empty 3d states, and thus are only very weak [100]. If the inversion symmetry of the transition metal cation is broken, the local 3d and 4p wavefunctions of the cation hybridize, and in turn dipole transitions into this orbital become allowed, leading to an

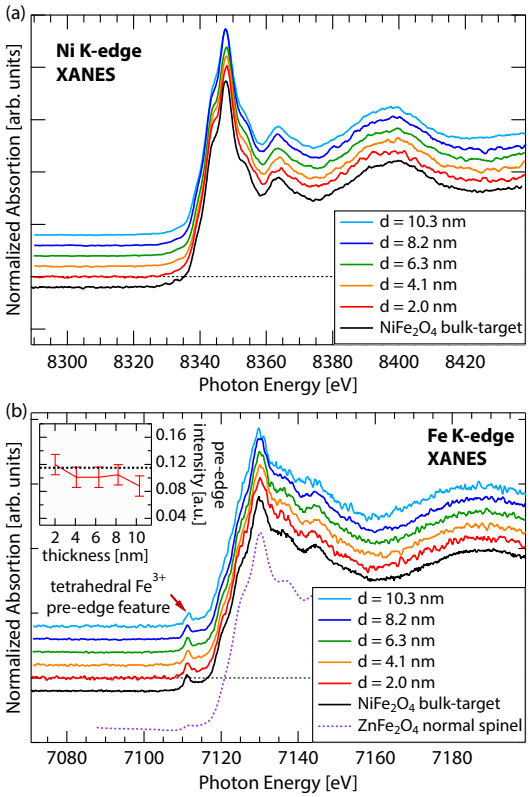


**Figure 5.4:** XANES spectra of (a) the the Ni *K* edge and (b) the Fe *K* edge from $NiFe_2O_4$ films with varying film thickness. For comparison a Fe K-edge spectrum of Zn ferrite, which exhibits the normal spinel structure, is plotted (reproduced from [99]). The inset in Fig. 5.4(b) shows the integrated spectral weight of the Fe *K* edge pre-edge feature in dependence of the film thickness, where the dotted line represents the bulk value.

increased weight of the pre-edge feature. In the spinel structure a broken symmetry is given for cations on $T_d$, but not on $O_h$ sites.

XANES studies of the Fe *K* edge of various spinels clearly show a sharp pre-edge for all materials exhibiting the inverse spinel structure, where Fe cations are situated on $T_d$ sites. In contrast, the spectra of compounds featuring the normal spinel structure, in which Fe cations solely occupy $O_h$ sites, only show a weak broad feature [99]. In Fig. 5.4(b), this is exemplary shown by a XANES reference spectrum of the normal spinel $ZnFe_2O_4$ (reproduced from [99]).

The normalized pre-edge intensity can be quantitatively correlated to the local site symmetry of the investigated cation species [101]. By monitoring the Fe *K* edge pre-edge intensity of the $NiFe_2O_4$ samples, no intensity changes are resolvable between the various film thicknesses and also not in comparison to the bulk reference sample. We thus can conclude once more, that the ultrathin films do not undergo a cationic inversion, but remain in the bulk-like cationic distribution of the inverse spinel lattice. This is supported by the Ni *K* edge spectra (Fig. 5.4(a)), which also show no sign of an emerging pre-edge

feature, characteristic for Ni cations on $T_d$ sites.

Focussing on the main Fe *K* edge in Fig. 5.4(b), a chemical shift is expected for valency changes. A shift of about 5 eV between $Fe^{2+}$ and $Fe^{3+}$ for octahedrally coordinated iron oxides was observed previously [102]. A comparison of XANES spectra from bulk $Fe_3O_4$ with $NiFe_2O_4$, for which $Fe^{2+}$ cations are replaced by $Ni^{2+}$, reveals a chemical shift of about 3 eV, that has been explained by the missing $Fe^{2+}$ ions [103]. This energy shift has also been observed in other ferrites, where the $Fe^{2+}$ cations are substituted by a different cation species [99]. In all cases, the Fe-*K* edge of the $Fe^{2+}$-compounds was situated at lower binding energies. In our case, we observe no chemical shift of the main-edge across all film thicknesses, thus again supporting that no modification in the oxidation state of the Fe cations occurs, fully consistent with our HAXPES results.

The results of this in-depth XANES pre-edge analysis clearly reveal that $NiFe_2O_4$ films grow in the inverse spinel structure independent of their film thickness. Moreover, the position of the main *K* edges confirms, that the Fe and Ni cations in all samples are present in a bulk-like valency for all film thicknesses.

### 5.2.4. XMCD

In a last step, we analyse the XMCD asymmetry signal to quantitatively determine the cationic distribution across the spinel lattice sites. The XMCD asymmetry spectra are element-specific and sensitively influenced by the valency, the local lattice site symmetry and the magnetic ordering of the investigated cation species. The spectral details reflect the superposition of cations occupying $T_d$ or $O_h$ sites with either divalent or trivalent valency, respectively. Hereby, each configuration has its own characteristic MCD spectrum, which serves as a fingerprint for the certain atomic and geometric configuration. We thus modelled those four XMCD spectra, which allows us to fit them as a linear combination to the experimental data and to quantify the fraction of each configuration.

We investigated XMCD asymmetry spectra of the Fe $L_{2,3}$ edge to identify any changes in the distribution of Fe cations between $T_d$ and $O_h$ lattice sites for $NiFe_2O_4$ films with varying thickness. Site- and valency-specific Fe $L_{2,3}$ edge XMCD spectra were computed by LFM calculations utilizing the software CTM4XAS [104], which are presented in Fig. 5.5(b). Due to the antiferromagnetic alignment of the cation spins between $T_d$ and $O_h$ sites, their asymmetry signals are of opposite sign. Consequently, these signals mainly cancel out in the observable sum asymmetry signal, leaving the resulting difference spectrum extremely sensitive to subtle changes in the cationic distribution.

Fig. 5.5(a) exemplary shows the MCD spectrum of the Fe $L_{2,3}$-edge for the 2 nm thick $NiFe_2O_4$ film with the corresponding fit. The $L_3$-edge exhibits a pronounced -/+/- asymmetry structure, caused by the antiparallel oriented Fe moments. The positive (+) peak at 709.7 eV (II) is dominated by tetrahedral $Fe^{3+}$ and the high energy negative (-) peak at 710.5 eV (III) by octahedral $Fe^{3+}$ cations. The first negative peak at 708.5 eV (I) cannot be directly associated with the presence of $Fe^{2+}$ cations, because it appears both in the reference data of bulk $NiFe_2O_4$ [93] and in the model spectrum for $Fe^{3+}$ cations. Yet,

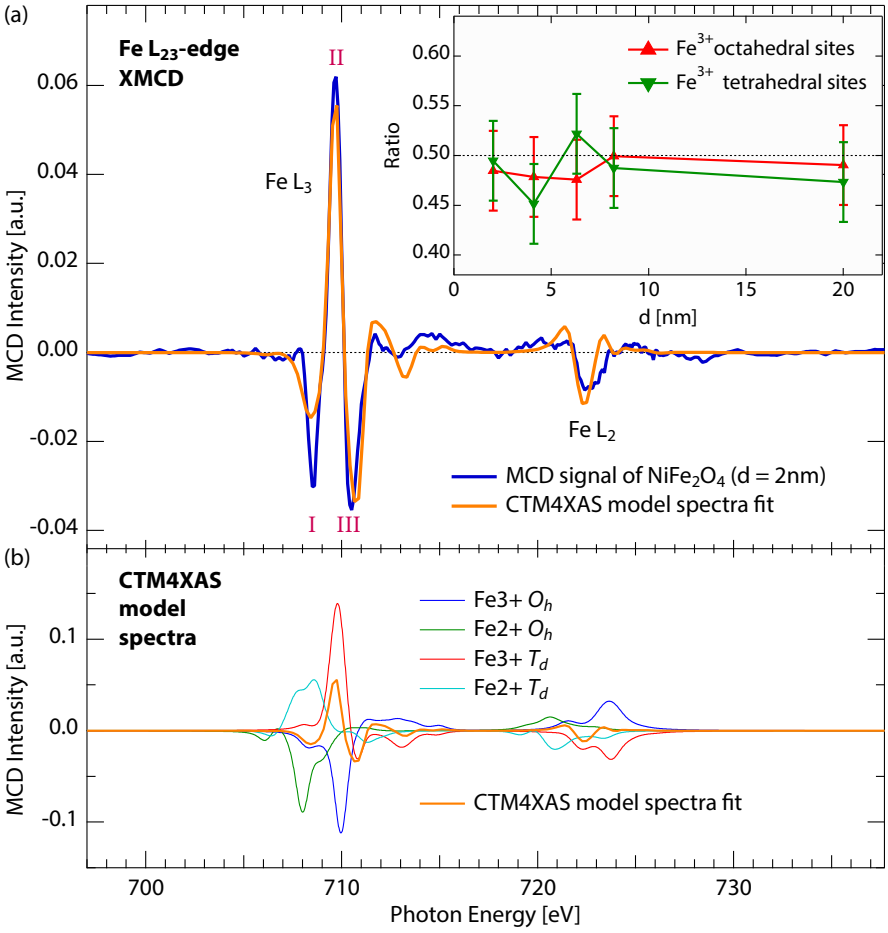


**Figure 5.5.:** Experimental XMCD spectrum from the Fe $L_{2,3}$ edge of the 2 nm thick $NiFe_2O_4$ film and the corresponding fit. The resulting lattice site occupancy for various film thicknesses is depicted in the inset.

the first peak is larger in comparison to the reference data, thus indicating the presence of a fraction of $Fe^{2+}$ cations at the surface, which is determined with ≈ 2 % from the model fit.

However, the result gives no indication for a cationic inversion of the film, which would result in a decrease of the positive peak (II) and strong enhancement of the high energy negative peak (III). These results are also observed for all other investigated $NiFe_2O_4$ film thicknesses, which give no clue for an increased octahedral $Fe^{3+}$ fraction, as would be characteristic for a cationic inversion to the normal spinel structure. This finding is in perfect agreement with electronic structure calculations, which find the fully inverse spinel lattice to be the ground state of bulk $NiFe_2O_4$ [32].

Since the XMCD spectra are recorded in TEY mode, the experiment probes the uppermost 2-3 nm of material. Complemented by the bulk-sensitive HAXPES and XANES techniques, the analysis yields a consistent picture of the stoichiometry, valency and cationic distribution of the $NiFe_2O_4$ thin films. In particular, we find that the cationic site occupancy always belongs to that of an inverse spinel lattice – this result is found both at the $NiFe_2O_4$ surface and in the bulk volume. This striking consistency provides clear evidence for the absence of a cationic inversion in $NiFe_2O_4$ in the crossover to the ultrathin film limit, and thus rules out this mechanism as the origin of the observed enhanced $M_S$ in ultrathin $NiFe_2O_4$ films.

## 5.3. Summary

In summary, we have investigated single-crystalline $NiFe_2O_4$ thin films grown cube-on-cube on Nb-doped $SrTiO_3$ (001) substrates, with thicknesses scaling down from 20 nm to 2 nm. In this crossover to the ultrathin film limit, we focussed on the impact of reduced dimensionality on the structural, electronic and magnetic $NiFe_2O_4$ properties. Foremost, we observed an enhanced saturation magnetization $M_S$ in ultrathin $NiFe_2O_4$ films. Despite the substrate-induced compressive in-plane strain, a reduced out-of-plane $NiFe_2O_4$ lattice constant is found, implying that a reduction of the unit-cell volume is energetically favourable. In order to investigate the cationic distribution in the $NiFe_2O_4$ thin films, complementing bulk- and surface-sensitive analyses using HAXPES, XANES and XMCD spectroscopy techniques have been performed, and special attention was paid to the element-specific cation valencies and -coordinations. We find a bulk-like inverse spinel structure being present in all samples – independent of the $NiFe_2O_4$ film thickness. Thereby, our results consistently reveal the absence of a cationic inversion from the inverse to the normal spinel structure, as was so far held responsible for an enhanced $M_S$ in ultrathin spinels. From our experimental results we find an auxetic behaviour, i.e. a structural unit cell reduction, in ultrathin $NiFe_2O_4$ films.

CHAPTER 6

# Spin and orbital magnetic moments in $NiFe_2O_4$ ultrathin films

In the previous chapter, a cationic inversion in the spinel structure was ruled out as a possible source of the observed enhanced magnetization in $NiFe_2O_4$ ultrathin - which was so far responsible. So far, an explanation for this phenomenon is still missing, and also not present in literature. Therefore, the local element-specific magnetic structure of the $NiFe_2O_4$ films is investigated in detail. X-ray magnetic circular dichroism (XMCD) spectra of the Fe $L_{2,3}$ and Ni $L_{2,3}$ edge are recorded at low temperatures for the same series of samples as already discussed in the previous chapter in order to investigate the element-specific contributions to the net magnetization of the films.

## 6.1. Experimental details

In this section the experimental setup, as well as the analysis of the collected data will be discussed. The data processing is based on the methods described in [105], which are used in the group of K. Fauth. Here, the same sample series as in chapter 5 is investigated, whereby growth conditions can be found in section 5.1.

### 6.1.1. Experimental setup

The data for all XMCD spectra presented in this chapter were recorded at the bending magnet beam line PM3 at BESSY-II, which provides a finite circular polarization of $0.93 \pm 0.02$ %. XMCD spectra of $NiFe_2O_4$ thin films were recorded at temperatures of $13 \pm 1$ K. The sample was attached to a cryostat, which allows temperatures down to 12 K. The used end station provides a liquid helium cooled superconducting magnet

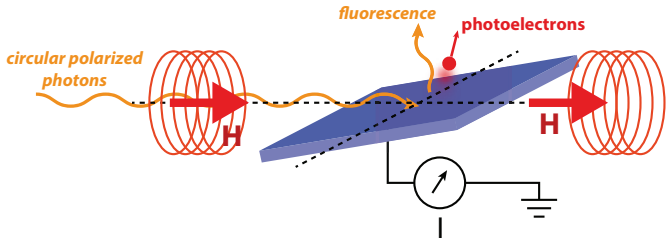


**Figure 6.1.:** Schematic drawing of the XMCD experiment: The incident beam is aligned parallel to the direction of the applied magnetic field. The X-ray absorption of the sample is recorded in total electron yield (TEY) mode.

in a Helmholtz coil geometry, which allows to apply magnetic fields of up to 3 T. The direction of the magnetic field is always aligned parallel to the direction of the incident beam, as depicted in Fig. 6.1. The X-ray absorption signal of the sample was recorded in total electron yield (TEY) mode and has been normalized to the incoming photon beam intensity $I_0$. To determine $I_0$ a gold grid was placed in the X-ray beam path which generates a photo-current that is proportional to the intensity of the beam and the energy dependent photoionization cross section of the grid.

### 6.1.2. Energy calibration

The monochromator of the beam line does not exactly reproduce the same photon energies for each measurement run, i.e. because of slow drifts of the X-ray beam position coming from the bending magnet. Thus, all recorded spectra need to be corrected in energy. Therefore, a known Fe- or Ni-reference wire is placed in the beam and its X-ray absorption is recorded simultaneously during each measurement using an extra picoammeter. Afterwards, the absorption spectra of the reference wire are aligned in energy with respect to each other, resulting in an energy offset for each recorded spectrum. The latter is then used to correct the energy shifts between different sample absorption spectra. Since only relative shifts between the spectra are corrected, an absolute correction of all spectra is still required, i.e. by recording the absorption spectra of a known reference sample if available. It is important to know that the resolution $\Delta E$ of the used SX700 monochromator scales with $E^{3/2}$ [106]. Thus, if the data point at $E_0$ (e.g. the Fe $L$ edge of the reference wire) is shifted by $\Delta E_0$ the energy of all other data point at energy $E_i$ in the spectrum needs to be shifted by:

$$\Delta E_i = \left(\frac{E_i}{E_0}\right)^{3/2} \Delta E_0 \tag{6.1}$$

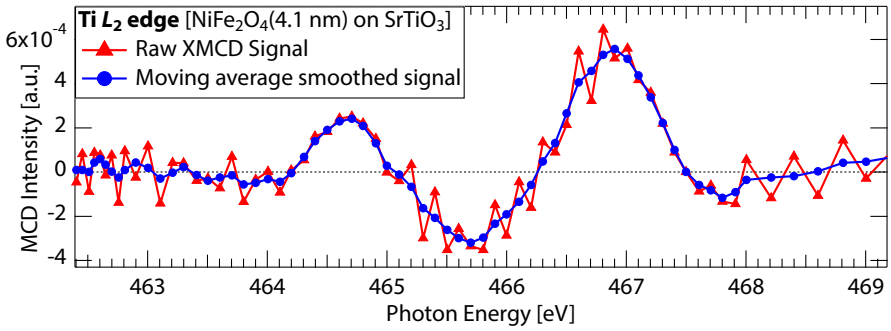


**Figure 6.2.:** Raw (red line) XCMD spectrum of the Ti $L_2$ edge. Due to the switching of the magnetic field at every data point alternating deviations are modulated onto the signal. These can be corrected by a trapezoidal rolling average (blue line).

### 6.1.3. Recording of the XMCD spectra

For the determinations of an dichroic spectrum, it is required to record two absorption spectra under an applied magnetic field, whereby the field direction needs to be reversed between the spectra. It is also possible to change the polarization of the incident beam, which however is quite time consuming at the PM3 beamline. It is obvious, that an energy drift between these two spectra would impair the resulting difference spectrum. To overcome this problem, the magnetic field is switched at every data point. Thereby, both absorption spectra are recorded in one measurement run, and thus effects due to time dependent energy or intensity drifts of the synchrotron radiation are minimized. All XMCD spectra presented in this chapter have been recorded under an applied magnetic field of 10 kOe, which was aligned (anti)parallel to the direction of the incident X-ray beam.

### 6.1.4. Effects of the magnetic field

Unfortunately, the switching of the magnetic field induces a new problem, due to the used electron yield detection mode, which involves the measurement of the photo-current. Because of capacitive loads in the measuring circuit, the current asymptotically approaches its final value, after each field switching. This would imply an infinitive waiting time for each data point, which is not feasible. In practice, the idle is limited and thus an alternating error is modulated onto the spectra (sample, $I_0$ and the calculated MCD), which is shown by the red line in Fig. 6.2. Since the error between two switching processes is of opposite sign, it can be reduced by averaging over three adjacent data points, as depicted by the blue line in Fig. 6.2.

$$I_n(\text{corrected}) = 0.25\, I_{n-1} + 0.5\, I_n + 0.25\, I_{n1} \quad \text{where } I_n \text{ is the } n\text{-th data point.} \quad (6.2)$$

Due to the Lorentz force, the photoelectrons emitted by the sample are forced onto spiral trajectories by the applied magnetic field. Consequently, many photoelectrons are returning towards the sample, and can not be detected in the photo current any more. Thus, this effect is reducing the signal, and consequently the realizable signal-to-noise ratio. Therefore, a bias voltage of –100 V is applied to the sample, which accelerates the electron away from the sample and thus reduces the amount of backscattered electrons [107].

Yet, the influence of the magnetic field onto the electron trajectories has another drawback, that needs to be considered. Since it is almost impossible to design the experiment completely axially symmetric, with respect to the direction of the magnetic field, also the electron trajectories are not fully symmetric. For this reason, the recorded photo current can differ by an offset while switching the magnetic field direction, even if the sample shows no dichroic effect at this photon energy [108]. This would result in an offset in the resulting MCD spectrum and needs to be corrected. Therefore, one of the two sample absorption spectra is linearly scaled in a way that the two match at all energies were no dicroic response is expected (e.g. the pre and post edge region). Also, the $I_0$ spectrum needs to be corrected this way, since the gold grid experiences the magnetic fields from the sample chamber as well.

## 6.2. Sum rules

In this chapter, the element specific magnetic properties of the Ni and Fe cations in $NiFe_2O_4$ thin films will be estimated from their XMCD spectra. For this purpose, two important magneto-optical sum rules are employed, which have been derived for electric dipole transitions in a localized model, considering a single ion in an arbitrary crystal-field symmetry and including hybridization effects [22, 23]. They allow to determine the orbital [22] and spin [23] magnetic moments of 3*d* transition metals from XMCD data and the corresponding XAS spectrum.

$$m_{\mathrm{Orb}} = -\frac{2q}{3r} N_h \tag{6.3}$$

$$m_{\mathrm{Spin}} = \frac{-3p + 2q}{r} N_h \left(1 + \frac{7\langle T_z \rangle}{2\langle S_z \rangle}\right)^{-1} \tag{6.4}$$

$$p = \int_{L_3} (\sigma^+ - \sigma^-)\, d\omega \quad q = \int_{L_{3,2}} (\sigma^+ - \sigma^-)\, d\omega \quad r = \frac{1}{2} \int_{L_{3,2}} (\sigma^+ + \sigma^-)\, d\omega \tag{6.5}$$

Hereby, $m_{\mathrm{Orb}}$ and $m_{\mathrm{Spin}}$ are the orbital and spin magnetic moments in units of $\mu_B$/f.u. and $N_h$ is the number of 3*d* holes per formula unit of the investigated metal cation. $p$ and $q$ are the integrals of the XMCD spectrum over the $L_3$ edge and both $L_{3,2}$ edge, respectively. $r$ describes the integral over the $L_{3,2}$ edge of the XAS spectrum. $\sigma^+$ and $\sigma^-$ represent the two absorption spectra that are recorded under inverse magnetization or polarization.

The integrals have been exemplary plotted for the Ni $L_{3,2}$ edge of $NiFe_2O_4$ in Fig. 6.3. The sum rules have been experimentally evaluated for Fe and Co-metal [109]. The spin sum rule includes the intra-atomic magnetic dipole operator $T_z$ which is only present for systems with symmetry less than cubic and thus can be neglected in our case [110].

## 6.3. Background substraction

To apply the sum rules, the term $r = 1/2 \int_{L_{3,2}} (\sigma^+ + \sigma^-)$ in the denominator has to be determined, which is given by the area below the $L_{3,2}$ edge in an unpolarized XAS spectrum. The latter can be determined by averaging the two absorption spectra recorded under opposite magnetization direction. The integral is proportional to the number of $3d$ valence states per formula unit of the investigated cation species. However, above the $L_3$ and $L_2$ edge also transitions into higher final states than the $3d$ final states are allowed, which are contributing as a continuum above the absorption edges. These are responsible for the characteristic edge jump and need to be removed. The top part of Fig. 6.3 exemplary shows an X-ray absorption spectrum of the Ni $L_{2,3}$ edge from an 8 nm thick $NiFe_2O_4$ film. To remove the background, the edge jumps need to be modelled by a step function. Itinerant magnets (e.g. $3d$ metals) one typically uses a two-step function [109], whose thresholds are set to the maxima of the $L_3$ and $L_2$ edge. The height of these steps is set to $2/3$ ($L_3$ edge) and $1/3$ ($L_2$ edge) of the height of the XAS-spectrum after the $L_{2,3}$ edge. These value correspond to the quantum degeneracy, e.g. the number of the possible initial states of the spin-split $2p$ core-levels. In contrast, in localized $3d$ electron systems like $NiFe_2O_4$ the $L$ edge reveals much more fine structure due to the pronounced atomic multiplet splitting. In principle, each multiplet transition would contribute its own continuum step edge to the background, which is difficult to model. Yet, in the case of the magnetite Fe $L$ edge using a simple two-step function turned out to yield reasonable results [111].

Thus, we also employ a two-step function for the treatment of the Fe $L$ edge. First, a straight line is fitted to the $L_3$ pre-edge region and is subtracted as a linear background. Next, we define two step edges at 710.9 eV (maximum of $L_3$ edge) and 723.5 eV. The step function is modelled using the the software Unifit 2013 [112], which calculates the step edges by a superposition of the error function and the arctangent function (which are the convolution of the Θ-function with the Gaussian- or Lorentzian distribution). Here, both are contributing equally and are broadened by a FWHM of 2 eV[1]. Finally, the background function is subtracted and the integral below the XAS spectrum can be calculated.

However, in case of the Ni $L$ edge of $NiFe_2O_4$ the background subtraction is more complex. Again, we start from a two-step function with step edges at 854.3 eV (maximum of $L_3$ edge) and 872.0 eV, which is depicted by the green line in Fig. 6.3. It is obvious that the region between the $L_3$ and $L_2$ edge is problematic (label A), since the XAS spectrum

[1] The broadening of the step edges has no influence onto the derived area below the XAS spectrum, but is important if one wants to fit the XAS spectrum since the shape of the peaks are affected.

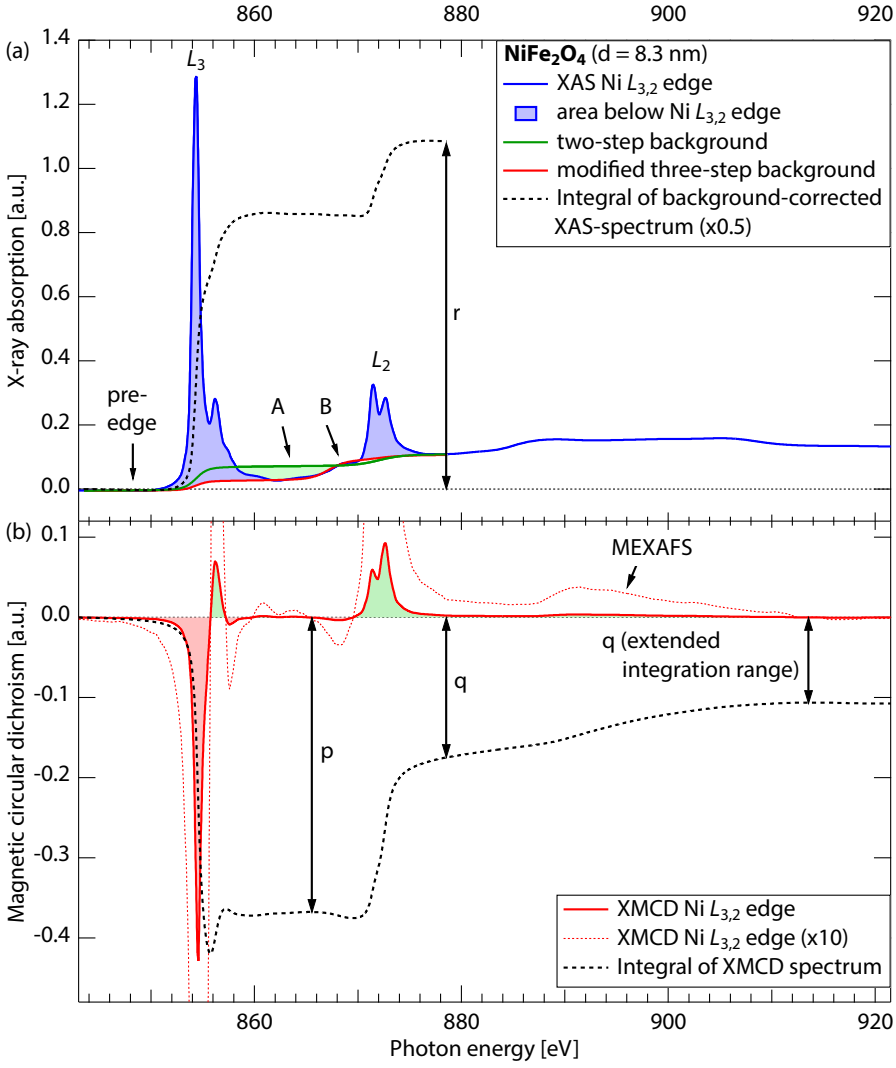


**Figure 6.3.:** (a) X-ray absorption spectrum of the Ni $L_{3,2}$ edge from a 8 nm thick $NiFe_2O_4$ film recorded at 70° off-normal beam incidence together with the two discussed step-edge function to model the background are shown. The dashed line illustrates the integral of the absorption spectrum after background substraction. (b) Corresponding Ni $L_{3,2}$ edge XMCD spectrum and its integral. The dashed line is the same spectrum scaled by a factor of 10 to emphasize the spectral weight existent in the energy region above the $L_2$ edge.

falls below the background function and thus would become negative after subtraction (green shaded area). For this reason, additional contributions to the background need to be considered. A closer look at the XAS spectrum reveals a gradual increase of the absorption (label B) in front of the Ni $L_2$ edge, which has been explained as follows: The sudden creation of a $2p$ core hole in XAS can induce an excitation of an electron from the ligand into the continuum state above the ionization threshold [113, 114], and thus has not to be treated as a $2p \rightarrow 3d$ transition. For this contribution an extra step edge is introduced at 867.1 eV, whose height and width is carefully adjusted to match the increase in the XAS spectrum. The resulting background is given by the red line in Fig. 6.3 and does not create negative contribution in background corrected XAS spectrum any more. The integrated XAS spectrum after background subtraction is plotted as the dashed line in Fig. 6.3.

## 6.4. Magnetic moments of Fe in $NiFe_2O_4$ thin films

In a first step, the Fe $L_{3,2}$ edge XMCD of $NiFe_2O_4$ with respect to the film thickness will be discussed. In section 5.2.4, we have already examined the XMCD spectra recorded at room temperature, which have been used to identify the cationic distribution in the spinel structure of the $NiFe_2O_4$ thin films. This analysis of the cationic distribution can also be applied to the measured XMCD spectra recorded at low temperatures of $T = 12 - 14$ K. We find, the resulting cation distribution comparable to the results at room temperature. Thus, also a change of the spinel structure at low temperatures can be ruled out.

We will now focus onto the contribution of magnetic moments from the Fe cations to the net moment of the films. Therefore, the sum rules are applied to the data and special attention is paid to the thickness dependence of the Fe spin and orbital magnetic moments.

### 6.4.1. Review of the XMCD spectra

Fig. 6.4 depicts the XMCD spectra from the Fe $L_{3,2}$ edge of $NiFe_2O_4$ thin films with thicknesses decreasing from 8.3 nm to 1.0 nm. The two sub-figures (a) and (b) show the same data, but with different scaling of the amplitude and the energy axis. The amplitude of the spectra has been normalized by scaling them down by a factor proportional to the area below the Fe $L_{3,2}$ peaks in the absorption spectra[2]. The absolute energy axis has been calibrated by comparing the spectrum of the 8.3 nm thick film with reference data of magnetite taken from [115]. Then, the positions of the $L_3$ edge minimum at 710.2 eV and the maximum at 710.9 eV were matched to the corresponding features in the magnetite data. $NiFe_2O_4$ and $Fe_3O_4$ can be compared, since both are structurally and chemically compatible and only $Ni^{2+}$ cations in $NiFe_2O_4$ are substituted by $Fe^{2+}$ cations in $Fe_3O_4$. This is supported by the positions of the mentioned spectral features, which varies by

[2] In Fig. 6.3 this is illustrated by the blue shaded area for the case of the Ni $L$ edge.

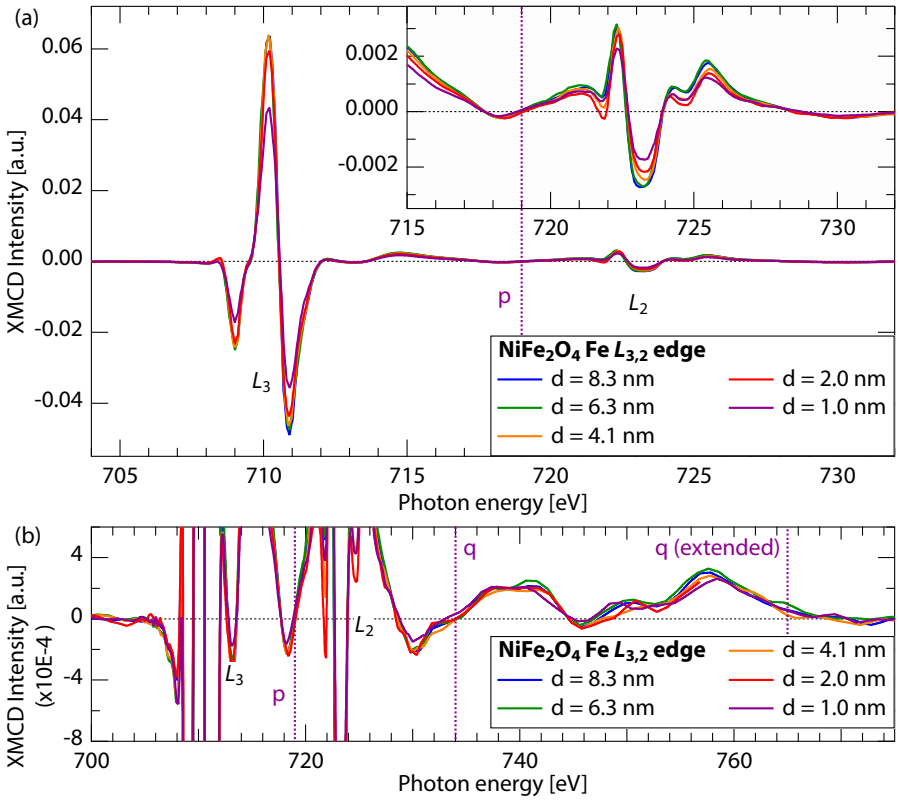


**Figure 6.4.:** (a) XMCD spectra of the Fe $L_{3,2}$ edge of $NiFe_2O_4$ thin with thicknesses between 1.0-8.3 nm recorded at $T$ = 12 – 14 K and 10 kOe in normal beam incidence (Inset: zoom of the $L_2$ edge). (b) The same spectra enlarged to present the contributions to the MCD signal above the $L_2$ edge. $p$ and $q$ denote the upper integration limits used for the sum rules.

less than 0.07 eV between the two compounds as determined from ligand field multiplet calculations. At first glance, the data reveals no emerging or disappearing spectral features while turning over from thicker films to the ultrathin film limit. However, the amplitude of the spectra is dropping with decreasing film thickness. This implies, that the long range order of the spins is decreasing and fluctuations of them are becoming more prominent. This can be argued by the reduction of the dimensionality from 3D to 2D, e.g. the thickness of the 1 nm film corresponds to 1.2 unit cells of $NiFe_2O_4$. However, these results do not coincide with the SQUID data discussed in section 5.2.1.

### 6.4.2. Application of the sum rules

Next, the sum rules are applied to the XMCD and XAS spectra. Hereby, one first needs to choose the right integration ranges for the integrals in Eq. 6.5. For the correct determination of the spin moments two sources of errors need to be considered. The first is the spectral overlap, which means that the areas below the $L_3$ and $L_2$ edge need to be well separated. Otherwise, the area belonging only to the $L_3$ edge would be also counted by the integral that is determining the area of the $L_2$ edge and vice versa. However, the hereby introduced error is small since in the overlapping region the XMCD intensity which belongs to the $L_2$ but is transferred to the $L_3$ edge is equal to the transfer in the opposite direction [116, 117]. The second source of error can occur in systems with small spin-orbit splitting, where the $L_3$ and $L_2$ edge are in close proximity. In this case, the excitation from the spin-split ground states are quantum mechanically mixed, the so-called $jj$ mixing. This mixing can reduce the spin moment derived from the sum rules by a factor of up to 2 [116] rendering the sum rules inappropriate for this case. In case of Fe and Ni in $NiFe_2O_4$ the $L_{3,2}$ edges are well separated which is clearly visible in Fig. 6.4 and 6.8 and thus we can apply the sum rules. For the Fe $L_3$ edge we employ an integration range from 700 to 719 eV, whereby the upper limit is marked by line p in Fig. 6.4.

The next issue is to chose the proper end of the integration range over the $L_2$ edge. In the case of magnetite there is an open discussion about the presence of a large orbital moment of the Fe cations. Previously, these moments have been evaluated by XMCD and a large unquenched orbital moment of $0.33\,\mu_B$/f.u. has been found for Fe cations on $O_h$ sites using an upper integration limit of 739 eV [118]. However, later this result was questioned, if an extended integration range with an upper limit of 765 eV was chosen [111]. Hereby, it was argued that the extended fine structure of both Fe $L$ edges (EXAFS) contains a significant contribution to the dichroic signal, which is called magnetic extended fine structure (MEXAFS) [119]. Therefore, the MEXAFS from the $L_3$ edge is superimposed with the the $L_2$ edge signal, which would modify the sum rule result. However, the MEXAFS signal is strongly damped at higher excitation energies. Thus, the dominating MEXAFS parts of the $L_3$ and $L_2$ edges, close to the excitation threshold, have an opposite sign and cancel each other out by choosing a longer integration range, that covers the whole region of dichroic response [111, 119]. As a result, the proposed quenched orbital moment in magnetite vanishes and a moment of $-0.001\,\mu_B$/f.u. was determined. In the case of $NiFe_2O_4$ we can also observe these MEXAFS contributions to the dichroic response of the Fe $L$ edge in the region up to 765 eV as evident from Fig. 6.4(b). Therefore, we also apply the extended integration region, which is marked by *q (extended)*.

Using the extended integration limits, the sum rules are applied to all Fe $L$ edge XMCD spectra of $NiFe_2O_4$ thin films. Therefore, the $3d$ electron hole number $N_h$ is required, which can be obtained from theoretical calculations of the electronic structure of the material. In [120] a configuration-interaction cluster model has been used to determine the number of $3d$ electrons in transition metal oxides, resulting in a hole number of $N_h$ = 9.4/f.u. for a system with two $Fe^{3+}$ cations per f.u.. This is supported by electronic

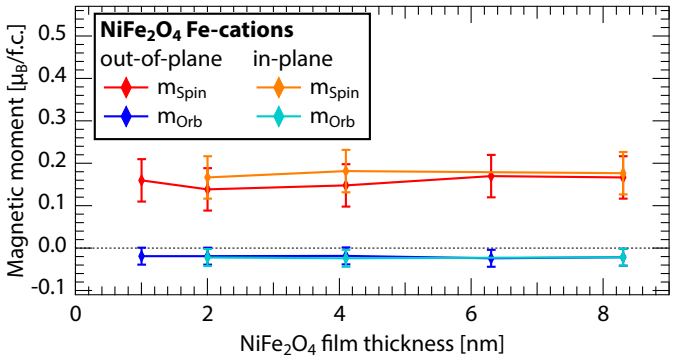


**Figure 6.5.:** Spin- ($m_{\mathrm{Spin}}$) and orbital ($m_{\mathrm{Orb}}$) magnetic moments of the Fe-cations in $NiFe_2O_4$ thin film as a function of film thickness.

structure calculations of $NiFe_2O_4$ using a local-density approximation (LDA) approach in combination with a modified Becke–Johnson (mBJ) exchange potential, which finds the number of $3d$ holes of the $Fe^{3+}$ cations to be $N_h \approx 9.35$/f.u. [121]. Thus, the latter value will be used in the following. The derived results are depicted in Fig. 6.5. The shown in- and out-of-plane values are corresponding to measurements that have been performed under an applied magnetic field parallel to the respective film direction.

### 6.4.3. Discussion

In the bulk spinel structure of $NiFe_2O_4$, $Fe^{3+}$ cations are equally distributed across tetrahedral and octahedral lattice sites (see Fig. 6.6(a)). They are present in a $3d^5$ electron configuration with a completely filled majority shell, e.g. all spins are aligned parallel. Thus, from a simplified view, all orbital moments are expected to be compensated already on an atomic level. In contrast, the Fe cation exhibits a spin magnetic moment of $5\,\mu_B$/atom, which is cancelled out on a macroscopic scale by the antiferromagnetic coupling of the cations on $T_d$ and $O_h$ sites. In a perfect antiferromagnet no XMCD signal is expected at all. However, in the spinel structure the Fe cations occupy inequivalent lattice sites, resulting in a dichroic response despite of the antiferromagnetic coupling.

The spin magnetic moments recorded under an in-plane field geometry are enhanced to the out-of-plane ones by 6 – 22 %. This can be attributed to the fact that the $NiFe_2O_4$ films are very hard to saturate and are not completely driven into saturation at a field of 10 kOe. The deviating moments then reflect the shape anisotropy of the thin films, whereby the in-plane direction is favoured. The results from the sum rules yield orbital moments of $m_{\mathrm{Orb}} = -0.02 \pm 0.02\,\mu_B$/f.u. for all films consistent with the expectation from the electron configuration. Exemplary, we have also determined the orbital moments with a shorter integration range for the $L_2$ edge with an upper limit of 734 eV. Hereby, orbital

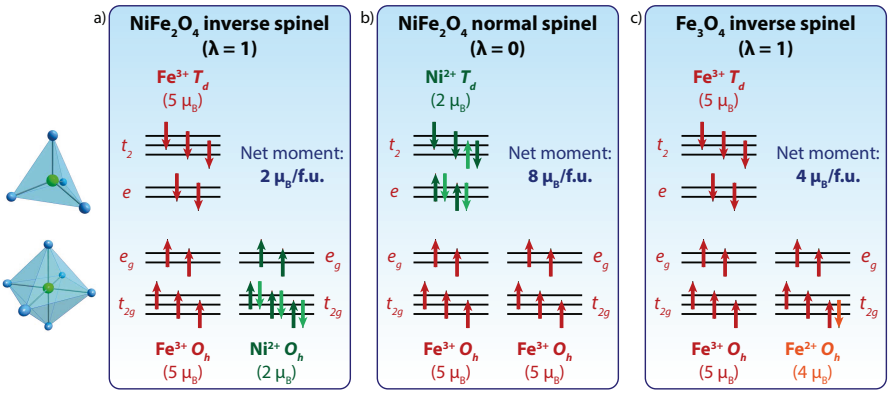


**Figure 6.6.:** Electronic configurations of the cations for varying cationic distributions: (a) In the default bulk $NiFe_2O_4$ inverse spinel structure, Fe cations are antiferromagnetically coupled and only the two unpaired Ni-electrons contribute to the net magnetization. (b) In the inverse spinel structure, both Fe cations are coupled ferromagnetically, thus only two of the ten electron spins are compensated by Ni. (c) In magnetite, the $Ni^{2+}$ cations of $NiFe_2O_4$ in the inverse spinel structure are substituted by $Fe^{2+}$

moments of around $m_{\mathrm{Orb}} = 0.01 \pm 0.02\,\mu_{\mathrm{B}}/\mathrm{f.u.}$ are derived rendering that the influence of the MEXAFS contribution should be less significant than in the case of magnetite. The spin magnetic moments are all in the scale of $m_{\mathrm{Spin}} \approx 0.14 - 0.17\,\mu_{\mathrm{B}}/\mathrm{f.u.}$, reflecting that the moments of the antiferromagnetic coupled Fe cations do not completely compensate each other. One explanation could be that the spins are slightly canted. However, by an analysis of the element specific hysteresis loops, we find that the hysteresis of Fe and Ni show the same behaviour, which is exemplary depicted in Fig. 6.7. This implies, that the Fe and Ni spins in each magnetic domain are present in a collinear alignment and that the domains are always flipping entirely while switching the applied magnetic fields. Another possibility is that the films still exhibit a finite off-stoichiometry, where a minority portion of the Ni cation on $O_h$ sites is replaced by $Fe^{2+}$ cations. This would be consistent with the small fraction of $Fe^{2+}$ cations that has been identified from the comparison of room-temperature XMCD measurements with ligand field multitplet calculations in section 5.2.4. Surprisingly, the Fe spin- as well as the orbital magnetic moments behave approximately constant with respect to the film thickness and show no major deviations as one could expect from the results of the SQUID measurements (see also Fig. 5.2). We also analyse the Ni moments in a next step in order to get a full picture.

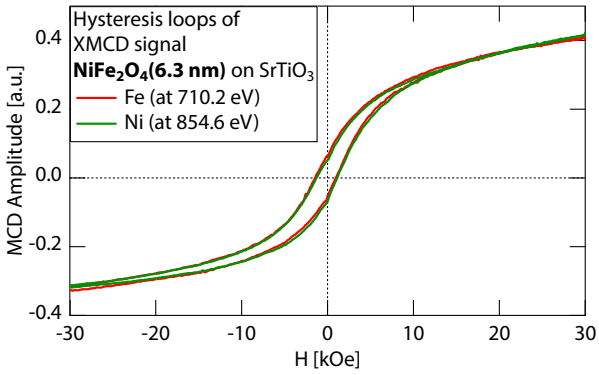


**Figure 6.7:** Element specific hysteresis loops have been determined from the field dependent X-ray absorption at the photon energies, where the maximum dichroic response in the $L_{3,2}$ absorption edge of the element is observable. The corresponding photon energies are denoted in the legend.

## 6.5. Magnetic moments of Ni in $NiFe_2O_4$ thin films

Next, the influence of the $NiFe_2O_4$ film thickness onto the spin and orbital magnetic moments of the Ni cations shall be discussed. The thickness dependent Ni $L_{2,3}$ edge XMCD spectra are plotted in Fig. 6.8. The spectra have been normalized by the area below the XAS of the Ni $L_{2,3}$ spectrum, in a similar way as in the case of the Fe $L$ edge spectra discussed in section 6.4.

### 6.5.1. Review of the XMCD spectra

In comparison with ligand field multiplet (LFM) model spectra and $NiFe_2O_4$ bulk reference data [113], all spectra reveal a shape that is expected for the presence of divalent Ni cations on octahedral lattice sites. In particular, there is no sign for Ni on tetrahedral lattice sites, which could be identified by a characteristic positive peak at 854.2 eV. A detailed discussion on the spectral features in the XMCD spectrum can be found in [113]. The behaviour of the MCD amplitude is similar to the case of the Fe $L$ edge. While it is almost constant for film thicknesses from 8.3 to 2 nm it drops for the ultrathin film with a thickness of only 1 nm.

### 6.5.2. Application of the sum rules

For the calculation of the magnetic moments using the sum rules again an extended integration range is appropriate. Comparable with the Fe $L$ edge also the Ni $L$ edge shows a significant contribution to the dichroic signal above the $L_2$ edge as can be identified by the dashed line in the bottom part of Fig. 6.3. Again, these contributions can be identified with MEXAFS oscillations from the $L_3$ and $L_2$ edge. For this reason, the same arguments, that have already been discussed for the Fe $L$ edge, are appropriate here and thus justify the usage of the extended integration range (marked by *q (extended)* in Fig.

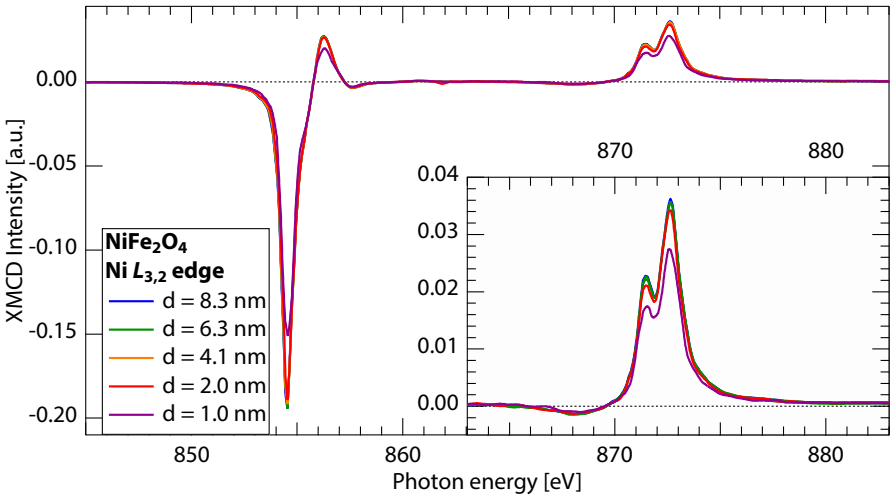


**Figure 6.8.:** XMCD spectra of the Ni $L_{3,2}$ edge of $NiFe_2O_4$ thin films with thicknesses between 1.0-8.3 nm recorded at $T$ = 12 – 14 K and $H$ = 10 kOe in normal beam incidence

6.3). In summary, we use the range from 843.5 eV to 865.5 eV for the calculation of the area below the $L_3$ edge and the range from 843.5 eV to 913.5 eV for both edges. According to [121] the number of $3d$ holes of the $Ni^{2+}$ cations in $NiFe_2O_4$ is $N_h \approx 2.23$/f.u. Also here, the in-plane measurements result in an spin magnetic moment which is in increased by 11 – 16 % in comparison to the out-of-plane measurements as shown in Fig. 6.9. In contrast, the orbital magnetic moment seems to be independent from the direction of the applied magnetic field.

### 6.5.3. Discussion

The $Ni^{2+}$ cations exhibit a $3d^8$ electron configuration. Thus, the lower lying $t_{2g}$ states are fully occupied and do not contribute to the spin or orbital magnetic moment. The remaining two electrons are aligned parallel and fill the two $e_g$ levels. Considering only the occupation of the $e_g$ orbitals the orbital quantum number would be completely quenched since both orbitals are occupied equally and thus no orbital moment is expected. However, taking into account spin-orbit coupling an orbital polarization is introduced by a second-order spin-orbit interaction [113]. Hereby, the contribution of orbital moment to the total magnetic moment of the Ni cations in $NiFe_2O_4$ has been determined to be 12 ± 2 %.

Focussing on the results from our measurement, we find a spin magnetic moment of $m_{Spin} = 0.78 \pm 0.05\,\mu_B$/f.u. and an orbital moment of $m_{Orb} = 0.09 \pm 0.03\,\mu_B$/f.u. for the 8 nm thick $NiFe_2O_4$ film. In contrast to the Fe moments, these values are slightly decreasing with film thickness and decrease down to $m_{Spin} = 0.63 \pm 0.05\,\mu_B$/f.u. and

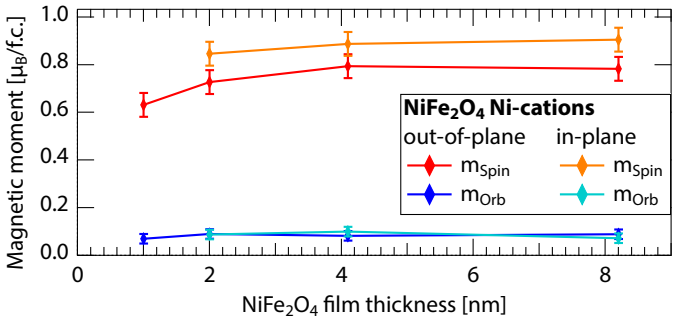


**Figure 6.9.:** Spin- ($m_{Spin}$) and orbital ($m_{Orb}$) magnetic moments of the Ni-cations in $NiFe_2O_4$ thin film as a function of film thickness.

$m_{Orb} = 0.09 \pm 0.03\,\mu_B$/f.u. for the 1 nm thick film. The orbital moment accounts with $10 \pm 2$ % to the total magnetic moment, consistent with the above mentioned result from [113]. The net moments are clearly below the value expected for bulk $NiFe_2O_4$, where the Ni cations should account with a net magnetic moment of $\approx 2\,\mu_B$/f.u.. The summation of all magnetic moments from the Fe and Ni cations for the 8 nm thick film results in $1.1 \pm 0.1\,\mu_B$/f.u.. This value is lower in comparison to the bulk moment and also below the results from the SQUID hysteresis loops (see Fig. 5.2) where a moment of $1.5 \pm 0.1\,\mu_B$/f.u. was measured. This can be explained by non-uniform distribution of the magnetic order throughout the film, i.e. one can think of a layer with reduced magnetic exchange interactions at the film surface, which is caused by the reduced dimensionality at the surface. Since the X-ray absorption spectroscopy is a very surface sensitive technique such a dead layer would become more prominent in the XMCD data. More surprisingly is that while the saturation magnetization determined from SQUID increases with decreasing film thickness, the summed magnetic moments from the XMCD experiments decrease. This contradiction cannot be explained from the data so far, thus we will proceed with investigating the $NiFe_2O_4/SrTiO_3$ interface. To sum up, we have found the orbital and spin magnetic moments to decrease with decreasing film thickness. However, these results are not able to explain the observed enhanced magnetization shown in Fig. 5.2.

## 6.6. Ti magnetism at the $NiFe_2O_4/SrTiO_3$ interface

So far, we investigated the magnetic properties of the 3*d* transition metal cations of the $NiFe_2O_4$ film in detail, whereby we did not find an explanation for the observed enhanced magnetization of the ultrathin film samples. Also, the pristine $SrTiO_3$ substrate did not reveal any ferromagnetic contribution, as already discussed in section 3.4.1. However, recent investigations of the oxide interface between $SrTiO_3$ and a number of perovskites revealed emerging physical properties which are absent in the participating oxides itself.

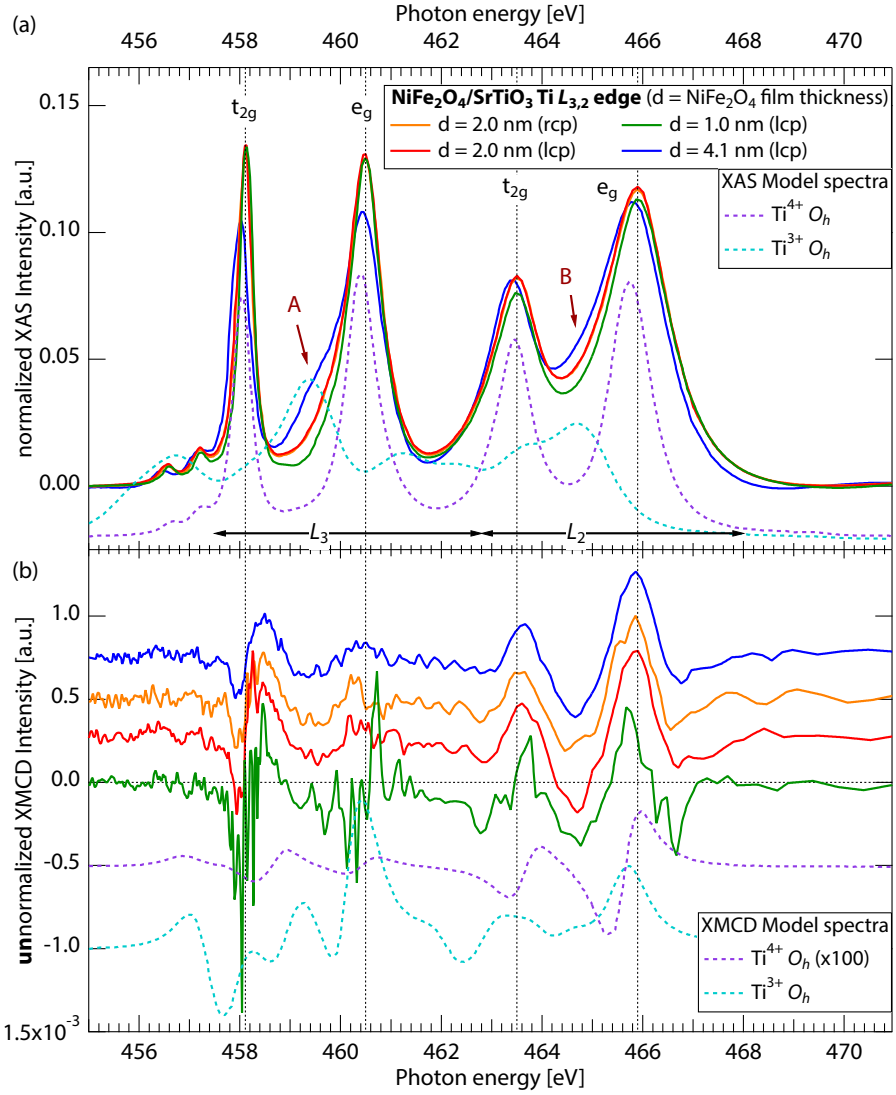


**Figure 6.10.:** XAS and XMCD spectra of the Ti $L_{3,2}$ edge of $SrTiO_3$ substrates covered by $NiFe_2O_4$ films with thicknesses between 1.0-4.1 nm recorded at $T = 12-14$ K and $H = 10$ kOe in normal beam incidence. The polarization of the incident X-ray beam is denoted in brackets. For comparison, calculated model spectra from multiplet calculations are plotted (reproduced from [18]).

For example, at the interface between the insulating and non-magnetic oxides $SrTiO_3$ and $LaAlO_3$ a conductive two-dimensional electron-gas has been found [15] as well as an emerging ferromagnetic ordering of the Ti cations [18]. Also, at epitaxial $LaMnO_3/SrTiO_3$ interfaces Ti ferromagnetism has been reported [122]. Motivated by these investigation, we also moved our focus onto the interface between the $NiFe_2O_4$ films and $SrTiO_3$ substrates. As a major result, we found that the Ti cations of $SrTiO_3$ substrate also reveal a ferromagnetic ordering, which we prove by XMCD measurements.

### 6.6.1. XMCD of the Ti $L_{3,2}$ edge

We have recorded XMCD spectra of the Ti $L_{3,2}$ edge from the 0.1 % Nb doped $SrTiO_3$ substrates below the $NiFe_2O_4$ films. Since the employed TEY detection mode is very surface sensitive, only the samples with $NiFe_2O_4$ film thicknesses below 4.1 nm have been investigated, where the Ti signal of the substrate was still visible. The resulting XAS and XMCD spectra are presented in Fig. 6.10 and show a clear dichroic response for all three investigated samples. To rule out any instrumental artefacts, the Ti $L$ edge XMCD spectrum of the substrate covered by 2 nm $NiFe_2O_4$ has additionally been recorded under reversed circular polarization of the incident X-ray beam. The clear match of the MCD spectra between the samples with varying $NiFe_2O_4$ film thickness as well as under reversed polarization undoubtedly proves the measured dichroism to be a characteristic feature of the samples, which implies a spin splitting of the electronic states at the Ti sites. However, the underlying exchange interaction responsible for the spin splitting is not clear.

In bulk $SrTiO_3$, the Ti cations shall be present in a purely tetravalent state ($Ti^{4+}$). It is obvious that the $3d^0$ configuration of $Ti^{4+}$ cannot cause a ferromagnetic polarization of the Ti electrons. If Ti is present in a tetravalent state it has donated its $4s^2$ and $3d^2$ electrons to the ionic bond with oxygen. Thus, $SrTiO_3$ is forming a valence band which is predominantly formed by the fully occupied O $2p$ orbitals and a conduction band which is mainly formed by the empty Ti $3d$ states, which are split by a indirect band gap of 3.25 eV [123]. The $Ti^{4+}$ cations are surrounded by six oxygen anions forming an octahedral symmetric ($O_h$) environment. Thus, the Ti $3d$ levels are split by the crystal field into the lower lying threefold degenerate $t_{2g}$ and the higher lying twofold degenerate $e_g$ states. Since the $3d$ levels are completely unoccupied, the spin- and angular momenta of the Ti electrons in bulk $SrTiO_3$ are completely determined and have no degree of freedom. Hence, we need to discuss possible effects which can result in nominal Ti valency different from 4+ and based upon this the possible exchange interactions which can cause ferromagnetic ordering. Therefore, a short review of the recent literature concerning ferromagnetism of Ti cations in $SrTiO_3$ shall be given subsequently.

### 6.6.2. Review of literature

In epitaxial heterostructures between **$LaMnO_3$ and $SrTiO_3$** a ferromagnetic polarization of the Ti cations at the interface has been observed via XMCD spectra [122] at low

temperatures. At the same time, shifts of the Ti $L$ edge absorption lines in the XAS spectra revealed that the Ti cations at the interface are reduced to a trivalent valency. This reduction has been attributed to a charge transfer where electrons from either Mn ions at the interface or from vacancies dope the Ti cations to a nominal valency of approximately +3.5. These extra electrons reside in the Ti $t_{2g}$ levels at the interface, and have an open spin and orbital degree of freedom. To identify the responsible mechanism for the observed ferromagnetic polarization the temperature dependence of the Ti XMCD signal was recorded and compared to the Mn XMCD signal. Hereby, the ferromagnetic-ordering of the Ti cations vanishes simultaneously with the ordering of the Mn cations when the Curie temperature $T_C$ of $LaMnO_3$ is exceeded. This suggests, that the occupied Ti $t_{2g}$ levels are coupled to the Mn cations via an Mn-O-Ti super-exchange interaction and thus adopt the ferromagnetic ordering of the ferromagnetic manganite. Analysis of the XMCD spectra revealed also the presence of an orbital angular momentum, which implies that the orbital degeneracy is not lifted by Jahn-Teller distortions, as would be expected for the $3d^1$ configuration of the $Ti^{3+}$ cations. The Jahn-Teller effect in a $3d^1$ system would prefer a deformation of the octahedral symmetry accompanied by a simultaneous lowering of the $d_{xy}$ orbital, which in turn carries no angular momentum $l_z$ (see Fig. 6.11(b)) [124, 125]. However, the Jahn-Teller effect is weak in systems where only $t_{2g}$ orbitals are occupied, since $t_{2g}$ orbitals have a smaller overlap with the neighbouring O $2p$ orbitals than $e_g$ orbitals.

Similar observation as for the $LaMnO_3/SrTiO_3$ system have been made for Ti cations at the **$BiMnO_3/SrTiO_3$** interface [126]. Hereby, an extra intensity in the valley between the two Ti $L_3$ edge peaks was accounted to the formation of $Ti^{3+}$ at the interface. From the analysis of X-ray linear dichroism spectra of the Ti $L$ edge the lowest lying $3d$ states have been identified to have an in-plane orientation, comparable to the $LaAlO_3/SrTiO_3$ interface [18]. Again, the polarization of the Ti cations could be associated to a Mn-O-Ti super-exchange interaction in an identical way like in the $LaMnO_3/SrTiO_3$ systems. In other words, the spin splitting of the Ti $3d$ at the interface is induced by a proximity effect with the adjacent ferromagnetically ordered manganites.

XMCD spectra of the Ti $L$ edge from cations at epitaxial **$LaAlO_3/SrTiO_3$** interfaces also reveal a ferromagnetic order [18]. Hereby, the XMCD spectra were compared with LFM calculations, which revealed that the dichroism is again emerging from $Ti^{3+}$ cations. To locate the $Ti^{3+}$ cations, the energy position of Ti $L$ edge transitions in XAS has been observed in dependence of the overlaying $LaAlO_3$ film thickness. Hereby, an $LaAlO_3$ wedge was deposited on $SrTiO_3$ and has been probed at different positions, which is similar to our measurements, where samples with varying $NiFe_2O_4$ overlayer thickness are used. The most interface sensitive measurements uncovered a shift of the $t_{2g}$ lines towards lower energies, which was attributed to the presence of $Ti^{3+}$ at the interface. In contrast to the $Ti^{3+}$ cations at the $LaMnO_3/SrTiO_3$ interface, the ferromagnetic order cannot be attributed to a super-exchange interaction since $LaAlO_3$ shows no magnetic behaviour at all. Instead, a distortion of the octahedral symmetry around the Ti cation at the interface has been attributed as the source of the ordering [18, 127]. Hereby, the

$TiO_6$ octahedral is compressed along the $z$-axis (perpendicular to the interface plane) which results in a lowering of the in-plane $d_{xy}$ orbitals (see Fig. 6.11(b)), which has been supported by XMCD spectra of the O $K$ edge. Thus, only the energetically favoured $d_{xy}$ orbitals are occupied by the $3d^1$ electrons resulting in an orbital ordering of the Ti $3d^1$ electrons at the interface along the $xy$ plane. However, the author neglect that this does not explain the observed ferromagnetic alignment of the spins, since in this case the ground state does not have an angular momentum ($l_z\,(d_{xy}) = 0$), and the spin-orbit interaction is thus ineffective [125]. Additionally, the superexchange interactions in a ferroorbital[3] ordered alignment would prefer an antiferromagnetic ordering of the spins, as long as the Ti-O-Ti bond angle is close to 180°.

The properties of the Ti cations at the $LaAlO_3/SrTiO_3$ interface have also been investigated by density functional studies, which also found the magnetism to be caused by Ti $3d$ electrons [128]. Though, the origin of the extra $3d$ electrons has been attributed to the presence of oxygen vacancies at the interface. While for a system without vacancies the occupation of $3d$ spin-up and down states is almost identical, an O vacancy induces an exchange splitting of the $3d$ electrons. Hereby, the excess electrons lead to a significant increase of the density of states at the Fermi edge, so that the Stoner criteria is fulfilled [128, 129]. Consistent with [18], the extra electrons predominantly occupy $d_{xy}$ orbitals. In contrast, the ferromagnetic order of these electrons is not explained by a coupling to the orbital order, but solely by the Stoner criteria.

### 6.6.3. Discussion

Based on the given review of literature the measured data presented in Fig. 6.10 will be discussed. First, we focus onto the X-ray absorption spectra of the Ti $L$ edge (Fig. 6.10(a)). A comparison of the spectra with the LFM model spectra taken from [18] reveals that the Ti cations are of predominantly $Ti^{4+}$ valency. The features in the XAS spectra can be identified with the possible $2p$ to $3d$ transition of $Ti^{4+}$ cations in an octahedral symmetry. The two peaks at 458.1 eV and 460.5 eV are forming the $L_3$ edge and are respectively related to transitions from the $2p^{3/2}$ level into $t_{2g}$ and $e_g$ bands of Ti. Likewise, the peaks at 463.5 eV and 465.9 eV can be identified with the corresponding transitions of the $L_2$ edge. The splitting of the $L_3$ edge peaks is closely related to the crystal field strength. The two small peaks at 456.6 eV and 457.2 eV are related to a transition which is forbidden in LS-coupling, but which becomes allowed because of the multipole $2p$-$3d$ interactions [131].

Upon increasing the film thickness of the overlaying $NiFe_2O_4$ film, one can clearly observe emerging shoulders in the valleys between the two $L_3$ as well as the two $L_2$ peaks, which are tagged by A and B in Fig. 6.10(a). These shoulders can be assigned to the formation of $Ti^{3+}$ cations. According to the discussion from [18], the XAS spectrum from

[3] Analogous to ferromagnetic order, ferroorbital order denotes a long range ordering of the orbital degree of freedom, whereby always the same orbital is occupied on adjacent sites (e.g. always $d_{xy}$).

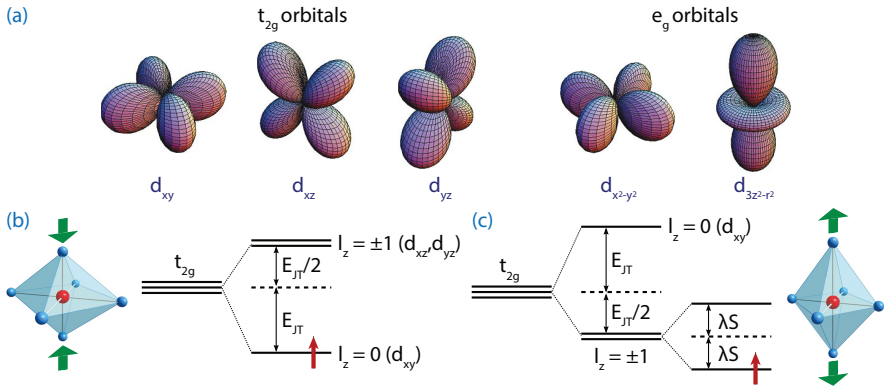


**Figure 6.11.:** Possible splittings of the $t_{2g}$ level of a cation in a distorted octahedral surrounding which is occupied with one $3d$ electron. (a) Possible $3d$ orbitals in a cubic crystal field (Image from [130]). (b) A compression of the oxygen octahedron along the $z$ axis causes a lowering of the $d_{xy}$ orbital in energy, which has no angular momentum and results in an energy gain of $E_{\mathrm{JT}}$. (c) Elongation along the $z$ axis lowers the $d_{xz}$,$d_{yz}$ doublet in energy. The spin-orbit coupling further lifts the degeneracy of the two orbitals resulting in an energy gain of $E_{\mathrm{JT}}/2 + \lambda S$. Image reproduced from [125].

a sample with a thicker overlayer becomes more sensitive to the interface region due to the limited probing depth of the TEY method. However, this argument can be doubted since an overlayer is damping all excited electrons equally and thus the relative intensity ratio of two features in a XAS spectrum should not be altered by varying the overlayer thickness, as long as the properties of the underlying $SrTiO_3$ layer are independent of the overlayer film thickness.

In contrast, if the amount of $Ti^{3+}$ cations depends on the overlayer thickness the XAS spectrum would change. For example, the shoulders clearly visible for the sample, that is covered by 4.1 nm of $NiFe_2O_4$, can be attributed to a higher concentration of $Ti^{3+}$ cations at the interface, in comparison to the 1 nm sample. The latter can be explained by oxygen diffusion from $SrTiO_3$ into $NiFe_2O_4$, whereby a thicker $NiFe_2O_4$ film can absorb a larger amount of oxygen, resulting in an increased oxygen vacancy density in $SrTiO_3$. These in turn, cause the reduction of $Ti^{4+}$ to $Ti^{3+}$ cations, in order to compensate the missing charge. Unfortunately, we cannot quantify the amount of formed $Ti^{3+}$ cations from the given data.

While the physical mechanism relevant for the formation of excess electrons at the interface cannot be unambiguously identified, it is obvious that the observed Ti dichroism and the involved spin splitting of the electronic states has to be associated with an ferromagnetic ordering of the excess electrons. If we assume the formation of $Ti^{3+}$ cations, the Ti $3d^1$ electron is occupying one of the $t_{2g}$ states and there are three possible scenarios for the ferromagnetic ordering of these electrons.

1. If the Jahn-Teller interaction is dominant, the oxygen octahedron around Ti reduces along the $z$-axis which splits the $t_{2g}$ levels into the lower lying $d_{xy}$ orbital and the higher lying $d_{xz}, d_{yz}$ doublet. Hereby, the system gains the Jahn-Teller stabilization energy $E_{\mathrm{JT}}$ per $Ti^{3+}$ cation (see Fig. 6.11(b)). This model is supported by the enlarged lattice constant of the overlaying $NiFe_2O_4$ film which induces an bi-axial tensile strain along the $xy$ plane to the $TiO_6$ octahedrons at the interface. However, similar as in the case $LaAlO_3/SrTiO_3$ in this scenario an exchange interaction which couples the spin and orbital degree of freedom of the $3d^1$ electron is lacking. Additionally, this model would lock the ferromagnetic ordering to the lattice which in turn would imply magnetocrystalline anisotropy between the $xy$-plane and the $z$ axis. While this anisotropy is clearly present at the $LaAlO_3/SrTiO_3$ interface [18], we cannot undoubtedly identify such an anisotropy in our system as visible from Fig 6.12.

2. If the spin-orbit splitting of the Ti $3d$ states is stronger than the splitting from the Jahn-Teller effect ($\lambda S + E_{\mathrm{JT}}/2 > E_{\mathrm{JT}}$) the $TiO_6$ octahedron would prefer to enlarge along the z-axis. This would lower $d_{xz}, d_{yz}$ orbitals, which are then further split by the LS-coupling resulting in an energy gain of $\lambda S + E_{\mathrm{JT}}/2$ per $Ti^{3+}$ cation (see Fig. 6.11(c)). In this scenario, the spin of the $3d^1$ electron on adjacent $Ti^{3+}$ would be coupled to the lattice via the spin-orbit interaction and thus an occurring (anti)ferroorbital ordering would be coupled to an (anti)ferromagnetic ordering of the spins. Yet, from the given arguments it is not possible to identify unambiguously the type of joint orbital and spin ordering in a $t_{2g}$ system [125]. Also, this scenario is expected to show magnetocrystalline anisotropy due to the locking of the ferromagnetic order to the lattice.

3. If both the Jahn-Teller interaction and the spin-orbit coupling are too small to lift the degeneracy of the $t_{2g}$ orbitals[4] the Ti $3d^1$ electron would be allowed to occupy all three $t_{2g}$ orbitals equally. Thus, even if the spin lattice is coupled to the orbital lattice in a certain occupation, there would be no preference of the spins to align along the $x$,$y$ or $z$-axis, since the $t_{2g}$ orbitals are symmetric. In this case two mechanisms could stabilize the ferromagnetic ordering of the electron spins. First, in an orbitally degenerate system with partially filled orbitals such an order is stabilized by the intra-atomic electron-electron interaction as described in section 2.4. Secondly, the adjacent $NiFe_2O_4$ film already holds a ferromagnetic ordering. Therefore, Fe-O-Ti, or Ni-O-Ti superexchange interactions across the $NiFe_2O_4/SrTiO_3$ interface could induce a ferromagnetic ordering of the Ti spins at the interface, similar to the case of the manganite/$SrTiO_3$ interface.

Next, we will discuss the recorded XMCD spectra from Fig. 6.10(b) in detail. For comparison, XMCD model spectra of $Ti^{3+}$ and $Ti^{4+}$ cations from LFM calculations are

[4] At $T = 0$ K a coupling, i.e. a perturbation to a degenerate system of any size would lift the degeneracy. Though, if the splitting is small enough it can be overcome by thermal fluctuation at low temperatures.

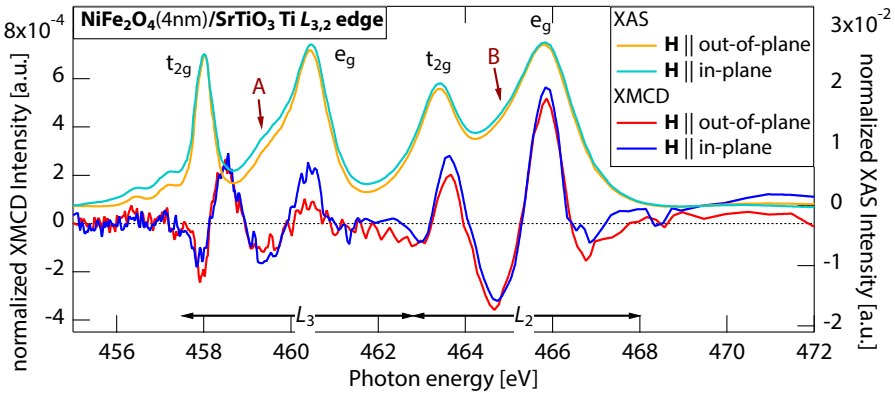


**Figure 6.12.:** XAS and XMCD spectra of the Ti $L_{3,2}$ edge of $SrTiO_3$ covered by a $d$ = 4 nm thick $NiFe_2O_4$ under recorded under in and out-of-plane geometry. The direction of the incident circular polarized beam is parallel to the applied magnetic field.

shown which have been reproduced from [18]. So far, we assumed that the spin splitting of the Ti 3$d$ states is caused by a long range ordering of the $3d^1$ states of the $Ti^{3+}$ cations only. In contrast to the observed Ti dichroism at the $LaAlO_3/SrTiO_3$ interface [18] our XMCD spectra of the Ti $L$ edge from all samples are closely matching to the model spectra for $Ti^{4+}$. Also, a fit of a superposition from the two model spectra for $Ti^{3+}$ and $Ti^{4+}$ results in a predominantly $Ti^{4+}$ nature of the recorded data. Thus, the measured XMCD spectrum cannot be caused by a magnetic ordered $3d^1$ configuration only. Likely, the observed XMCD is shaped by a similar mechanism as at the manganite/$SrTiO_3$ interface, were the reported dichroism is dominated by features that can be attributed to a $3d^0$ configuration [126]. Thereby, the result was explained by the overlap of the Ti 3$d$ orbitals with the adjacent O 2$p$ orbitals, which allow the excited Ti $2p^5 3d^1$ final state to be sensitive to the exchange field of a magnetic environment. Alternatively, one can assume a virtual hopping of the O 2$p$ electrons towards the Ti orbitals via a charge-transfer process, which results in a nominal Ti valency of less than 4. Still, the occurrence of the exchange splitting of the Ti cations at the interface was explained by a Mn-O-Ti superexchange interaction. Thus, the same argument could be transferred to the case of the $NiFe_2O_4/SrTiO_3$ interface. To verify this conclusion, the Ni, Fe and Ti $L$ edge XMCD would need to be recorded at varying temperatures. If the Ti dichroism vanishes simultaneously with the dichroism of Fe and Ni, the superexchange interaction across the interface would be confirmed.

### 6.6.4. Outlook and conclusion

Based on the results it would be interesting to investigate the orbital occupation of the Ti cations in more detail. A first hint towards an orbital order could be gained by applying

the orbital sum rule to the Ti $L$ edge XMCD. However, the recorded dichroic signal reveals significant drifts beyond the edges which renders the evaluation of the integral prone to errors. Alternatively, the XMCD of the O $K$ edge could be recorded and analysed. But since $SrTiO_3$ is already covered by the magnetic oxide $NiFe_2O_4$ one cannot easily discriminate the contributions of both materials to the O $K$ edge XMCD. Therefore, taking XMLD spectra of the Ti $L$ edge would be the method of choice.

In summary, we found a novel ferromagnetic ordering of the Ti electrons at the $NiFe_2O_4/SrTiO_3$ interface. However, the given data does not allow to quantify the contribution of the Ti ferromagnetism to the total magnetization which can be observed in SQUID experiments. Still, the extra ferromagnetic contribution of Ti could explain the observed enhanced magnetization in our samples. Especially, since for thinner films, contributions from an interfacial effect to the total signal become increasingly pronounced. From our data, we cannot unambiguously identify the origin for the ferromagnetic behaviour of Ti. However, from the discussion, we find a superexchange interaction between the cations of the ferrimagnetic $NiFe_2O_4$ film and the Ti electrons most likely.

## 6.7. Impact of non-stoichiometric film growth

In this section, the properties of a $NiFe_2O_4$ thin film that does not show bulk-like stoichiometry will be discussed. Herein, we compare the results with data from the already discussed 8.3 nm thick sample, which will be considered as a stoichiometric reference film in the following. The off-stoichiometric sample has been grown under the same conditions as the sample series discussed in chapter 5.

Fig. 6.13 depicts the SQUID hysteresis loop of the sample after substrate background subtraction. Remarkably, the film reveals a saturation magnetization $M_S$ of $2\,\mu_B$/f.u. which is considerably above the values of all films in this thickness region that have

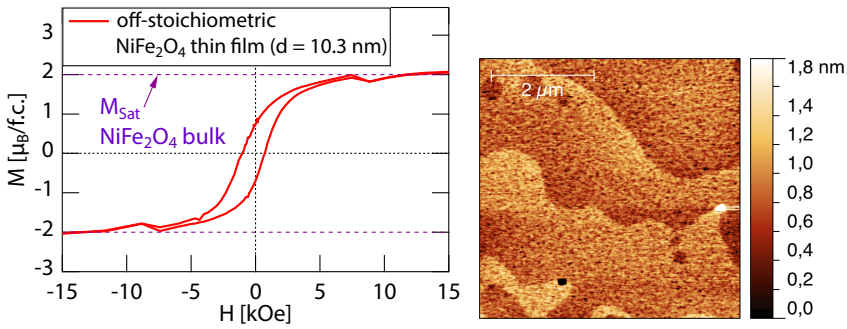


**Figure 6.13.:** Left: Detail of the SQUID hysteresis loop from a non-stoichiometric $NiFe_2O_4$ thin film. Right: AFM scan of the film surface.

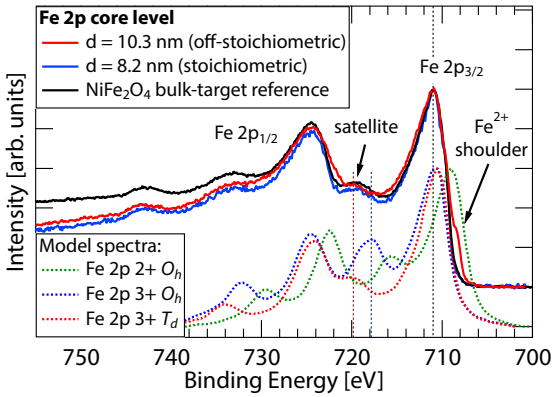


**Figure 6.14:** Fe $2p$ core level spectra of a non-stoichiometric $NiFe_2O_4$ thin film in comparison to model spectra taken from [85] and bulk spectra. Clearly identifiable is the emerging shoulder at the low binding-energy side of the Fe $2p_{3/2}$ peak, which can be attributed to the formation of $Fe^{2+}$

been investigated so far and matches the bulk value. This is surprising, since the film is still expected to form dislocations and anti-phase boundaries which would lower the saturation magnetization.

### 6.7.1. HAXPES

Thus, we investigated this sample by means of HAXPES and XMCD spectroscopy using the same experimental parameters as described in sections 5.1 and 6.1. The resulting Fe $2p$ core-level spectrum from the HAXPES experiment is shown in Fig. 6.14 in comparison to the reference spectrum from the stoichiometric film. At a first glance, the spin-split Fe $2p_{3/2}$ and $2p_{1/2}$ peaks do not shift in energy with respect to the reference, revealing that the film is still dominated by trivalent Fe cations. However, at the low binding energy sides of both peaks one can clearly identify an emerging shoulder. Its binding energy position is matching with the expected energy of $Fe^{2+}$ cations, as can be seen from the comparison with the model spectra. Thus, we attribute the occurrence of the shoulder to the formation of divalent Fe cations during growth. Unfortunately, the amount of $Fe^{2+}$ cations cannot quantified from the Fe $2p$ core level spectrum, due to the complicated multiplet structure of the peak [84]. Focussing onto the satellite peak between the two Fe $2p$ peaks, a deviation between the off-stoichiometric and the reference $NiFe_2O_4$ thin film can be clearly observed as well. The satellite is smeared out in contrast to reference spectra, supporting a presence of reduced Fe cations. However, due to its width one can not draw conclusions onto the cationic distribution.

### 6.7.2. XMCD

To get a deeper insight into the influence of the altered Fe valency onto the cationic distribution of the off-stoichiometric film, the XMCD spectrum is analysed and a ligand

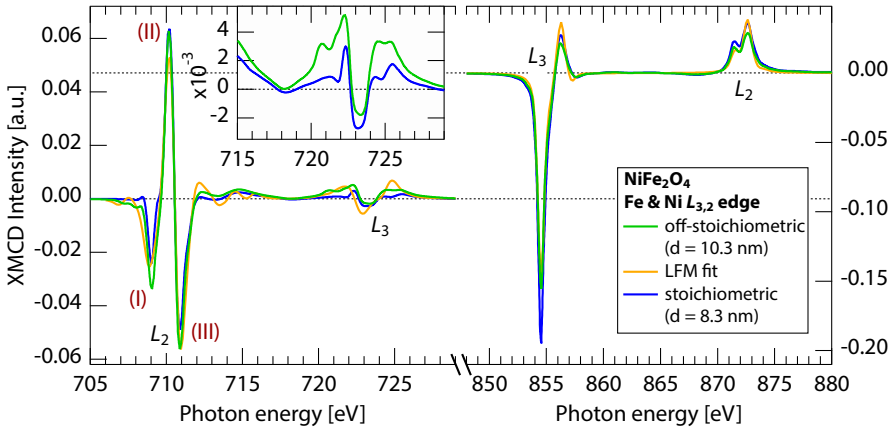


**Figure 6.15.:** XMCD spectra of the Fe and Ni $L_{2,3}$ edge from a non-stoichiometric $NiFe_2O_4$ thin film in comparison to a ligand field multiplet model and the spectra from a stoichiometric sample.

field multiplet model fit is applied to the data. The spectrum together with the fit is plotted in comparison to the MCD spectrum of the reference sample in the left side of Fig. 6.15. The modifications to the three peak structure in the $L_3$ edge immediately reveals a change. The increase of the negative peak at 710.9 eV (III) relative to the positive one at 710.2 eV (II) reflects that more trivalent Fe cations are occupying $O_h$ than $T_d$ oriented lattice sites. Also, the first negative peak at 709.0 eV (I) is enlarged with respect to the reference sample, which is consistent with the presence of a minor fraction $Fe^{2+}$ cation as observed in the HAXPES spectrum. The LFM fit yields in a Fe cation distribution of 40 % for $Fe^{3+}$ on $T_d$ sites, 43 % for $Fe^{3+}$ on $O_h$ sites, and 17 % for $Fe^{2+}$ on $O_h$ sites. The result suggests a considerably enhanced amount of Fe cations occupying octahedral lattice sites. If we would assume a bulk-like stoichiometry, this would imply an partial transition from the fully inverse ($\lambda = 1$) to the normal spinel structure with an inversion parameter of $\lambda = 0.8$. This in turn, would mean that 20 % of the Ni cations are occupying $T_d$ sites. Thus, the Ni $L_{3,2}$ edge XMCD spectrum is investigated and compared to the reference one, which both are plotted in the right side of Fig. 6.15. However, both spectra are matching almost perfectly with each other, except in amplitude, ruling out a transition of $Ni^{2+}$ cations towards tetrahedral lattice sites. The LFM model fit of the Ni $L_{3,2}$ edge also derives that the Ni cations occupy $O_h$ sites solely. Thus, the results lead to the conclusion, that the cations in the film are no more present in a bulk-like stoichiometry. Instead, an excess of Fe cations is present, which are replacing Ni cations on their octahedral lattice sites, which is supported by the decreased amplitude of the Ni MCD spectrum. Consequently, a fraction of the off-stoichiometric film is no more present as $NiFe_2O_4$ but as a $Fe_3O_4$ phase instead. This in turn, could explain the enhanced magnetization observed in the SQUID measurement, since magnetite contributes with 4 $\mu_B$/f.u. to the total magnetization as

is obvious from Fig. 6.6(c). This is supported by the results from the sum rules which yield in $m_{\mathrm{Spin}} = 0.61\,\mu_{\mathrm{B}}$/f.u. and $m_{\mathrm{Orb}} = -0.05\,\mu_{\mathrm{B}}$/f.u. for Fe and $m_{\mathrm{Spin}} = 0.64\,\mu_{\mathrm{B}}$/f.u. and $m_{\mathrm{Orb}} = 0.05\,\mu_{\mathrm{B}}$/f.u. for Ni. From the LFM model fit a stoichiometry of $Ni_{0.83}Fe_{2.17}O_4$ can be estimated. This can also be regarded to the formation of $Fe_3O_4$ clusters, which account for 17 % of the $NiFe_2O_4$ film.

### 6.7.3. Conclusion

These results are clearly different to all other investigated samples. Since the sample has been grown under identical conditions as the reference sample, one might assume the deposition process is not stable. Yet, as this sample can be clearly distinguished from the regular case and the remaining sample deliver consistent results, the PLD process still proves stability over the range of investigated samples. However, the exceptional sample underlines, that it is crucial to properly characterize every sample for its stoichiometry and cationic distribution. Hereby, the analysis of the Fe *L* edge XMCD has turned out to deliver the most sensitive results in the case of ferrites.

## 6.8. Summary from XMCD analysis

In this chapter, the local site-specific magnetic structure of the $NiFe_2O_4$ films as well as of the underlying $SrTiO_3$ substrate have been investigated in detail. The qualitative analysis of the XMCD spectra reveals an alignment of the spin structure throughout the spinel films which is comparable to the bulk. The sum rules have been applied to the Fe and Ni *L* edge, whereby we could determine the spin and orbital magnetic moments of both species in dependence of film thickness. Hereby, we found the sum of all moments to underestimate the result that has been gained from SQUID measurements. More surprisingly, the moments determined from the sum rules do not increase with decreasing film thickness as would be expected from the SQUID data. Instead, we discovered a novel ferromagnetic ordering from the electrons of the Ti cations at the $NiFe_2O_4/SrTiO_3$, which has not been observed so far. The origin of this Ti ferromagnetism has been ascribed to Fe-O-Ti or Ni-O-Ti superexchange interactions across the interface. Finally, the case of an non-stoichiometric $NiFe_2O_4$ film has been discussed. Hereby, we found that minor off-stoichiometric film compositions could significantly alter the magnetic response of the film. This emphasizes the major importance of a thorough characterization of the complex spinel structure.

# CHAPTER 7

# Conclusion

In this thesis, the magnetic oxide $NiFe_2O_4$ was evaluated as a possible candidate for a spin filter tunnel barrier. Such a barrier combines insulating and magnetic properties, which results in a highly spin-dependent tunneling probability through the barrier. For this purpose, the spinel ferrite $NiFe_2O_4$ is a auspicious material since it shows both features even at room temperature.

As a prerequisite for future integration of $NiFe_2O_4$ thin films into spin filter tunnel hybrids, the deposition process of the material on $SrTiO_3$ (001) substrates has been optimized. The main challenge was to grow thin films which reproduce the desired properties of the bulk material, i.e. insulating and ferrimagnetic behaviour. Hereby, we have employed pulsed laser deposition (PLD) as the thin film deposition technique of choice. The influence of the different PLD specific deposition parameters like laser pulse energy, background pressure and substrate temperature was studied in detail. These parameters were evaluated and optimized towards an epitaxial and single crystalline thin film growth. As additional quality parameters we minimized the mosaicity and coercive field, while simultaneously maximizing the saturation magnetization $M_S$. The inevitable formation of anti-phase boundaries, due to the half-sized lattice constant of the underlying $SrTiO_3$ substrate, hindered us in archiving an bulk-like $M_S$. However, the resulting films still reproducibly revealed ferrimagnetic behaviour. Additionally, we archieved very low surface and interface roughnesses of the $NiFe_2O_4$ films, which is beneficial for tunneling transport experiments. In summary, we have established a procedure for high quality thin film growth of $NiFe_2O_4$ on $SrTiO_3$ substrates.

On this basis, we focussed on reducing the film thickness towards the ultrathin film limit ($d$ = 1 – 4 nm), which is mandatory to obtain reasonable tunnel currents throughout the tunnel barrier in future spin filter tunnelling experiments. In this context, a question already open for an decade was addressed, i.e. the enhanced saturation magnetization

observable in ferrite ultrathin films. So far, this phenomenon has been explained by a cationic inversion of the spinel structure, e.g. an transition from the bulk-like inverse spinel structure to the normal one in ultrathin films. Still, an experimental proof for this model is lacking. Consequently, we studied the sensitive interplay between magnetic, electronic, and structural properties in thin film of the oxide $NiFe_2O_4$. Emphasis is placed on the impact of reduced dimensionality in the crossover from bulk-like to ultrathin dimensions, by growing a series of $NiFe_2O_4$ films with thicknesses between 2 – 10 nm. We observed an enhanced $M_S$ for ultrathin $NiFe_2O_4$ films, consistent with literature. The cationic distribution of all samples is investigated by a complementary bulk- and surface-sensitive analysis using HAXPES, XANES, and XMCD spectroscopy techniques, and special attention was paid to the element-specific cation valencies and coordinations. We did not find any hint for a cationic inversion to the normal spinel structure. Instead, all samples reveal a bulk-like inverse spinel structure independent of the $NiFe_2O_4$ film thickness. Thus, our studies could finally and consistently rule out a cationic inversion as the possible explanation for the observed enhanced $M_S$. More surprisingly, the $NiFe_2O_4$ films revealed an auxetic behaviour in the ultra-thin limit, i.e. the films show a reduced out-of-plane lattice constant while at the same time the in-plane constant is reduced by the biaxial compressive strain from the substrate. Based on these studies, a future step could be the integration of $NiFe_2O_4$ ultrathin films into magnetic spin filter tunnel junctions. A procedure for the fabrication of these junction is proposed in appendix C. Subsequently, these junctions can be investigated by transport experiments to finally evaluate their capabilities as a spin-filter.

With the question for the source of the enhanced magnetization in ultrathin $NiFe_2O_4$ films still open, our focus moved towards the element-specific contribution to the net magnetization in the films. Therefore, we recorded high quality XMCD spectra of the Fe and Ni $L$ edge from the thickness dependent $NiFe_2O_4$ thin film series. The data was treated using the MCD sum rules, whereby we determined the spin and orbital magnetic moments of both cation species in $NiFe_2O_4$. For the thicker films ($d > 4$ nm) the resulting moments agree with our expectations. I.e. the sum of all moments is significantly below the expected value of $2\,\mu_B$/f.u. for bulk $NiFe_2O_4$ as expected due to the distortion throughout the film by dislocations and anti-phase boundaries. Still, the moments are consistent with the magnetic structure that is expected for $NiFe_2O_4$ in the inverse spinel structure. In particular, the Fe cations contribute only a very small spin and no orbital magnetic moment, since the Fe cations are distributed equally across tetrahedral and octahedral lattice sites. These are antiferromagnetically coupled, whereby the Fe magnetic moments are cancelled out. In contrast, the Ni moments are not compensated, which is supported by the sum rule analysis. We also studied a non-stoichiometric film with excess Fe cations. Hereby, divalent Fe substitutes Ni on octahedral lattice sites. As a consequence, the sum rule analysis revealed a considerably enhanced contribution from Fe towards the net magnetization film. This result could be a possible explanation for the observed enhanced magnetization in literature, since a small off-stoichiometry is easily overlooked in ultrathin films, but significantly alters the magnetic structure of the film.

Still, this did not explain the behaviour of our ultrathin films, which do not reveal any off-stoichiometry. Therefore, we investigated the interface between the $NiFe_2O_4$ films and $SrTiO_3$ substrate in more detail. In the past few years several publications reported on emerging physical properties at atomic sharp interface between two oxides which are absent in the adjoining materials. Indeed, we found evidence of a ferromagnetic ordering of the Ti spins from the underlying substrate material. In bulk $SrTiO_3$, Ti is tetravalent and thus all orbital and spin degrees of freedom are quenched. Our spectra revealed a partial reduction of Ti into an trivalent state with a $3d^1$ electron configuration, which can be attributed to a charge transfer across the interface. We explain the ferromagnetic alignment of the Ti electron by a coupling of these $3d^1$ electrons to the ferromagnetic order of the adjacent $NiFe_2O_4$ film via a superexchange interaction across the interface. From the present data we cannot quantify the contribution of the Ti ferromagnetism to the total observed magnetization in SQUID experiments, leaving this question open for further studies. Still, the presence of this novel ferromagnetic order at the $NiFe_2O_4/SrTiO_3$ interface could explain the observed enhanced magnetization in our samples. Moreover, for the thinner films, the contributions from an interfacial effect to the total signal increases, explaining why it is only observable in the ultrathin film limit. So far, Ti ferromagnetism has only been observed at the interface between $SrTiO_3$ and manganites as well as $SrTiO_3$ and $LaAlO_3$. Thus, our measurements revealed for the first time the presence of this phenomenon at a $SrTiO_3$ to spinel interface. This opens up a new model system for studying the sensitive interplay between the lattice, spin and orbital degrees of freedom in transition metal oxides.

# APPENDIX A

## Preparation of $SrTiO_3$ (001) substrates

All $NiFe_2O_4$ thin film samples discussed in this theses have been grown on $SrTiO_3$ substrates with an (001) surface an Nb doping levels between 0 – 0.5 %. The substrates were supplied by Crystec GmbH and were delivered with a mechanically polished surface. The surface roughness can be reduced by annealing the substrates at 950 °C, which yields in a step terrace structure as shown in Fig. A.1(a). Hereby, the terraces are alternately terminated by either a SrO or a $TiO_2$ layer. To achieve a uniform $TiO_2$ termination of the substrate surface a wet etching process utilizing buffered hydrofloric acid is applied, which is removing the SrO facets [92]. For this purpose, the $SrTiO_3$ substrates are submerged in water, yielding in the formation of $Sr(OH)_2$ complexes from the SrO surface layer. Afterwards, these complexes can be removed by dissociating them with hydrofloric acid. After cleaning the substrates in acetone and isopropanol they are annealed at 950 °C in air

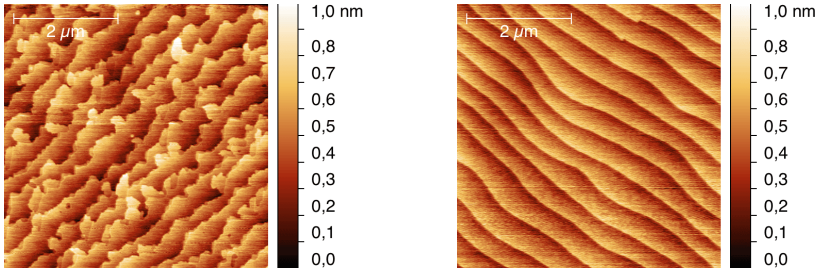


**(a)** only annealed **(b)** etched and annealed

**Figure A.1.:** AFM scans of $SrTiO_3$ (001) substrate surfaces which have been (a) only annealed at 950 °C or (b) etched and annealed using the given procedure.

and slowly cooled down subsequently. Finally, this results in a $SrTiO_3$ (001) surface which is only terminated by $TiO_2$ terraces, with a step height of exactly one unit cell (3.905 Å) as depicted in Fig. A.1(b). It is important not to anneal the as-delivered substrates prior to the etching procedure.
The following procedure has been adopted from the PGI-7 and is also described in [132]:

1. 3 min cleaning in acetone in a ultrasonic bath
2. 3 min cleaning in isopropanol in a ultrasonic bath
3. 3 min rinsing in deionized water in a ultrasonic bath
4. 30 s etching in buffered hydrofloric acid (BHF) $pH = 5.5$[1]
5. Immediate rinsing in plenty of deionized water to dilute acid residues on the substrate surface and stop the etching process
6. 3 min cleaning in acetone in a ultrasonic bath
7. 3 min cleaning in isopropanol in a ultrasonic bath
8. 120 min anealing at 950 °C in air

[1] Earlier, a no more available BHF with $pH = 6.5$ was used, whereby the etching time was 225 s.

# APPENDIX B

## Simulation of XAS and XMCD spectra

The simulation of the model XMCD spectra presented in this work has been performed using the software CTM4XAS [104]. Hereby, the possible initial and final states of an single cation are calculated in the framework of the atomic multiplet theory [133–135]. When the single electron excitation description is applied to the metal $L_{2,3}$ edges, the agreement with experimental data is poor. To consider symmetry aspects of the solid, the effect of the crystal field in a solid is included [136]. In case of oxides, the crystal field of an anion is determined in first order by the distance and the symmetry of surrounding oxygen anions. The combined treatment of atomic multiplets together with the crystal field is called ligand field multiplet (LFM) theory. The software is also capable to consider the effects of bonding, which are described by charge transfer effects between the cations and the oxygen anions [137]. A detailed description of the underlying theories can be found in [38]. On the basis of the calculated states in the cation, the possible transitions between them and their transition probabilities are computed. Finally, the determined transitions can be convoluted with a Lorentzian distribution to respect the finite core-hole lifetime and a Gaussian distribution to account for the instrumental broadening.

Fig. B.1 shows the main window of the CTM4XAS software. In the upper left part the parameters concerning the atomic multiplet are entered. One can chose the cation of interest and its valency. Below, the screening of the electron-electron interactions by the solid can be adjusted by scaling the corresponding Slater integrals, where 1.0 stands for the atomic value. Hereby, $F_{dd}$ describes coupling of the $3d$ electrons with each other. The $F_{pd}$ integral describes the dipole-dipole interaction between the created $2p$-core hole and the remaining $3d$-holes and the $G_{pd}$ integral the exchange interactions between them. Next to it, the spin-orbit coupling values of the core-hole and of the remaining holes in the excited state can be scaled.

In the lower left part, the parameters for the crystal field are entered. Most important

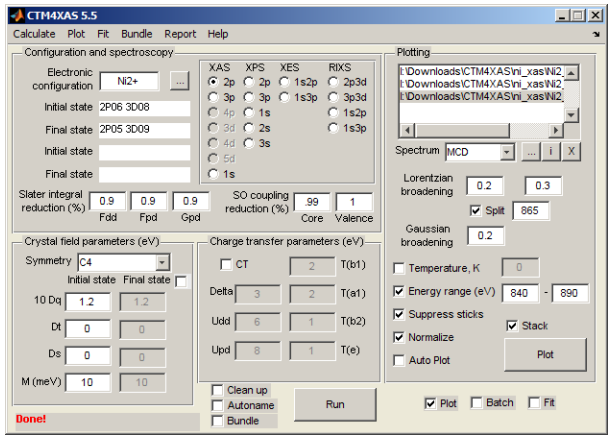


**Figure B.1:** Screenshot of the software CTM4XAS which has been used to calculated the presented model XMCD spectra in this work.

are the choice of the right symmetry group (e.g. $O_h$ for octahedral) and the crystal field splitting $10Dq$ between the $t_{2g}$ and $e_g$ levels. To include the exchange field splitting of the ground state in a ferromagnetic systems the four-fold symmetry ($C_4$) has to be chosen. One can assume that it is given by the Curie-temperature of the system [138]. Charge transfer parameters can be entered in the lower middle part, but are not used here.

On the right side one can chose the Lorentzian and Gaussian broadening of the calculated transitions. Finally, one can select the kind of plotted spectrum (e.g. XAS or MCD), whereby the displayed spectra are simultaneously written to XY-formatted files for further processing.

# APPENDIX C

## Fabrication of magnetic tunnel junctions

1. On the Nb:$SrTiO_3$ substrate an 2-5 nm thick film of $NiFe_2O_4$ is deposited, which is capped with an 25 nm thick Au capping-layer.
2. In the first step of the process the pillars of the magnetic tunnel junctions are created by means of a positive lithographic procedure containing the following steps:
   - The sample is cleaned for 3 min in acetone and then 3 min in isopropanol in an ultrasonic bath.
   - Drying for 3 min on a hot-plate set to 110 °C.
   - The resist AZ5214E is dispensed on the sample surface using a spin-coater at 4000 rpm resulting in an ≈ 1400 nm thick layer of photo-resist.
   - Hardening of the resist for 5 min on a hot-plate set to 90 °C.
   - The resist is exposed everywhere else since where the pillars should remain using a lithographic mask in a mask-aligner.
   - The resist is developed for 60-80 s, which removes all resist except on top of the pillars. (critical step)
   - The sample is etched for 4 min by reactive ion beam etching (RIBE) resulting in ≈ 50 nm high pillars (20 nm $SrTiO_3$ + 5 nm $NiFe_2O_4$ + 25 nm Au)
3. Now the whole sample is covered with 50 nm of $SiO_2$which is then completely surrounding the pillars.
4. The excessive insulator material is lifted off by solving the remaining photo-resist on top of the pillars which is done by putting the sample into dimethyl sulfoxide (DMSO) at 90 °C.

5. Now the tunnel-junctions are essentially finished but the top electrode is way to small for being electrical contacted. Therefore, a second negative lithography step is performed, to define contact pads on top of the Au electrodes .
    - The sample is cleaned for 3 min in acetone and then 3 min in isopropanol using an ultrasonic bath.
    - Drying for 3 min on a hot-plate set to 110 °C.
    - The resist AZ5214E is dispensed on the sample surface using a spin-coater at 4000 rpm.
    - Hardening of the resist for 5 min on a hot-plate set to 90 ° °C.
    - The resist is exposed for 18 s everywhere where the contact pads should form.
    - The image reversal of the resist is started by baking the sample on a hot-plate at 120 °C for exact 1 min. (critical step)
    - The sample should stay at air for at least 1 min.
    - Flood exposure of the whole sample for 90 s.
    - The resist is developed for 60-80 s, which removes all resist where the contact pads should form.
6. The sample surface is now sputtered very shortly to clean the Au top surface of pillars
7. A 250-500 nm thick layer of gold is deposited on the whole sample.
8. The excess gold is lifted off by solving the remaining resist in dimethyl sulfoxide (DMSO) at 90 °C.

# List of Figures

# Bibliography


[1] L. Stobbe, N. F. Nissen, M. Proske, A. Middendorf, B. Schlomann, M. Friedewald, P. Georgieff, and T. Leimbach, *Abschätzung des Energiebedarfs der weiteren Entwicklung der Informationsgesellschaft* (Fraunhofer IZM, Berlin, 2009) (cited on page 1).

[2] P. Grünberg, R. Schreiber, Y. Pang, M. B. Brodsky, and H. Sowers, "*Layered Magnetic Structures: Evidence for Antiferromagnetic Coupling of Fe Layers across Cr Interlayers*", Physical Review Letters **57**, 2442 (1986) doi:10.1103/PhysRevLett.57.2442 (cited on page 1).

[3] G. Binasch, P. Grünberg, F. Saurenbach, and W. Zinn, "*Enhanced magnetoresistance in layered magnetic structures with antiferromagnetic interlayer exchange*", Physical Review B **39**, 4828 (1989) doi:10.1103/PhysRevB.39.4828 (cited on page 1).

[4] M. N. Baibich, J. M. Broto, A. Fert, F. N. Van Dau, F. Petroff, P. Etienne, G. Creuzet, A. Friederich, and J. Chazelas, "*Giant Magnetoresistance of (001)Fe/(001)Cr Magnetic Superlattices*", Physical Review Letters **61**, 2472 (1988) doi:10.1103/PhysRevLett.61.2472 (cited on page 1).

[5] S. Datta and B. Das, "*Electronic analog of the electro-optic modulator*", Applied Physics Letters **56**, 665, (1990) doi:10.1063/1.102730 (cited on page 1).

[6] G.-X. Miao, M. Müller, and J. S. Moodera, "*Magnetoresistance in Double Spin Filter Tunnel Junctions with Nonmagnetic Electrodes and its Unconventional Bias Dependence*", Physical Review Letters **102**, 076601 (2009) doi:10.1103/PhysRevLett.102.076601 (cited on page 2).

[7] M. Müller, M. Luysberg, and C. M. Schneider, "*Observation of spin filtering in magnetic insulator contacts to silicon*", Applied Physics Letters **98**, 142503, (2011) doi:10.1063/1.3572016 (cited on page 2).

[8] C. Caspers, M. Müller, A. X. Gray, A. M. Kaiser, A. Gloskovskii, C. S. Fadley, W. Drube, and C. M. Schneider, "*Chemical stability of the magnetic oxide EuO directly on silicon observed by hard x-ray photoemission spectroscopy*", Physical Review B **84**, 205217 (2011) doi:10.1103/PhysRevB.84.205217 (cited on page 2).

[9] C. Caspers, A. Gloskovskij, W. Drube, C. M. Schneider, and M. Müller, "*Heteroepitaxy and ferromagnetism of EuO/MgO (001): A route towards combined spin- and symmetry-filter tunneling*", Physical Review B **88**, 245302 (2013) doi: 10.1103/PhysRevB.88.245302 (cited on page 2).

[10] C. Himcinschi, I. Vrejoiu, G. Salvan, M. Fronk, A. Talkenberger, D. R. T. Zahn, D. Rafaja, and J. Kortus, "*Optical and magneto-optical study of nickel and cobalt ferrite epitaxial thin films and submicron structures*", Journal of Applied Physics **113**, 084101, (2013) doi:10.1063/1.4792749 (cited on page 2).

[11] V. A. M. Brabers, in *Handbook of Magnetic Materials*, Vol. 8, edited by K. H. J. Buschow (Elsevier, Amsterdam, 1995), pages 189–324, isbn: 978-0-444-81974-1 (cited on pages 2, 10, 41, 59).

[12] S. Venzke, R. B. van Dover, J. M. Phillips, E. M. Gyorgy, T. Siegrist, C.-H. Chen, D. Werder, R. M. Fleming, R. J. Felder, E. Coleman, and R. Opila, "*Epitaxial Growth and Magnetic Behavior of $NiFe_2O_4$ Thin Films*", Journal of Materials Research **11**, 1187 (1996) doi:10.1557/JMR.1996.0153 (cited on pages 2, 35–37, 40, 55).

[13] U. Lüders, M. Bibes, J.-F. Bobo, M. Cantoni, R. Bertacco, and J. Fontcuberta, "*Enhanced magnetic moment and conductive behavior in $NiFe_2O_4$ spinel ultrathin films*", Physical Review B **71**, 134419 (2005) doi:10.1103/PhysRevB.71.134419 (cited on pages 2, 3, 35, 37, 55, 59).

[14] F. Rigato, S. Estradé, J. Arbiol, F. Peiró, U. Lüders, X. Martí, F. Sánchez, and J. Fontcuberta, "*Strain-induced stabilization of new magnetic spinel structures in epitaxial oxide heterostructures*", Materials Science and Engineering: B **144**, 43, (2007) doi:10.1016/j.mseb.2007.07.102 (cited on pages 2, 35–37, 40).

[15] A. Ohtomo and H. Y. Hwang, "*A high-mobility electron gas at the $LaAlO_3/SrTiO_3$ heterointerface*", Nature **427**, 423, (2004) doi:10.1038/nature02308 (cited on pages 2, 82).

[16] S. Gariglio, N. Reyren, A. D. Caviglia, and J. M. Triscone, "*Superconductivity at the $LaAlO_3/SrTiO_3$ interface*", Journal of Physics: Condensed Matter **21**, 164213, (2009) doi:10.1088/0953-8984/21/16/164213 (cited on page 2).

[17] J. A. Bert, B. Kalisky, C. Bell, M. Kim, Y. Hikita, H. Y. Hwang, and K. A. Moler, "*Direct imaging of the coexistence of ferromagnetism and superconductivity at the $LaAlO_3/SrTiO_3$ interface*", Nature Physics **7**, 767, (2011) doi:10.1038/nphys2079 (cited on page 2).

[18] J.-S. Lee, Y. W. Xie, H. K. Sato, C. Bell, Y. Hikita, H. Y. Hwang, and C.-C. Kao, "*Titanium $d_{xy}$ ferromagnetism at the $LaAlO_3/SrTiO_3$ interface*", Nature Materials **12**, 703, (2013) doi:10.1038/nmat3674 (cited on pages 2, 81–84, 86, 87).

[19] J. Mannhart and D. G. Schlom, "*Oxide Interfaces - An Opportunity for Electronics*", Science **327**, 1607, (2010) doi:10.1126/science.1181862 (cited on page 2).

[20] Y. Z. Chen, N. Bovet, F. Trier, D. V. Christensen, F. M. Qu, N. H. Andersen, T. Kasama, W. Zhang, R. Giraud, J. Dufouleur, T. S. Jespersen, J. R. Sun, A. Smith, J. Nygård, L. Lu, B. Büchner, B. G. Shen, S. Linderoth, and N. Pryds, "*A high-mobility two-dimensional electron gas at the spinel/perovskite interface of $\gamma$-$Al_2O_3/SrTiO_3$*", Nature Communications **4**, 1371 (2013) doi:10.1038/ncomms2394 (cited on page 2).

[21] F. Rigato, J. Geshev, V. Skumryev, and J. Fontcuberta, "*The magnetization of epitaxial nanometric $CoFe_2O_4(001)$ layers*", Journal of Applied Physics **106**, 113924, (2009) doi:10.1063/1.3267873 (cited on pages 3, 55, 59).

[22] B. T. Thole, P. Carra, F. Sette, and G. van der Laan, "*X-ray circular dichroism as a probe of orbital magnetization*", Physical Review Letters **68**, 1943 (1992) doi:10.1103/PhysRevLett.68.1943 (cited on pages 4, 70).

[23] P. Carra, B. T. Thole, M. Altarelli, and X. Wang, "*X-ray circular dichroism and local magnetic fields*", Physical Review Letters **70**, 694 (1993) doi:10.1103/PhysRevLett.70.694 (cited on pages 4, 70).

[24] N. F. Mott, "*The Basis of the Electron Theory of Metals, with Special Reference to the Transition Metals*", Proceedings of the Physical Society. Section A **62**, 416, (1949) doi:10.1088/0370-1298/62/7/303 (cited on page 6).

[25] J. Hubbard, "*Electron Correlations in Narrow Energy Bands*", Proceedings of the Royal Society of London A: Mathematical, Physical and Engineering Sciences **276**, 238, (1963) doi:10.1098/rspa.1963.0204 (cited on page 6).

[26] D. I. Khomskii and G. A. Sawatzky, "*Interplay between spin, charge and orbital degrees of freedom in magnetic oxides*", Solid State Communications, Highlights in Condensed Matter Physics and Materials Science **102**, 87, (1997) doi:10.1016/S0038-1098(96)00717-X (cited on page 8).

[27] J. B. Goodenough, *Magnetism and the chemical bond.* (Interscience Publishers, New York, 1963) (cited on page 8).

[28] J. Kanamori, "*Superexchange interaction and symmetry properties of electron orbitals*", Journal of Physics and Chemistry of Solids **10**, 87, (1959) doi:10.1016/0022-3697(59)90061-7 (cited on page 8).

[29] P. W. Anderson, "Chapter 2 - Exchange in Insulators", in G. T. Rado and H. Suhl, *Magnetism* (Academic Press, 1963), pages 25–83, isbn: 978-0-12-575301-2 (cited on page 8).

[30] O. Madelung, U. Rössler, and M. Schulz, in *Ternary Compounds, Organic Semiconductors*, Vol. 41E, Landolt-Börnstein - Group III Condensed Matter (Springer Berlin Heidelberg, 2000), pages 1–7, isbn: 978-3-540-66781-0 (cited on page 10).

[31] S. J. Kim, W. C. Kim, and C. S. Kim, "*Mössbauer Studies of Superexchange Interactions in $NiFe_2O_4$*", Journal of the Korean Physical Society **36**, 430 (1999) doi:10.3938/jkps.36.430 (cited on page 10).

[32] Z. Szotek, W. M. Temmerman, D. Ködderitzsch, A. Svane, L. Petit, and H. Winter, "*Electronic structures of normal and inverse spinel ferrites from first principles*", Physical Review B **74**, 174431 (2006) doi:10.1103/PhysRevB.74.174431 (cited on pages 12, 66).

[33] Z. Szotek, W. M. Temmerman, A. Svane, L. Petit, P. Strange, G. M. Stocks, D. Ködderitzsch, W. Hergert, and H. Winter, "*Electronic structure of half-metallic ferromagnets and spinel ferromagnetic insulators*", Journal of Physics: Condensed Matter **16**, S5587, (2004) doi:10.1088/0953-8984/16/48/015 (cited on page 12).

[34] H. Kiessig, "*Interferenz von Röntgenstrahlen an dünnen Schichten*", Annalen der Physik **402**, 769, (1931) doi:10.1002/andp.19314020702 (cited on page 18).

[35] L. G. Parratt, "*Surface Studies of Solids by Total Reflection of X-Rays*", Physical Review **95**, 359 (1954) doi:10.1103/PhysRev.95.359 (cited on page 18).

[36] K. Gramm, L. Lundgren, and O. Beckman, "*SQUID Magnetometer for Mangetization Measurements*", Physica Scripta **13**, 93, (1976) doi:10.1088/0031-8949/13/2/004 (cited on page 19).

[37] S. Hüfner, *Photoelectron spectroscopy* (Springer, Berlin, 1995), isbn: 3-540-19108-9 (cited on pages 23, 27).

[38] F. de Groot and A. Kotani, *Core Level Spectroscopy of Solids*, Advances in Condensed Matter Science (CRC Press, Boca Raton, Florida, 2008), isbn: 978-1-4200-0842-5 (cited on pages 23, 25, 99).

[39] J. Stöhr and H. C. Siegmann, *Magnetism* (Springer-Verlag, Berlin Heidelberg, 2006), isbn: 978-3-540-30282-7 (cited on pages 24, 25).

[40] H. Hertz, "*Ueber einen Einfluss des ultravioletten Lichtes auf die electrische Entladung*", Annalen der Physik **267**, 983, (1887) doi:10.1002/andp.18872670827 (cited on page 25).

[41] A. Einstein, "*Über einen die Erzeugung und Verwandlung des Lichtes betreffenden heuristischen Gesichtspunkt*", Annalen der Physik **322**, 132, (1905) doi:10.1002/andp.19053220607 (cited on page 25).

[42] C. Berglund and W. Spicer, "*Photoemission Studies of Copper and Silver: Experiment*", Physical Review **136**, A1044 (1964) doi:10.1103/PhysRev.136.A1044 (cited on page 26).

[43] *ISO 18115, Surface Chemical Analysis – Vocabulary* (International Organization for Standardization, Geneva, 2011) (cited on pages 28–30).

[44] C. J. Powell and A. Jablonski, "*Surface sensitivity of X-ray photoelectron spectroscopy*", Nuclear Instruments and Methods in Physics Research Section A: Accelerators, Spectrometers, Detectors and Associated Equipment, Special issue in honour of Prof. Kai Siegbahn **601**, 54, (2009) doi:10.1016/j.nima.2008.12.103 (cited on pages 28, 30).

[45] A. Jablonski and C. J. Powell, "*Information depth and the mean escape depth in Auger electron spectroscopy and x-ray photoelectron spectroscopy*", Journal of Vacuum Science & Technology A **21**, 274, (2003) doi:10.1116/1.1538370 (cited on page 29).

[46] A. Jablonski, I. S. Tilinin, and C. J. Powell, "*Mean escape depth of signal photoelectrons from amorphous and polycrystalline solids*", Physical Review B **54**, 10927 (1996) doi:10.1103/PhysRevB.54.10927 (cited on page 29).

[47] A. Jablonski and C. J. Powell, "*Relationships between electron inelastic mean free paths, effective attenuation lengths, and mean escape depths*", Journal of Electron Spectroscopy and Related Phenomena **100**, 137, (1999) doi:10.1016/S0368-2048(99)00044-4 (cited on page 29).

[48] S. Tanuma, C. J. Powell, and D. R. Penn, "*Calculations of electron inelastic mean free paths. IX. Data for 41 elemental solids over the 50 eV to 30 keV range*", Surface and Interface Analysis **43**, 689, (2011) doi:10.1002/sia.3522 (cited on page 29).

[49] S. Tanuma, C. J. Powell, and D. R. Penn, "*Calculations of electron inelastic mean free paths. V. Data for 14 organic compounds over the 50–2000 eV range*", Surface and Interface Analysis **21**, 165, (1994) doi:10.1002/sia.740210302 (cited on page 30).

[50] Wolfgang S. M. Werner, Werner Smekal, and Cedric J. Powell, *NIST Database for the Simulation of Electron Spectra for Surface Analysis (SESSA)*, version 1.3, Gaithersburg, Maryland, May 2011, http://www.nist.gov/srd/nist100.cfm (cited on pages 30, 33).

[51] J. Yeh and I. Lindau, "*Atomic subshell photoionization cross sections and asymmetry parameters:* $1 \leq Z \leq 103$", Atomic Data and Nuclear Data Tables **32**, 1, (1985) doi:10.1016/0092-640X(85)90016-6 (cited on page 32).

[52] M. B. Trzhaskovskaya, V. I. Nefedov, and V. G. Yarzhemsky, "*Photoelectron angular distribution parameters for elements Z=1 to Z=54 in the photoelectron energy range 100–5000 eV*", Atomic Data and Nuclear Data Tables **77**, 97, (2001) doi:10.1006/adnd.2000.0849 (cited on pages 32, 33).

[53] J. W. Cooper, "*Photoelectron-angular-distribution parameters for rare-gas subshells*", Physical Review A **47**, 1841 (1993) doi:10.1103/PhysRevA.47.1841 (cited on page 32).

[54] J. H. Scofield, *Theoretical photoionization cross sections from 1 to 1500 keV*. (University of California, Lawrence Livermore Laboratory, Livermore, California, Jan. 12, 1973) (cited on page 33).

[55] J. J. Yeh, *Atomic Calculation of Photoionization Cross-Sections and Asymmetry Parameters* (Gordon & Breach Science Publishers, Langhorne, PA, June 1993), 250 pages, isbn: 978-2-88124-585-5 (cited on page 33).

[56] M. B. Trzhaskovskaya, V. I. Nefedov, and V. G. Yarzhemsky, "*Photoelectron angular distribution parameters for elements Z=55 to Z=100 in the photoelectron energy range 100–5000 eV*", Atomic Data and Nuclear Data Tables **82**, 257, (2002) doi:10.1006/adnd.2002.0886 (cited on page 33).

[57] J. X. Ma, D. Mazumdar, G. Kim, H. Sato, N. Z. Bao, and A. Gupta, "*A robust approach for the growth of epitaxial spinel ferrite films*", Journal of Applied Physics **108**, 063917, (2010) doi:10.1063/1.3488638 (cited on pages 35–37, 40).

[58] U. Lüders, A. Barthélémy, M. Bibes, K. Bouzehouane, S. Fusil, E. Jacquet, J. Contour, J. Bobo, J. Fontcuberta, and A. Fert, "*$NiFe_2O_4$: A Versatile Spinel Material Brings New Opportunities for Spintronics*", Advanced Materials **18**, 1733, (2006) doi:10.1002/adma.200500972 (cited on pages 35, 46).

[59] A. V. Ramos, T. S. Santos, G. X. Miao, M.-J. Guittet, J.-B. Moussy, and J. S. Moodera, "*Influence of oxidation on the spin-filtering properties of $CoFe_2O_4$ and the resultant spin polarization*", Physical Review B **78**, 180402 (2008) doi:10.1103/PhysRevB.78.180402 (cited on pages 35, 46).

[60] D. Venkateshvaran, M. Althammer, A. Nielsen, S. Geprägs, M. S. Ramachandra Rao, S. T. B. Goennenwein, M. Opel, and R. Gross, "*Epitaxial $Zn_xFe_{3-x}O_4$ thin films: A spintronic material with tunable electrical and magnetic properties*", Physical Review B **79**, 134405 (2009) doi:10.1103/PhysRevB.79.134405 (cited on pages 35, 46).

[61] U. Lüders, M. Bibes, J. Bobo, and J. Fontcuberta, "*Tuning the growth orientation of $NiFe_2O_4$ films by appropriate underlayer selection*", Applied Physics A: Materials Science & Processing **80**, 427, (2005) doi:10.1007/s00339-004-2886-5 (cited on pages 36, 40).

[62] C. Klewe, M. Meinert, A. Boehnke, K. Kuepper, E. Arenholz, A. Gupta, J.-M. Schmalhorst, T. Kuschel, and G. Reiss, "*Physical characteristics and cation distribution of $NiFe_2O_4$ thin films with high resistivity prepared by reactive co-sputtering*", Journal of Applied Physics **115**, 123903, (2014) doi:10.1063/1.4869400 (cited on page 36).

[63] R. Datta, S. Kanuri, S. V. Karthik, D. Mazumdar, J. X. Ma, and A. Gupta, "*Formation of antiphase domains in $NiFe_2O_4$ thin films deposited on different substrates*", Applied Physics Letters **97**, 071907, (2010) doi:10.1063/1.3481365 (cited on pages 36, 37).

[64] R. Datta, B. Loukya, N. Li, and A. Gupta, "*Structural features of epitaxial $NiFe_2O_4$ thin films grown on different substrates by direct liquid injection chemical vapor deposition*", Journal of Crystal Growth **345**, 44, (2012) doi:10.1016/j.jcrysgro.2012.02.007 (cited on page 36).

[65] A. V. Ramos, J.-B. Moussy, M.-J. Guittet, M. Gautier-Soyer, C. Gatel, P. Bayle-Guillemaud, B. Warot-Fonrose, and E. Snoeck, "*Influence of a metallic or oxide top layer in epitaxial magnetic bilayers containing $CoFe_2O_4$(111) tunnel barriers*", Physical Review B **75**, 224421 (2007) doi:10.1103/PhysRevB.75.224421 (cited on page 36).

[66] J. A. Moyer, C. A. F. Vaz, E. Negusse, D. A. Arena, and V. E. Henrich, "*Controlling the electronic structure of $Co_{1-x}Fe_{2+x}O_4$ thin films through iron doping*", Physical Review B **83**, 035121 (2011) doi:10.1103/PhysRevB.83.035121 (cited on page 36).

[67] S. Matzen, J.-B. Moussy, R. Mattana, K. Bouzehouane, C. Deranlot, F. Petroff, J. C. Cezar, M.-A. Arrio, P. Sainctavit, C. Gatel, B. Warot-Fonrose, and Y. Zheng, "*Epitaxial growth and ferrimagnetic behavior of $MnFe_2O_4$(111) ultrathin layers for room-temperature spin filtering*", Physical Review B **83**, 184402 (2011) doi:10.1103/PhysRevB.83.184402 (cited on page 36).

[68] M. Foerster, J. M. Rebled, S. Estradé, F. Sánchez, F. Peiró, and J. Fontcuberta, "*Distinct magnetism in ultrathin epitaxial $NiFe_2O_4$ films on $MgAl_2O_4$ and $SrTiO_3$ single crystalline substrates*", Physical Review B **84**, 144422 (2011) doi:10.1103/PhysRevB.84.144422 (cited on pages 37, 59).

[69] D. T. Margulies, F. T. Parker, M. L. Rudee, F. E. Spada, J. N. Chapman, P. R. Aitchison, and A. E. Berkowitz, "*Origin of the Anomalous Magnetic Behavior in Single Crystal $Fe_3O_4$ Films*", Physical Review Letters **79**, 5162 (1997) doi:10.1103/PhysRevLett.79.5162 (cited on pages 37, 41, 59).

[70] M. Luysberg, R. G. S. Sofin, S. K. Arora, and I. V. Shvets, "*Strain relaxation in $Fe_3O_4/MgAl_2O_4$ heterostructures: Mechanism for formation of antiphase boundaries in an epitaxial system with identical symmetries of film and substrate*", Physical Review B **80**, 024111 (2009) doi:10.1103/PhysRevB.80.024111 (cited on page 37).

[71] W. Han, X. Jiang, A. Kajdos, S.-H. Yang, S. Stemmer, and S. S. P. Parkin, "*Spin injection and detection in lanthanum- and niobium-doped $SrTiO_3$ using the Hanle technique*", Nature Communications **4** (2013) doi:10.1038/ncomms3134 (cited on page 37).

[72] S. Kramer-Sinzinger, "Strukturelle, magnetische und elektronische Eigenschaften ultradünner $NiFe_2O_4$ Filme", Diplomarbeit (Universität zu Köln, Mar. 8, 2012) (cited on page 38).

[73] H. S. Kim and H. S. Kwok, "*Correlation between target-substrate distance and oxygen pressure in pulsed laser deposition of $YBa_2Cu_3O_7$*", Applied Physics Letters **61**, 2234, (1992) doi:10.1063/1.108278 (cited on page 38).

[74] R. Castro-Rodríguez, D. Reyes Coronado, A. Iribarren, B. Watts, F. Leccabue, and J. Peña, "*Correlation between target–substrate distance and oxygen pressure in pulsed laser deposition of complex oxide thin films*", Applied Physics A: Materials Science & Processing **81**, 1503, (2005) doi:10.1007/s00339-005-3302-5 (cited on page 38).

[75] J. L. Dormann, D. Fiorani, and E. Tronc, in *Advances in Chemical Physics*, edited by I. Prigogine and S. A. Rice (John Wiley & Sons, Inc., 1997), pages 283–494, isbn: 978-0-470-14157-1 (cited on page 42).

[76] C. a. F. Vaz, J. a. C. Bland, and G. Lauhoff, "*Magnetism in ultrathin film structures*", Reports on Progress in Physics **71**, 056501, (2008) doi:10.1088/0034-4885/71/5/056501 (cited on page 42).

[77] J. A. Moyer, C. A. F. Vaz, D. P. Kumah, D. A. Arena, and V. E. Henrich, "*Enhanced magnetic moment in ultrathin Fe-doped $CoFe_2O_4$ films*", Physical Review B **86**, 174404 (2012) doi:10.1103/PhysRevB.86.174404 (cited on pages 42, 59).

[78] F. C. Voogt, T. T. M. Palstra, L. Niesen, O. C. Rogojanu, M. A. James, and T. Hibma, "*Superparamagnetic behavior of structural domains in epitaxial ultrathin magnetite films*", Physical Review B **57**, R8107 (1998) doi:10.1103/PhysRevB.57.R8107 (cited on page 42).

[79] S. Wicklein, A. Sambri, S. Amoruso, X. Wang, R. Bruzzese, A. Koehl, and R. Dittmann, "*Pulsed laser ablation of complex oxides: The role of congruent ablation and preferential scattering for the film stoichiometry*", Applied Physics Letters **101**, 131601, (2012) doi:10.1063/1.4754112 (cited on page 43).

[80] D. J. Keeble, S. Wicklein, R. Dittmann, L. Ravelli, R. A. Mackie, and W. Egger, "*Identification of A- and B-Site Cation Vacancy Defects in Perovskite Oxide Thin Films*", Physical Review Letters **105**, 226102 (2010) doi:10.1103/PhysRevLett.105.226102 (cited on page 43).

[81] M. Hoppe, M. Gorgoi, C. M. Schneider, and M. Müller, "*Wide-Range Structural and Chemical Stability of the Magnetic Oxide $NiFe_2O_4$ Grown by $O_2$-Assisted Pulsed Laser Deposition*", IEEE Transactions on Magnetics **50**, 2506204, (2014) doi:10.1109/TMAG.2014.2322378 (cited on page 46).

[82] M. Gorgoi, S. Svensson, F. Schäfers, G. Öhrwall, M. Mertin, P. Bressler, O. Karis, H. Siegbahn, A. Sandell, H. Rensmo, W. Doherty, C. Jung, W. Braun, and W. Eberhardt, "*The high kinetic energy photoelectron spectroscopy facility at BESSY progress and first results*", Nuclear Instruments and Methods in Physics Research Section A: Accelerators, Spectrometers, Detectors and Associated

Equipment, Special issue in honour of Prof. Kai Siegbahn **601**, 48, (2009) doi: 10.1016/j.nima.2008.12.244 (cited on pages 47, 56).

[83] W. Drube, "*Photoelectron spectroscopy with hard X-rays*", Nuclear Instruments and Methods in Physics Research Section A: Accelerators, Spectrometers, Detectors and Associated Equipment **547**, 87, (2005) doi:10.1016/j.nima.2005.05.015 (cited on pages 49, 56).

[84] M. C. Biesinger, B. P. Payne, A. P. Grosvenor, L. W. M. Lau, A. R. Gerson, and R. S. C. Smart, "*Resolving surface chemical states in XPS analysis of first row transition metals, oxides and hydroxides: Cr, Mn, Fe, Co and Ni*", Applied Surface Science **257**, 2717, (2011) doi:10.1016/j.apsusc.2010.10.051 (cited on pages 49, 60, 89).

[85] T. Fujii, F. M. F. de Groot, G. A. Sawatzky, F. C. Voogt, T. Hibma, and K. Okada, "*In situ XPS analysis of various iron oxide films grown by $NO_2$-assisted molecular-beam epitaxy*", Physical Review B **59**, 3195 (1999) doi:10.1103/PhysRevB.59.3195 (cited on pages 49, 60–62, 89).

[86] A. P. Grosvenor, B. A. Kobe, M. C. Biesinger, and N. S. McIntyre, "*Investigation of multiplet splitting of Fe 2p XPS spectra and bonding in iron compounds*", Surface and Interface Analysis **36**, 1564, (2004) doi:10.1002/sia.1984 (cited on page 49).

[87] R. Claessen, M. Sing, M. Paul, G. Berner, A. Wetscherek, A. Müller, and W. Drube, "*Hard x-ray photoelectron spectroscopy of oxide hybrid and heterostructures: a new method for the study of buried interfaces*", New Journal of Physics **11**, 125007, (2009) doi:10.1088/1367-2630/11/12/125007 (cited on page 49).

[88] A. N. Mansour, "*Nickel Monochromated Al Kα XPS Spectra from the Physical Electronics Model 5400 Spectrometer*", Surface Science Spectra **3**, 221, (1994) doi: 10.1116/1.1247750 (cited on page 51).

[89] A. P. Grosvenor, M. C. Biesinger, R. S. Smart, and N. S. McIntyre, "*New interpretations of XPS spectra of nickel metal and oxides*", Surface Science **600**, 1771, (2006) doi:10.1016/j.susc.2006.01.041 (cited on page 51).

[90] M. Hoppe, S. Döring, M. Gorgoi, S. Cramm, and M. Müller, "*Enhanced ferrimagnetism in auxetic $NiFe_2O_4$ in the crossover to the ultrathin-film limit*", Physical Review B **91**, 054418 (2015) doi:10.1103/PhysRevB.91.054418 (cited on page 55).

[91] D. Fritsch and C. Ederer, "*Effect of epitaxial strain on the cation distribution in spinel ferrites $CoFe_2O_4$ and $NiFe_2O_4$: A density functional theory study*", Applied Physics Letters **99**, 081916, (2011) doi:10.1063/1.3631676 (cited on page 56).

[92] G. Koster, B. L. Kropman, G. J. H. M. Rijnders, D. H. A. Blank, and H. Rogalla, "*Quasi-ideal strontium titanate crystal surfaces through formation of strontium hydroxide*", Applied Physics Letters **73**, 2920, (1998) doi:10.1063/1.122630 (cited on pages 56, 97).

[93] R. A. D. Pattrick, G. van der Laan, C. M. B. Henderson, P. Kuiper, E. Dudzik, and D. J. Vaughan, "*Cation site occupancy in spinel ferrites studied by X-ray magnetic circular dichroism developing a method for mineralogists*", European Journal of Mineralogy **14**, 1095, (2002) doi:10.1127/0935-1221/2002/0014-1095 (cited on pages 57, 64).

[94] M. Foerster, M. Iliev, N. Dix, X. Martí, M. Barchuk, F. Sánchez, and J. Fontcuberta, "*The Poisson Ratio in $CoFe_2O_4$ Spinel Thin Films*", Advanced Functional Materials **22**, 4344, (2012) doi:10.1002/adfm.201200257 (cited on page 58).

[95] S. K. Arora, H.-C. Wu, R. J. Choudhary, I. V. Shvets, O. N. Mryasov, H. Yao, and W. Y. Ching, "*Giant magnetic moment in epitaxial $Fe_3O_4$ thin films on MgO(100)*", Physical Review B **77**, 134443 (2008) doi:10.1103/PhysRevB.77.134443 (cited on page 60).

[96] J. Orna, P. A. Algarabel, L. Morellón, J. A. Pardo, J. M. de Teresa, R. López Antón, F. Bartolomé, L. M. García, J. Bartolomé, J. C. Cezar, and A. Wildes, "*Origin of the giant magnetic moment in epitaxial $Fe_3O_4$ thin films*", Physical Review B **81**, 144420 (2010) doi:10.1103/PhysRevB.81.144420 (cited on page 60).

[97] D. Alders, F. C. Voogt, T. Hibma, and G. A. Sawatzky, "*Nonlocal screening effects in 2p x-ray photoemission spectroscopy of NiO (100)*", Physical Review B **54**, 7716 (1996) doi:10.1103/PhysRevB.54.7716 (cited on pages 60, 61).

[98] M. A. van Veenendaal and G. A. Sawatzky, "*Nonlocal screening effects in 2p x-ray photoemission spectroscopy core-level line shapes of transition metal compounds*", Physical Review Letters **70**, 2459 (1993) doi:10.1103/PhysRevLett.70.2459 (cited on page 60).

[99] K. Matsumoto, F. Saito, T. Toyoda, K. Ohkubo, K. Yamawaki, T. Mori, K. Hirano, M. Tanaka, and S. Sasaki, "*Site-Specific Studies on X-Ray Magnetic Circular Dichroism at Fe K Edge for Transition-Metal Ferrites*", Japanese Journal of Applied Physics **39**, 6089 (2000) doi:10.1143/JJAP.39.6089 (cited on pages 63, 64).

[100] F. d. Groot, G. Vankó, and P. Glatzel, "*The 1s x-ray absorption pre-edge structures in transition metal oxides*", Journal of Physics: Condensed Matter **21**, 104207, (2009) doi:10.1088/0953-8984/21/10/104207 (cited on page 62).

[101] M. Wilke, F. Farges, P.-E. Petit, G. E. Brown, and F. Martin, "*Oxidation state and coordination of Fe in minerals: An Fe K-XANES spectroscopic study*", American Mineralogist **86**, 714, (2001) (cited on page 63).

[102] S. Sasaki, "*$Fe^{2+}$ and $Fe^{3+}$ ions distinguishable by x-ray anomalous scattering: Method and its application to magnetite*", Review of Scientific Instruments **66**, 1573, (1995) doi:10.1063/1.1145911 (cited on page 64).

[103] F. Saito, T. Toyoda, T. Mori, M. Tanaka, K. Hirano, and S. Sasaki, "*Site- and valence-selective study on the origin of Fe peaks in X-ray magnetic circular dichroism of Ni ferrites, $Fe[Ni_xFe_{2-x}]O_4$*", Physica B: Condensed Matter **270**, 35, (1999) doi:10.1016/S0921-4526(99)00163-5 (cited on page 64).

[104] E. Stavitski and F. M. de Groot, "*The CTM4XAS program for EELS and XAS spectral shape analysis of transition metal L edges*", Micron **41**, 687, (2010) doi: 10.1016/j.micron.2010.06.005 (cited on pages 64, 99).

[105] S. Gold, "Winkel- und Temperaturabhängigkeit der magnetokristallinen Anisotropieenergie und der mikroskopischen magnetischen Momente des ferromagnetischen Halbmetalls $CrO_2$", PhD thesis (Universität Würzburg, Würzburg, Oct. 25, 2005), 110 pages (cited on page 67).

[106] W. Braun, H. Petersen, J. Feldhaus, A. M. Bradshaw, E. Dietz, J. Haase, I. T. McGovern, A. Puschmann, A. Reimer, H. H. Rotermund, and R. Unwin, "*Soft X-Ray Monochromators At Bessy*", Proc. SPIE **0447**, 117 (1984) (cited on page 68).

[107] E. Goering, S. Gold, A. Bayer, and G. Schuetz, "*Non-symmetric influences in the total electron yield X-ray magnetic circular dichroism signal in applied magnetic fields*", Journal of Synchrotron Radiation **8**, 434 (2001) doi:10.1107/S0909049500018343 (cited on page 70).

[108] E. Goering, A. Fuss, W. Weber, J. Will, and G. Schütz, "*Element specific x-ray magnetic circular dichroism magnetization curves using total electron yield*", Journal of Applied Physics **88**, 5920, (2000) doi:10.1063/1.1308095 (cited on page 70).

[109] C. T. Chen, Y. U. Idzerda, H.-J. Lin, N. V. Smith, G. Meigs, E. Chaban, G. H. Ho, E. Pellegrin, and F. Sette, "*Experimental Confirmation of the X-Ray Magnetic Circular Dichroism Sum Rules for Iron and Cobalt*", Physical Review Letters **75**, 152 (1995) doi:10.1103/PhysRevLett.75.152 (cited on page 71).

[110] J. Stöhr and H. König, "*Determination of Spin- and Orbital-Moment Anisotropies in Transition Metals by Angle-Dependent X-Ray Magnetic Circular Dichroism*", Physical Review Letters **75**, 3748 (1995) doi:10.1103/PhysRevLett.75.3748 (cited on page 71).

[111] E. Goering, S. Gold, M. Lafkioti, and G. Schütz, "*Vanishing Fe 3d orbital moments in single-crystalline magnetite*", EPL (Europhysics Letters) **73**, 97, (2006) doi:10.1209/epl/i2005-10359-8 (cited on pages 71, 75).

[112] R. Hesse, *Unifit*, version 2013, Leipzig, 2012, http://www.uni-leipzig.de/~unifit/ (cited on page 71).

[113] G. van der Laan, C. M. B. Henderson, R. A. D. Pattrick, S. S. Dhesi, P. F. Schofield, E. Dudzik, and D. J. Vaughan, "*Orbital polarization in $NiFe_2O_4$ measured by Ni-2p x-ray magnetic circular dichroism*", Physical Review B **59**, 4314 (1999) doi:10.1103/PhysRevB.59.4314 (cited on pages 73, 78–80).

[114] G. v. d. Laan, C. S. Mythen, and H. A. Padmore, "*Electronic Polaron Excitations in the X-Ray Absorption Spectrum of $TiO_2$*", EPL (Europhysics Letters) **11**, 67, (1990) doi:10.1209/0295-5075/11/1/012 (cited on page 73).

[115] A. Müller, A. Ruff, M. Paul, A. Wetscherek, G. Berner, U. Bauer, C. Praetorius, K. Fauth, M. Przybylski, M. Gorgoi, M. Sing, and R. Claessen, "*$Fe_3O_4$ on ZnO: A spectroscopic study of film and interface properties*", Thin Solid Films **520**, 368, (2011) doi:10.1016/j.tsf.2011.07.023 (cited on page 73).

[116] E. Goering, "*X-ray magnetic circular dichroism sum rule correction for the light transition metals*", Philosophical Magazine **85**, 2895, (2005) doi:10.1080/14786430500155221 (cited on page 75).

[117] E. Goering, S. Gold, and A. Bayer, "*Ground-State-Moment-Analysis: A quantitative tool for X-ray magnetic circular dichroism analysis for 3d transition metals*", Applied Physics A **78**, 855, (2004) doi:10.1007/s00339-003-2442-8 (cited on page 75).

[118] D. J. Huang, C. F. Chang, H.-T. Jeng, G. Y. Guo, H.-J. Lin, W. B. Wu, H. C. Ku, A. Fujimori, Y. Takahashi, and C. T. Chen, "*Spin and Orbital Magnetic Moments of $Fe_3O_4$*", Physical Review Letters **93**, 077204 (2004) doi:10.1103/PhysRevLett.93.077204 (cited on page 75).

[119] D. Ahlers, K. Attenkofer, and G. Schütz, "*Spin-dependent extended x-ray absorption fine structure in magnetic oxides*", Journal of Applied Physics **83**, 7085, (1998) doi:10.1063/1.367854 (cited on page 75).

[120] T. Saitoh, A. E. Bocquet, T. Mizokawa, and A. Fujimori, "*Systematic variation of the electronic structure of 3d transition-metal compounds*", Physical Review B **52**, 7934 (1995) doi:10.1103/PhysRevB.52.7934 (cited on page 75).

[121] M. Meinert and G. Reiss, "*Electronic structure and optical band gap determination of $NiFe_2O_4$*", Journal of Physics: Condensed Matter **26**, 115503, (2014) doi:10.1088/0953-8984/26/11/115503 (cited on pages 76, 79).

[122] J. Garcia-Barriocanal, J. C. Cezar, F. Y. Bruno, P. Thakur, N. B. Brookes, C. Utfeld, A. Rivera-Calzada, S. R. Giblin, J. W. Taylor, J. A. Duffy, S. B. Dugdale, T. Nakamura, K. Kodama, C. Leon, S. Okamoto, and J. Santamaria, "*Spin and orbital Ti magnetism at $LaMnO_3/SrTiO_3$ interfaces*", Nature Communications **1**, 82 (2010) doi:10.1038/ncomms1080 (cited on page 82).

[123] K. v. Benthem, C. Elsässer, and R. H. French, "*Bulk electronic structure of SrTiO3: Experiment and theory*", Journal of Applied Physics **90**, 6156, (2001) doi:10.1063/1.1415766 (cited on page 82).

[124] H. A. Jahn and E. Teller, "*Stability of Polyatomic Molecules in Degenerate Electronic States. I. Orbital Degeneracy*", Proceedings of the Royal Society of London. Series A, Mathematical and Physical Sciences **161**, 220, (1937) doi:10.1098/rspa.1937.0142 (cited on page 83).

[125] K. I. Kugel and D. I. Khomskii, "*The Jahn-Teller effect and magnetism: transition metal compounds*", Soviet Physics Uspekhi **25**, 231, (1982) doi:10.1070/PU1982v025n04ABEH004537 (cited on pages 83–86).

[126] M. Salluzzo, S. Gariglio, D. Stornaiuolo, V. Sessi, S. Rusponi, C. Piamonteze, G. M. De Luca, M. Minola, D. Marré, A. Gadaleta, H. Brune, F. Nolting, N. B. Brookes, and G. Ghiringhelli, "*Origin of Interface Magnetism in $BiMnO_3/SrTiO_3$ and $LaAlO_3/SrTiO_3$ Heterostructures*", Physical Review Letters **111**, 087204 (2013) doi:10.1103/PhysRevLett.111.087204 (cited on pages 83, 87).

[127] M. Salluzzo, J. C. Cezar, N. B. Brookes, V. Bisogni, G. M. De Luca, C. Richter, S. Thiel, J. Mannhart, M. Huijben, A. Brinkman, G. Rijnders, and G. Ghiringhelli, "*Orbital Reconstruction and the Two-Dimensional Electron Gas at the $LaAlO_3/SrTiO_3$ Interface*", Physical Review Letters **102**, 166804 (2009) doi:10.1103/PhysRevLett.102.166804 (cited on page 83).

[128] N. Pavlenko, T. Kopp, E. Y. Tsymbal, G. A. Sawatzky, and J. Mannhart, "*Magnetic and superconducting phases at the $LaAlO_3/SrTiO_3$ interface: The role of interfacial Ti 3d electrons*", Physical Review B **85**, 020407 (2012) doi:10.1103/PhysRevB.85.020407 (cited on page 84).

[129] A. P. Petrović, A. Paré, T. R. Paudel, K. Lee, S. Holmes, C. H. W. Barnes, A. David, T. Wu, E. Y. Tsymbal, and C. Panagopoulos, "*Emergent vortices at a ferromagnetic superconducting oxide interface*", New Journal of Physics **16**, 103012, (2014) doi:10.1088/1367-2630/16/10/103012 (cited on page 84).

[130] Y. Tokura and N. Nagaosa, "*Orbital Physics in Transition-Metal Oxides*", Science **288**, 462, (2000) doi:10.1126/science.288.5465.462 (cited on page 85).

[131] F. M. F. de Groot, M. O. Figueiredo, M. J. Basto, M. Abbate, H. Petersen, and J. C. Fuggle, "*2p X-ray Absorption of Titanium in Minerals*", Physics and Chemistry of Minerals **19**, 140 (1992) doi:10.1007/BF00202101 (cited on page 84).

[132] F. Gunkel, "The Influence of Defects on the Conductivity of the LAO/STO-Interface", Diplomarbeit (RWTH Aachen, Aug. 2009) (cited on page 98).

[133] R. P. Gupta and S. K. Sen, "*Calculation of multiplet structure of core p-vacancy levels*", Physical Review B **10**, 71 (1974) doi:10.1103/PhysRevB.10.71 (cited on page 99).

[134] R. P. Gupta and S. K. Sen, "*Calculation of multiplet structure of core p-vacancy levels. II*", Physical Review B **12**, 15 (1975) doi:10.1103/PhysRevB.12.15 (cited on page 99).

[135] S. Suga, S. Shin, M. Taniguchi, K. Inoue, M. Seki, I. Nakada, S. Shibuya, and T. Yamaguchi, "*Reflectance spectra of $ZnCr_2Se_4$ spinel from 4 to 100 eV measured with synchrotron radiation: Band structure, covalency, and final-state interactions*", Physical Review B **25**, 5486 (1982) doi:10.1103/PhysRevB.25.5486 (cited on page 99).

[136] B. Thole, G. van der Laan, and P. Butler, "*Spin-mixed ground state of Fe phthalocyanine and the temperature-dependent branching ratio in X-ray absorption spectroscopy*", Chemical Physics Letters **149**, 295, (1988) doi:10.1016/0009-2614(88)85029-2 (cited on page 99).

[137] H. Ogasawara, A. Kotani, K. Okada, and B. T. Thole, "*Theory of x-ray-absorption spectra in $PrO_2$ and some other rare-earth compounds*", Physical Review B **43**, 854 (1991) doi:10.1103/PhysRevB.43.854 (cited on page 99).

[138] C. Piamonteze, P. Miedema, and F. M. F. de Groot, "*Accuracy of the spin sum rule in XMCD for the transition-metal L edges from manganese to copper*", Physical Review B **80**, 184410 (2009) doi:10.1103/PhysRevB.80.184410 (cited on page 100).

# Own Publications


[1] M. Hoppe, S. Döring, M. Gorgoi, S. Cramm, and M. Müller, "*Enhanced ferrimagnetism in auxetic $NiFe_2O_4$ in the crossover to the ultrathin-film limit*", Physical Review B **91**, 054418 (2015) doi:10.1103/PhysRevB.91.054418.

[2] M. Hoppe, M. Gorgoi, C. M. Schneider, and M. Müller, "*Wide-Range Structural and Chemical Stability of the Magnetic Oxide $NiFe_2O_4$ Grown by $O_2$-Assisted Pulsed Laser Deposition*", IEEE Transactions on Magnetics **50**, 2506204, (2014) doi:10.1109/TMAG.2014.2322378.

[3] D. M. Gottlob, T. Jansen, M. Hoppe, D. E. Bürgler, and C. M. Schneider, "*Epitaxial Cu(001) films grown on a Cr/Ag/Fe/GaAs(001) buffer system*", Thin Solid Films **562**, 250, (2014) doi:10.1016/j.tsf.2014.04.078.

# Conference Contributions

[1] M. Voigt, C. Caspers, B. Zijlstra, S. Flade, S. Döring, M. Gorgoi, C. M. Schneider, and M. Müller, "*Electronic, structural and magnetic properties of $NiFe_2O_4$ ultra thin films*", Poster, DPG-Frühjahrstagung, Regensburg, Mar. 12–15, 2013.

[2] M. Hoppe, S. Döring, M. Gorgoi, C. M. Schneider, and M. Müller, "*$NiFe_2O_4$: a candidate for efficient spin filtering at room temperature?*", Poster, Fifth Joint BER II and BESSY II User Meeting, Berlin, Dec. 4–6, 2013.

[3] M. Hoppe, S. Döring, S. Cramm, M. Gorgoi, C. M. Schneider, and M. Müller, "*$NiFe_2O_4$: a candidate for efficient spin filtering at room temperature?*", Poster, 550th Wilhelm and Else Heraeus seminar, Bad Honnef, Jan. 8–10, 2014.

[4] M. Hoppe, S. Döring, M. Gorgoi, F. Gunkel, C. M. Schneider, and M. Müller, "*$NiFe_2O_4$: a candidate for efficient spin filtering at room temperature?*", Talk, DPG-Frühjahrstagung, Dresden, Mar. 30–Apr. 4, 2014.

[5] M. Hoppe, S. Döring, S. Cramm, M. Gorgoi, C. M. Schneider, and M. Müller, "*$NiFe_2O_4$: a candidate for efficient spin filtering at room temperature?*", Poster, INTERMAG Europe, Dresden, May 4–8, 2014.

[6] M. Hoppe, S. Döring, M. Gorgoi, C. M. Schneider, and M. Müller, "*Chemical and magnetic properties of $NiFe_2O_4$ ultrathin films: A combined study via HAXPES, XANES and XMCD*", Poster, SNI2014, Bonn, Sept. 21–23, 2014.

[7] M. Hoppe, S. Döring, M. Gorgoi, S. Cramm, and M. Müller, "*Enhanced ferrimagnetism in auxetic $NiFe_2O_4$ in the crossover to the ultrathin film limit*", Poster, 580th Wilhelm und Else Heraeus Seminar, Bad Honnef, Jan. 7–9, 2015.

[8] M. Hoppe, S. Döring, M. Gorgoi, S. Cramm, and M. Müller, "*Enhanced ferrimagnetism in auxetic $NiFe_2O_4$ in the crossover to the ultrathin film limit*", Poster, JARA Nanoelectronic Days 2015, Jülich, Apr. 27–30, 2015.

# Acknowledgements

At the end, I would like to thank all the people who have supported me during my work and contributed to the successful completion of this thesis.

First of all, I would like to thank my advisor Martina Müller for the chance to work in her research group and for her guidance and support over the years. I also appreciate your commitment that gave me the chance to meet many scientists from the magnetism community and to perform lots of measurements at synchrotron facilities.

I want to give special thanks to Kai Fauth, who has undertaken major efforts to make our XMCD beamtime possible in the first place and to become successful and also for agreeing to act as second reviewer for my thesis.

Sincere thanks goes to my colleagues from the Oxide Spintronics Lab: Timm Gerber, Patrick Lömker, Christian Caspers, Bernardus Zijlstra and Katrin Neureiter. Thank you for the outstanding team work.

Thanks to Sven Döring, Mihaela Gorgoi, Stefan Cramm, Martin Zinner and Andrei Gloskovskij for enduring and fruitful support during several beamtimes.

I would like to thank Thomas Jansen, Heinz Pfeifer, Norbert Schnitzler, and Franz-Josef Köhne for their indispensable technical support.

I also want to thank all my colleagues from the PGI-6 for the workaday support and the enjoyable time I have spent at the institute. It was a pleasure to work with you.

I thank my family and my friends for their continued support during my entire studies and the PhD time.

Finally, I want to thank my wife Charlotte for everything.

Band / Volume 105
**Resonant Magnetic Scattering Studies using Synchrotron Radiation and Laser-Generated Extreme Ultraviolet Light**
C. M. Weier (2015), vii, 143 pp
ISBN: 978-3-95806-052-4

Band / Volume 106
**Neutron Scattering**
Lectures of the JCNS Laboratory Course held at Forschungszentrum Jülich and at the Heinz-Maier-Leibnitz Zentrum Garching
edited by Th. Brückel, D. Richter, G. Roth, A. Wischnewski and R. Zorn (2015), ca 300 pp
ISBN: 978-3-95806-055-5

Band / Volume 107
**Neutron Scattering**
Experimental Manuals of the JCNS Laboratory Course held at Forschungszentrum Jülich and at the Heinz-Maier-Leibnitz Zentrum Garching
edited by Th. Brückel, D. Richter, G. Roth, A. Wischnewski and R. Zorn (2015), ca 150 pp
ISBN: 978-3-95806-056-2

Band / Volume 108
**STM-based quantum transport through molecular wires**
N. Fournier (2015), ix, 295 pp
ISBN: 978-3-95806-059-3

Band / Volume 109
**Study on the electroforming and resistive switching behaviour of nickel oxide thin fims for non-volatile memory applications**
R. Weng (2015), xxi, 159 pp
ISBN: 978-3-95806-062-3

Band / Volume 110
**Microswimmers – From Single Particle Motion to Collective Behaviour**
Lecture Notes of the DFG SPP Summer School 2015
edited by G. Gompper, C. Bechinger, S. Herminghaus, R. E. Isele-Holder, U.B. Kaupp, H. Löwen, H. Stark, R. G. Winkler (2015)
ISBN: 978-3-95806-083-8

Band / Volume 111
**Long range order in 3D nanoparticle assemblies**
E. Josten (2015), 238 pp
ISBN: 978-3-95806-087-6

Band / Volume 112
**Silicon nanowire structures for neuronal cell interfacing**
S. Pud (2015), 153 pp
ISBN: 978-3-95806-089-0

Band / Volume 113
**Memristive Phenomena -**
**From Fundamental Physics to Neuromorphic Computing**
Lecture Notes of the 47th IFF Spring School 2016
22 February – 04 March 2016, Jülich, Germany
ed. by R. Waser and M. Wuttig (2016), ca 1000 pp
ISBN: 978-3-95806-091-3

Band / Volume 114
**Single-Cell Analysis of Microbial Production Strains**
**in Microfluidic Bioreactors**
A. M. Grünberger (2015), XIX, 225 pp
ISBN: 978-3-95806-092-0

Band / Volume 115
**Magnetic order and spin dynamics in the**
**extended kagome system $CaBaCo_2Fe_2O_7$**
J. Reim (2015), viii, 144 pp
ISBN: 978-3-95806-097-5

Band / Volume 116
**Structural and electronic investigations on homo- and hetero-organic**
**layers involving CuPc on silver single crystal surfaces**
K. M. Schönauer (2015), x, 148 pp
ISBN: 978-3-95806-112-5

Band / Volume 117
**First-principles investigation of inelastic magnetic excitations**
**in nanostructures deposited on surfaces**
B. J. Schweflinghaus (2016), v, 204 pp
ISBN: 978-3-95806-115-6

Band / Volume 118
**Magnetic, structural, and electronic properties of $NiFe_2O_4$ ultrathin films**
M. Hoppe (2016), vii, 118 pp
ISBN: 978-3-95806-122-4

Schlüsseltechnologien /
Key Technologies
Band / Volume 118
ISBN 978-3-95806-122-4